

Growth and Characterisation of III-V
Semiconductor Materials Grown Primarily by
AME and PA-MBE

Lucy Elizabeth Goff BSc(Hons) MSc AMInstP

Thesis submitted to the University of Nottingham for the
Degree of Doctor of Philosophy

December 2015

Abstract

This thesis describes the growth and characterisation of gallium nitride, indium nitride and indium gallium nitride semiconductors primarily carried out using a novel growth technique called Anion Modulation Epitaxy (AME) and also plasma-assisted MBE (PA-MBE). Characterisation was typically performed by x-ray diffraction, scanning electron microscopy and optical reflectance studies.

All of the work in this thesis was carried out in the hope to improve layer structure and quality which in turn would create higher efficiency solar cells.

Nanorods were grown using PA-MBE as these are known to form entirely defect-free material and this would be an attractive quality when trying to increase the efficiency. InN rods were grown at temperatures between 350°C and 450°C on SiC substrates of both Si- and C-polar faces at various indium fluxes to establish optimal growth conditions. It was found that a BEP flux of $\sim 2.0 \times 10^{-7}$ Torr and a growth temperature $\sim 400^\circ\text{C}$ provided a large array of rods. Samples produced tall, thin nanorods as well as short, fat ones. CBED analysis revealed that the tall nanorods were growing In-polar which mimics the behaviour seen for GaN. Photoluminescence (PL) data for the rods agrees with the bulk PL measurement of InN in the literature confirming that reasonable quality films have been produced. Coalescence of the rods was achieved by increasing the flux to $\sim 2.0 \times 10^{-6}$ Torr. Also, p-n junctions were

grown on both faces of SiC and preliminary tests have shown a response to light.

A new growth method was developed from conventional PA-MBE known as Anion Modulation Epitaxy (AME) and gives rise to improved growth compared with equivalent samples by PA-MBE as the growth temperature is decreased. It also allows p-doping for GaN to be carried out at lower temperatures and more consistently. Direct comparison of GaN samples grown at equivalent temperatures by PA-MBE and AME show improved structural, electrical and optical properties for the samples grown using AME. It has also proven to be a useful tool for studying temperature changes at the substrate surface when using any pulsed growth technique. Substrate temperature was shown to vary by approximately 15°C each time the flow was interrupted. Slower, long-term trends were also monitored depending on the average nitrogen to metal ratio. An increase in overall temperature is derived from increasing metal rich growth, whereas the opposite effect is true for increased nitrogen rich growth.

AME was also used for the growth of intermediate band solar cells (IBSC). The entire growth is easily monitored and altered using AME without altering the growth parameters drastically. Pulsing the nitrogen allows for variations in the metal cell fluxes to be kept under control at the surface. The discovery of 'hidden' metal in the layer would have taken a lot longer to discover, and would have ruined the sample without utilising AME.

Acknowledgements

There are a great number of people I owe thanks to that have made my PhD a possibility. Prof. Tom Foxon has always been there to answer any questions and offer support. His knowledge and help have been invaluable to me; from helping me brush up on any physics, to keeping me informed about the conferences I should be going to. I am sure he will always be there to answer any of my questions no matter where I am.

Without my supervisor Dr. Richard Campion fighting for the funding to take me on, I wouldn't be in this position now. I am so glad you managed to get the money to support me! I also need to thank you for the number of hours you spent teaching me how to use the MBE machine, as well as the conversations about my results. Dr Sergei Novikov's support in teaching me how to grow nanorods was also invaluable, along with the musings about science politics.

I would like to thank all of the technicians and workshop staff for their help when I broke the MBE machine including Bob Chettle and Mike Parker. A very special thanks goes to Steve Tabreham for both your technical help with upgrading and fixing the machine, but also your support when the going got tough. My PhD would not have been possible without you.

Chris Staddon trained me on the X-ray equipment but was also on hand to discuss the data. These conversations led to other more detailed scans

which helped to understand the samples more. Thank you for all of your help. Dr Tony Kent also allowed me to use his PL equipment for my samples. Many thanks to his postdoc Dr Paul Walker for helping me understand the equipment and being on hand to answer no end of questions.

Staff and students at the University of Bristol have provided me with detailed images and discussions about my nanorod samples and I am grateful for all of your input, especially Prof. Dave Cherns, Dr. Ian Griffiths, Richard Webster and Queenie Soundararajah.

My office mates have kept me going through the lows of equipment breakdowns. I especially need to thank Jac for teaching me to use the 'mini'-MBE even though you were deep in thesis write-up and had an impending deadline. Also, Dan and Ari for the many evenings of distractions and tutoring in fine Italian cooking, as well as Joe, Eric and Maryam for your help and support throughout.

Finally I should thank my family for their support, my brother for helping me maintain some normality during the write up, and my partner Sean. I am sorry for the number of evenings and weekends you have spent watching me write and cooking me dinner, I am eternally grateful.

Publications

L. E. Goff, S. V. Novikov, C. T. Foxon, A. J. Kent, R. Webster and D. Cherns. 'MBE growth of InN nanorods on SiC substrates' *Journal of Crystal Growth*, 386, pp135-138 (2014).

R. F. Webster, D. Cherns, L. E. Goff, S. V. Novikov, C. T. Foxon, A. M. Fischer and F. A. Ponce. 'Indium Nitride and Indium Gallium Nitride layers grown on nanorods' *Journal of Physics Conference Series*, 471(1), pp012025 (2013).

L. E. Goff, C. T. Foxon, C. R. Staddon, A. J. Kent, and R. P. Campion. 'Anion Modulation Epitaxy (AME), an alternative growth strategy for group-III nitrides' *Physica Status Solidi C* 9, No 3-4 pp530-533 (2012).

Conferences

Oral presentations:

- 9th International Conference on Nitride Semiconductors 2011, Glasgow
- UK Molecular Beam Epitaxy meeting 2010 (UKMBE), London

Poster presentations:

- International Conference on MBE 2012 (ICMBE), Nara, Japan
- UK Nitrides Consortium meeting 2011 (UKNC), London

List of Figures

1.1	Schematic of GaN/InGaN quantum well LED and TEM images of the layer.	5
1.2	Bandgap energies of the most widely used semiconductors.	6
1.3	Schematic of an MOVPE reactor.	11
2.1	Schematic of an MBE machine	16
2.2	Schematic of the holder used within the ‘mini’-system.	20
2.3	Schematic view of the RHEED geometry.	23
2.4	A 2D representation of the Ewald sphere.	24
2.5	RHEED images taken during different surface reconstructions of GaAs.	25
2.6	Schematic of how atoms at the surface can exhibit a different structure to the bulk, (a) showing a relaxed and (b) showing a reconstructed surface.	26
2.7	2D structures are described using Bravais nets.	27
2.8	2D structures are described using Bravais nets.	28
2.9	Translation between real and reciprocal space.	29
2.10	Different stages of the layer-by-layer growth mode	30
2.11	Schematic of the heater configurations in a) the gen III and b) the ‘mini’-system.	32

2.12	Schematic of the heat transfer with in the system. Arrows indicate heat flow.	33
2.13	Schematic of the kSA BandiT product setup.	36
2.14	Schematic of the various growth modes.	37
3.1	Schematic of the atomic transitions within the copper atom.	41
3.2	Schematic to show geometry of Bragg's law.	42
3.3	Schematic diagram of a high resolution double-axis X-ray diffractometer.	44
3.4	Schematic of photoluminescence.	47
3.5	Optical reflectance spectrum from a 450nm layer grown on a substrate of GaAs.	49
3.6	Schematic diagram of multiple Fabry-Pérot oscillations in a thin film of thickness d	50
4.1	Schematic of the VLS growth of Si nanocolumns using a gold catalyst.	56
4.2	Schematic of the suggested growth model for a cylindrical nanocolumn in a PA-MBE system.	58
4.3	SEM images taken at $\times 60,000$ InN.	62
4.4	Schematic drawing of the dangling bonds left when the SiC substrate is terminated on the Si- or C-face.	63
4.5	SEM and RHEED images of the InN nanorods grown on Si-face SiC.	65
4.6	SEM and RHEED images taken during the growth of InN nanorods on C-face SiC.	67
4.7	SEM image of coalesced InN layer grown on top of the InN nanorods.	68

4.8	TEM and CBED data for InN nanorods on Si-polar SiC. . . .	69
4.9	Low temperature ($\sim 4\text{K}$) PL spectrum from an InN coalesced layer on Si-face 6H-SiC.	70
4.10	RHEED images taken during the growth of InN nanorods on p-type SiC.	71
5.1	Graph illustrating the different growth regimes at different temperatures when growing gallium nitride	77
5.2	Summary of the shutter sequences used in the different types of modulated growth.	79
5.3	Shutter sequence for nitrogen flux and surface concentration of group III.	82
5.4	RHEED images taken during the AME sequence on the Gen III.	84
5.5	2theta/omega line scans for GaN at 550°C	87
5.6	Photoluminescence from the 550°C GaN sample set. LG25 is the MBE grown sample that has given out a stronger photoluminescence when compared with the AME samples. The AME samples give off less than 100 counts compared with 700 counts for the MBE sample.	87
5.7	Reciprocal space maps for samples grown at 500°C by AME and PA-MBE.	90
5.8	2theta/omega scans for the GaN sample set at 500°C	91
5.9	Photoluminescence data carried out on GaN grown at 500°C	92
5.10	X-ray data for InN with a growth temperature of 500°C	94
5.11	Growth rate data for gallium nitride at 680°C and indium nitride at 500°C	95

5.12	Images of samples resulting from different growth conditions with and without a high temperature GaN buffer.	96
5.13	Cyclic temperature changes for each sequences.	97
5.14	This graph shows how even and predictable the cyclic temperature changes become once the conditions have been optimised.	97
5.15	This graph shows the change in temperature throughout an entire growth.	98
6.1	This diagram shows electron transitions in the intermediate band.	103
6.2	This diagram shows the the different types of samples grown using AME for solar cell purposes.	105
6.3	This image shows an x-ray diffraction line scan through the GaN peak for IB91 and IB92.	106
6.4	This image shows an x-ray diffraction line scan through the GaN peak for IB96 and IB97.	108
6.5	This image shows x-ray diffraction line scans through the gallium nitride peak for IB91 and IB92.	109
6.6	This image shows the external quantum efficiency for IB102 and IB105.	111
6.7	A thermodynamic model demonstrating the miscibility gap for InGaN and a three dimensional representation of the InGaMnN phase space.	113
6.8	SEM images of InGaN 10% In, 1 % Mn at x23,000 and n-GaN on sapphire at x23,000 and x75,000 magnification.	115

List of Tables

4.1	Table of all InN growth carried out.	73
5.1	Table of XRD data for the samples grown by AME compared to control samples grown by PA-MBE at both 500°C (LG35-38) and 550°C (LG24-27). The times in brackets (t1, t2) are the times in seconds for which the nitrogen shutter was closed (t1) and open (t2). The Ga shutter is open continuously. Increasing t2, increases the time during which the growth is nitrogen rich. The MBE control sample is grown with the same Ga and N fluxes, within experimental error.	88
6.1	Table of processed samples to create solar cells all on n-GaAs substrates.	104

Contents

Abstract	i
Acknowledgements	iii
Publications	v
Conferences	vi
List of Figures	x
List of Tables	xi
Contents	xii
1 Literature Review	1
1.1 Introduction to Nitrides	1
1.1.1 Solid State Lighting	3
1.1.2 Development of LEDs	4
1.1.3 Importance of Gallium Nitride	5
1.1.4 Why does Highly defective GaN still emit light?	7
1.1.5 How to produce solid-state white light	8
1.2 How Nitrides are Grown	9
1.2.1 Metal-Organic Vapour Phase Epitaxy	9

1.2.2	Ammonia-Molecular beam Epitaxy	10
1.3	Growth of Nanocolumns	12
1.4	Conclusions	13
2	Experimental Techniques	15
2.1	Molecular Beam Epitaxy	15
2.1.1	Description of Equipment	15
2.1.2	Machine set-ups	19
2.2	RHEED	22
2.2.1	Theory of RHEED	23
2.2.2	Surface Crystallography	25
2.2.3	Growth Rate Determination	30
2.3	Temperature Monitoring during Growth	31
2.3.1	BandiT	34
2.3.2	Pyrometry	36
2.4	Growth Mechanisms	37
2.4.1	2D Growth	37
2.4.2	3D Growth	38
2.5	Conclusions	39
3	Characterisation Techniques	40
3.1	X-Ray Diffraction (XRD)	40
3.1.1	Theory	41
3.1.2	High Resolution XRD	43
3.1.3	Triple Axis Diffractometry	44
3.1.4	PANalytic X'Pert Materials Research Diffractometer	45
3.2	Scanning Electron Microscopy (SEM)	46
3.3	Photoluminescence	47

<i>CONTENTS</i>	xiv
3.4 Optical Reflectance for Thickness Measurements	48
3.5 Transmission Electron Microscopy (TEM)	49
3.5.1 Convergent Beam Electron Diffraction (CBED)	51
3.6 Seebeck effect	52
3.7 Conclusions	52
4 Growth of Indium Nitride Nanocolumns	53
4.1 Motivation	53
4.2 Theory of Nanorod Growth by PA-MBE	55
4.2.1 Vapor-Liquid-Solid mechanism of Crystal Growth	55
4.2.2 Complementary Geometric Growth Model for GaN	57
4.3 Experimental Method	59
4.4 Results	60
4.4.1 Growth of Nanorods	60
4.4.2 Coalescence of Nanorods	66
4.5 Conclusions	74
5 Growth of GaN, InN, and InGaN	75
5.1 Motivation	75
5.2 Anion Modulation Epitaxy	78
5.3 Experimental Method	79
5.4 Results and Discussion	80
5.4.1 GaN Results by AME	80
5.4.2 InN Results by AME	92
5.5 Cyclic temperature changes during AME	94
5.6 Conclusions	99
6 Application of AME for Solar Cells	100
6.1 Motivation	100

<i>CONTENTS</i>	xv
6.2 Results	104
6.2.1 Growth on GaAs	104
6.2.2 Growth on Sapphire	110
6.3 Conclusions	116
7 Summary of Results and Future Work	117

Chapter 1

Literature Review

1.1 Introduction to Nitrides

The III-V nitrides have been viewed for a long time as a promising materials system due to their wide range of potential applications in both electronic and optoelectronic devices. If the wurtzite polytypes of GaN, AlN and InN are considered, then it is easy to imagine fabrication of optical devices ranging from the infrared, well into the UV given the direct bandgap range for these materials(0.67 eV for InN [1], 3.4 eV for GaN [2], and 6.2 eV for AlN [3]).

Another important band occurs at the 240-280 nm range (≈ 4.75 eV) where absorption by the ozone makes the earths atmosphere almost opaque [4]. Imaging array detectors operating in this band would make sensitive surveillance equipment for objects coming up out of the atmosphere if positioned in an area that is shielded from the sun's radiation.

A lot of research has gone into the development of high efficiency blue and UV laser diodes (LDs) and light emitting diodes (LEDs) that can function at room temperature. These nitride devices are favoured over their GaAs equivalents due to AlGa_xN/GaN diodes having a large band band disconti-

nunity at the well walls which leads to stronger recombination overlap and a larger output power density. Nitride based devices are also capable of operating at higher temperatures. GaN based devices are also suitable for use in high power applications. Experiments were carried out on GaN p-n diodes and the breakdown field of GaN was found to be 3.27 MV/cm [5].

Recently there has been a considerable amount of progress in improving the short wavelength LEDs. InGaN/GaN blue LEDs with external quantum efficiencies of approximately 64% [6] have been produced, whereas twenty years ago the highest efficiencies were approximately 7% [7]. Typically, devices have been grown on substrates such as sapphire or SiC, but there are great advantages of using GaN substrates such as a reduced dislocation density and thus improved performance at high injection currents [8]. AlGaIn laser diodes have also been fabricated that emit at UV wavelengths as low as 336 nm with an output power of approximately 3mW [9].

One of the last remaining challenges for improving GaN-based LEDs is to reduce their optical losses[10]. These losses are caused by the relatively high refractive index of GaN (approximately 2.5 [11]). To overcome this difficulty, the low optical reflection from low effective refractive index nanorod arrays could be exploited [12]. GaN nanocolumn arrays have been shown to have the same physical and thermal properties as the bulk GaN crystal[12], making them equally suitable and durable for high-power, GaN-based optoelectronic applications. By analyzing reflectivity interference fringes, it has been quantitatively determined that GaN nanocolumn arrays behave as low effective refractive index transparent media in the entire visible spectra region [10]. Also, the polarized properties of single GaN nanocolumns have been demonstrated and studied in detail [13].

In order to realise general solid state lighting or full colour displays using

high efficiency GaN based LEDs, the efficiency of the light extraction from these devices needs to be enhanced and this is limited by losses due to total internal reflection. At a GaN/air planar interface, the critical angle for total internal reflection to occur is approximately 24° and only 4% of the emitted light can escape from the GaN layer [13]. There has been a lot of ongoing research effort into improving the light extraction efficiency of these GaN based LEDs, for example surface subwavelength texturing [14], and the incorporation of photonic crystals within the LED structures [15, 16, 17]. The main drawback of these methods is the use of lithographic processes that are both costly and complicated, therefore not lending themselves to large-scale applications. Further work is needed in this area to avoid the use of such expensive processes.

1.1.1 Solid State Lighting

The generation of electricity is the main source of energy-related greenhouse gas emissions, and lighting uses approximately a fifth of this output [18]. Incandescent light bulbs may not seem to be the obvious choice for energy savings, but given that the average American house has 45 light bulbs; Canadian houses have 30; and British houses have 25. Let us consider a house with 30 incandescent light bulbs rated at 100 W, then 3000 W is used to light the house. The average light bulb is switched on for 4 hours a day, therefore lighting this house uses 12 kilowatt-hours (kWh) of electricity per day. If all residential, commercial and industrial buildings are considered, then lighting is the second largest user of energy in buildings [19].

Incandescent light bulbs are extremely inefficient and only convert approximately 5% of electricity into visible light. By comparison, energy-saving fluorescent lamps are only approximately 20% efficient so there is a great deal

of room for improvement of lighting efficiency and thus a large amount of energy savings.

Given that lighting is one of the largest causes of greenhouse gas emissions, and the energy used to supply lighting throughout the world results in 1900 megatonnes of CO₂ being emitted per year (assuming the same energy mix based on the 2012 world electricity generation values of 40% coal, 23% natural gas, 16% hydropower, 11% nuclear, 5% oil and 5% from renewables other than hydro, ie geothermal, solar, wind etc.) [20]. This level of CO₂ is equivalent to 70% of the emissions from the worlds cars, and over three times the amount of emission from aircraft [21].

1.1.2 Development of LEDs

Modern commercial LEDs are semiconductor structures that emit light from a quantum well structure that is usually around 2 nm thick. In this case, let us consider an InGaN quantum well (Figure 1.1 [18], this will always be placed between p-type and n-type doped layers (GaN for this example). Figure 1.1 also shows the number of threading dislocations that are present in these structures and these will be discussed in section 1.1.4.

The first reported LED emitted red light and was made from GaAsP in 1962 by Nick Holonyak [22]. The LED shone extremely dimly and was only visible in the dark and had an efficiency of 0.1 lm/W. Ten years later, the efficiency had doubled to 0.2 lm/W but was still only visible in the dark. By 1980, the efficiency was up to 2 lm/W by using an AlGaAs/GaAs quantum well LED and was increased to 10 lm/W by 1990 by using a quaternary semiconductor (AlInGaP/GaAs). By 2000, the quantum well LED was changed to AlInGaP/GaP which increases the efficiency to 100 lm/W.

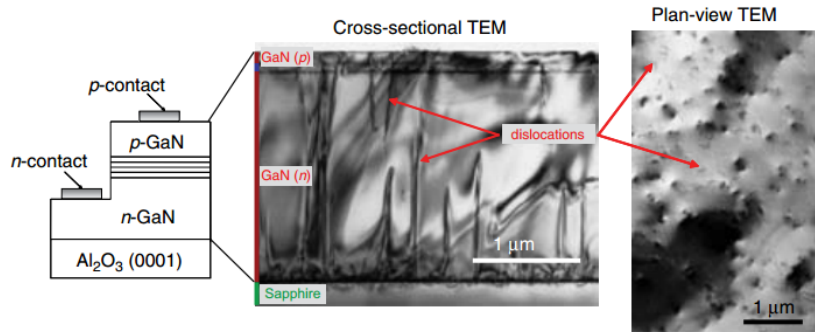


Figure 1.1: Schematic of GaN/InGaN quantum well LED and transmission electron microscope (TEM) images in cross-sectional and plan view, showing the high threading dislocation density which occurs when growing GaN on sapphire. The lattice mismatch between GaN and sapphire is approximately 16 %.

1.1.3 Importance of Gallium Nitride

GaN is arguably the most important semiconductor material next to silicon. The main materials that were used for light emitting devices are shown in Figure 1.2. As can be seen from Figure 1.2(b), many different materials were needed to go from infrared through to blue (InAs to ZnSe) using more than one materials system. Also, despite much research into ZnSe blue light emitting devices, no devices have ever worked. One of the major problems with ZnSe is the defected material quenches the light emission. Green LEDs are also a problem; even though GaP and AlAs both emit at the green wavelength, they have an indirect bandgap which results in a weak emission. Thus, before GaN, bright LEDs could be made from infrared through to yellow, but no green, blue or white were available.

GaN, InN and AlN changed the landscape of LED production dramatically. Figure 1.2(a) shows that the bandgaps of these nitride materials range from 0.67 eV to 6.2 eV for AlN. By using InN, through to GaN, and any InGaN alloys in between, any colour in the visible spectrum can in principle

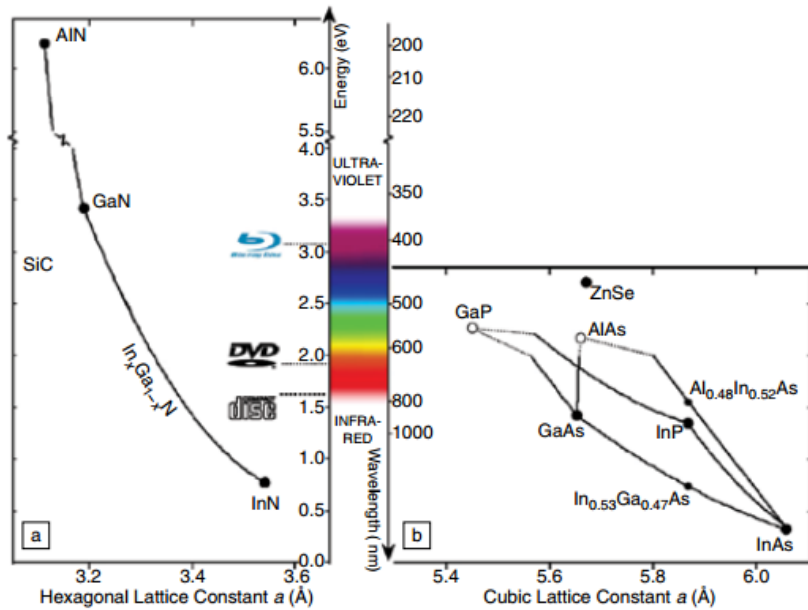


Figure 1.2: (a) Bandgap energies ranging from InN, through GaN and up to AlN. The laser energies for compact discs, DVDs and Blurays are also shown with the visible spectrum. (b) The main materials that were known to emit light prior to the discovery of GaN, solid circles are direct bandgap materials whilst open circles are indirect bandgap materials [18].

be produced as well as IR and UV. This gives us one materials system that can span the whole visible spectrum, which would be advantageous for solar cell production as well as light emission. Solar cells will be considered in chapter 6.

In practice, the intensity of light emission from high indium content In-GaN is weak and this still isn't fully understood. Despite emission from InGaN at blue wavelengths being strong, emission at green wavelengths is less intense and emission in the red very weak.

If GaN is mixed with AlN, then the resulting AlGaIn alloy can emit light from the near-UV to deep-UV. Deep-UV has important applications

including water purification [23, 24, 25], air purification [26, 27, 28, 29] and the detection of biological agents [30, 31, 32, 33, 34, 35, 36, 37].

1.1.4 Why does Highly defective GaN still emit light?

Many nitride-based researchers believed they knew why these highly defective InGaN structures still emitted light: nanometer scale indium-rich nanoclusters within the InGaN quantum wells that localised the carriers and therefore could not diffuse to the dislocations with many basing their beliefs on images from electron microscopes and thermodynamic calculations.

As Figure 1.1 shows in section 1.1.2, the density of threading dislocations is high, largely due to the high substrate and layer lattice mismatch (approximately 16%). Dislocations in GaN are known to be nonradiative recombination centres and will destroy any light emission. Thermodynamic calculations have been carried out and show that InGaN is unstable and will decompose into high-indium and low-indium content regions between approximately 30% and 80% [38]. More importantly, TEM images of the InGaN quantum wells show strained regions on a nanometer scale [39] and electron energy loss spectroscopy (EELS) have determined these regions to be indium-rich [40]. As the InN bandgap is below that of GaN, In-rich regions in the InGaN would confine electrons and holes, and significantly suppress any diffusion to the dislocations. In 2003, it was discovered that these In-rich clusters do not exist, and are just an imaging artefact from using a high electron dose within the TEM [41]. Thermodynamic calculations were also carried out that included the strain that the InGaN wells were under, and these calculations suggested that the strain should suppress InGaN decomposition and the InGaN should remain a homogeneous alloy up until at least 40% In content [42]. Therefore, the emission cannot be due to the In-rich

clusters.

The emerging consensus in the scientific community is that the emission is due to interface effects between the InGaN quantum well and the GaN overlayer, more specifically, monolayer height interface steps on the InGaN (see [43] and references therein). It is also now believed that InGaN is stable as a random alloy with at least 30% indium content and this has been confirmed with three-dimensional atom probe studies that do not utilise electrons for imaging [44]. However, TEM images suggest that the quantum wells contain monolayer height interface steps [45] and has also been confirmed by atom probe studies. As the quantum wells are strained, and there is a high piezoelectric effect in GaN, the interface step produces an additional carrier confinement energy of approximately $3kT$ at room temperature, where k is the Boltzmann constant and T is the temperature, and this is enough to localise the carriers [46].

1.1.5 How to produce solid-state white light

There are 4 main ways to produce white light LEDs:

1. A blue InGaN/GaN LED with a yellow phosphor. The blue LED chip is covered with a phosphor that is excited by the blue light from the LED and emits yellow light and the combination of the blue and yellow produces a white light.
2. Red, green and blue LEDs. Mixing red, green and blue LEDs will produce white light but there are some problems with this method. The efficiency of green LEDs is so small compared to red and blue that the efficiency of this whit LED will be reduced. Also, the efficiencies of the individual coloured LEDs changes over time and at different rates,

so the quality of the white light originally produced will degrade.

3. Red, green and blue quantum dots in a single LED. A single LED could be produced with InGaN quantum dots of different sizes and compositions in order to emit white light.
4. Near-UV or blue LED with red, green and blue phosphors. Blue LEDs with a yellow phosphor are good enough for bicycle lights or interior vehicle lights, but not good enough for home or office lighting. This can be achieved by using a blue LED with yellow and red phosphors to create a warmer light.

1.2 How Nitrides are Grown

There are several different techniques that can be employed for the growth of III-Nitride semiconductors. The most common are metal-organic vapour phase epitaxy (MOVPE), and molecular beam epitaxy (MBE), which can be broken down into Ammonia-MBE (NH_3 -MBE) and plasma assisted-MBE (PA-MBE). MOVPE and NH_3 -MBE will be discussed here whilst PA-MBE will be described in chapter 2 as it is the main technique in this thesis.

1.2.1 Metal-Organic Vapour Phase Epitaxy

Metal-organic vapour phase epitaxy (MOVPE) is a type of chemical vapour deposition method that is used to produce semiconductors. Unlike growth by MBE, the growth of crystals by MOVPE is chemical reaction, rather than physical deposition for MBE. MOVPE will take place under pressures of 10 Torr to 760 Torr, and this is caused by the gaseous precursors used. Conversely MBE will be carried out under vacuum.

In MOVPE, reactant gases are combined inside the reactor at elevated temperatures, this provokes a chemical interaction that results in deposition on the substrate surface. The reactor must be able to withstand the chemicals being used and the high temperatures. Typically the chamber walls will be made of stainless steel and sometimes the inside is lined with ceramic or quartz. The chamber is also water cooled to prevent overheating. The substrate sits on a ‘susceptor’ which is at controlled temperature set by the user. The susceptor is often made from graphite as this is resistant to the metalorganic compounds being injected.

There is also a gas inlet switching system that introduces the gases using ‘bubblers’. The carrier gases are bubbled through the metalorganic liquid which picks up the vapour and transports it to the reactor. The amount of vapour transported is dependant on the flow of carrier gas and the bubbler temperature. There is also a pressure maintenance system and a gas exhaust cleaning system that converts the waste products for recycling or disposal.

1.2.2 Ammonia-Molecular beam Epitaxy

Ammonia-MBE (NH_3 -MBE) is a type of gas source MBE (also known as chemical beam epitaxy) that uses ammonia as the precursor gas solid elemental sources from effusion cells for the group III’s. Ammonia-MBE is often favoured over plasma-assisted-MBE as the growth rate is much higher and closer to the rates used during MOVPE growth [48]. Higher growth rates tend to be favoured as this reduces the number of impurities incorporated into the layer, and therefore there should be less defects within the structure [49, 50].

Typically, pressures during ammonia-MBE growth are approximately 10^{-4} Torr. The NH_3 molecule needs to be ‘cracked’ in order to release the nitro-

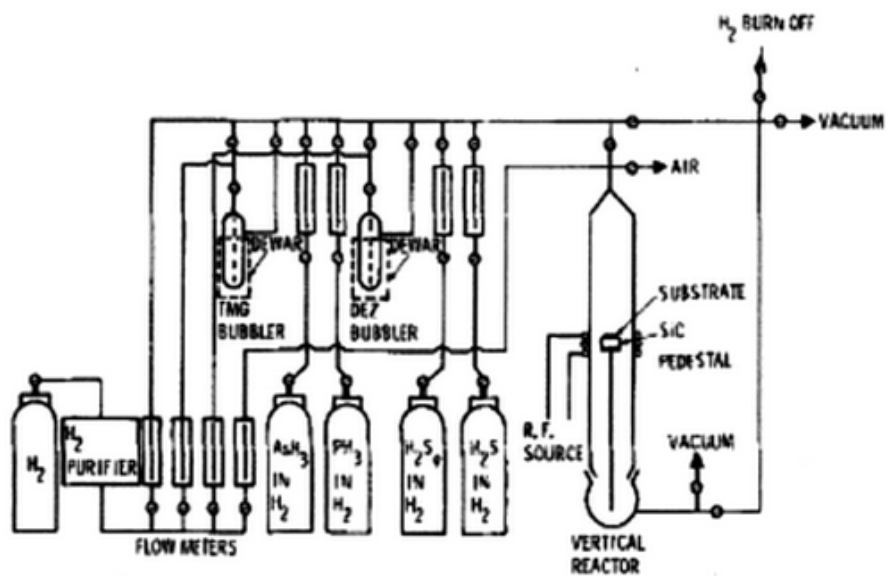


Figure 1.3: Schematic diagram of an MOVPE reactor Manasevit and Simpson to grow epitaxial GaAs and GaP. The group V's are supplied as hydrides and gallium as trimethyl gallium [47].

gen from the ammonia molecule. Temperatures of approximately 500°C are needed to split the molecule so no low-temperature semiconductor growth can be achieved, making indium nitride impossible to grow.

1.3 Growth of Nanocolumns

Semiconductor nanocolumns are fast becoming a key part of the development of future devices as they offer reduced dimensionality, superior material properties, and bottom-up assembly. Over the past decade, research interest has peaked around semiconductor nanocolumns and a wide range of nanocolumn based electronic and photonic devices have been developed including nanocolumn solar cells [51, 52, 53, 54], photodetectors [55, 56, 57], lasers [58, 59, 60, 61, 62, 63], LEDs [64, 65], resonant tunnelling diodes [66], waveguides [67], single photon sources [68], single-electron transistors and memory devices [69, 70, 71, 72, 73], field-emission electron sources [74], field-effect transistors for ultrahigh density logic and memory devices [75, 76, 77, 78], integrated photonic circuits [79, 80], and highly sensitive biological and chemical sensors [81, 82].

The unique geometry of nanocolumns offers large advantages over conventional planar structures; if the nanocolumn diameter is sufficiently small, these structures can then exhibit quantum confinement in two dimensions. The high surface-to-volume ratio of nanocolumns makes them especially suitable for sensing applications, but the nanocolumns can also function as interconnects as well as active device elements. Device architectures of vertical-standing nanowires will also allow ultrahigh density device integration onto a single chip [75, 78].

Additionally, nanocolumns can be tailored into unique radial and axial

heterostructures which increases the range of device capabilities [83, 84, 85, 86]. In axial heterostructures, the narrow nanocolumn diameter will allow the lattice of nanocolumns to expand or contract radially. This mechanism for relaxation within the lattice can relieve strain without encouraging misfit dislocations, but also allows high quality coherent heterointerfaces even between highly mismatched materials [87, 88, 89]. Therefore, nanocolumns are advantageous over planar or bulk materials where lattice-mismatched heterostructures can only be grown if the strained layer is thin and below the critical layer thickness. A wide range of nanocolumn heterostructures have been grown using a range of binary and ternary III-V materials, as well as IV materials such as Si and Ge [90, 91, 92, 93, 94, 95]. Although there are large thermal, chemical and structural mismatches between the materials, high quality crystallographic and optical properties have been demonstrated [90, 92, 93, 96].

A full description of the growth mechanisms involved in III-nitride nanocolumn growth will be presented in chapter 4.

1.4 Conclusions

A brief review of the literature so far with regards to nitride material has been presented here. The importance of the wurtzite polytypes of GaN, AlN and InN have been highlighted and the potential to fabricate optical devices from infrared, all the way through to deep-UV. Solid state lighting has also been reviewed and the importance of the development of LEDs through the visible range. Electricity generation is the main source of energy-related carbon emissions, thus the introduction of LED lighting could potentially save millions per year and also slow down any damage to the ozone.

Gallium nitride is an important discovery as it gives us the potential to produce devices using one materials system. The alloys of GaN, InN and AlN can be used for many applications such as LEDs, solar cells, water purification, air purification and the detection of biological agents.

The debate over how and why defective GaN has also been explored. It was believed that emission was due to In-rich clusters within the InGaN layers but it is now widely believed that the emission is due to interface effects between the InGaN quantum well and the GaN over-layer.

Other growth techniques such as MOVPE and NH_3 -MBE have also been outlined as alternatives to MBE. Also, the importance of altering growth parameters to produce nanocolumns has been considered. Nanocolumns have the advantage that they can be tailored into unique radial and axial heterostructures, and this increases the range of devices that can be produced.

Chapter 2

Experimental Techniques

2.1 Molecular Beam Epitaxy

Molecular beam epitaxy (MBE) is an ultra high vacuum (UHV) technique that grows single crystals via the interaction of molecular beams on the surface of a crystalline substrate. It offers the control to ‘grow’ with monolayer precision, as well as giving a good uniformity across a surface and high purity structures. It also gives the user the ability to dope films n and p-type, and also produce heterostructures with precise control of thickness [97], [98].

2.1.1 Description of Equipment

A typical MBE machine is shown in Figure 2.1 [99]. It consists of a growth chamber with a nitrogen cooled cryopanel surrounding the substrate and heater and several effusion cells pointing towards the substrate. All of the cells have a shutter associated with them so that they can be opened or closed depending on the layer that is being grown. The shutter opening or closing time is short compared to the time to deposit a single mono/bilayer, hence the precise thickness control. A reflection high energy electron diffraction

(RHEED) gun and screen are positioned so that the RHEED beam can reflect from the surface at a shallow angle ($\approx 1^\circ$) and diffraction can be obtained throughout the growth. This will be described in more detail later in this chapter. There is also a Bayert Alpert ion gauge that can be placed in the path of the beam to measure the beam equivalent pressures (BEPs) of a given atomic/molecular beam. A beam is produced by heating the cell up to a given temperature where the material will evaporate/sublimate. The flux of material produced from each cell is then controlled by adjusting the cell temperature.

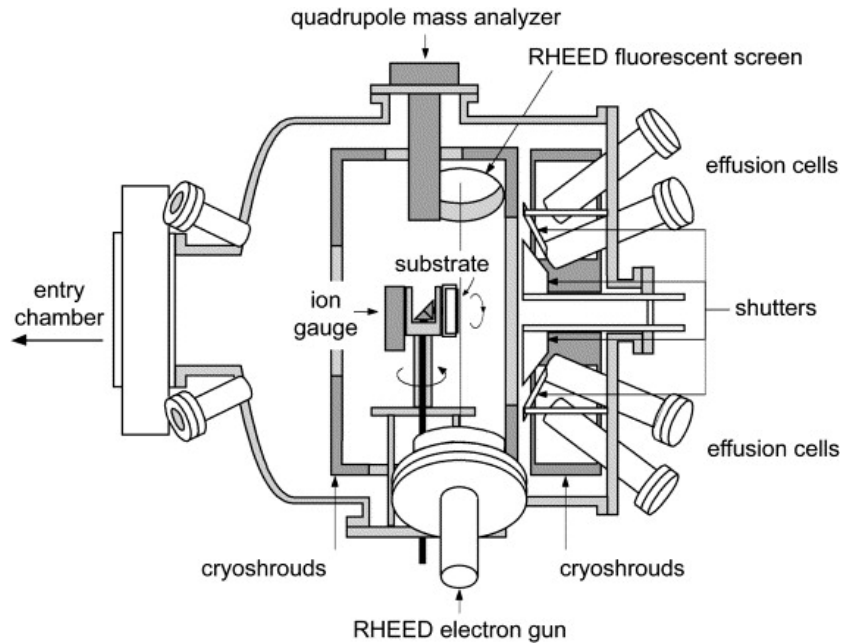


Figure 2.1: Schematic of an MBE machine taken from Franchi 2003 [99].

During growth, the shutters of the required element(s) are opened, allowing the atomic/molecular beam to land on the heated substrate. These beams of atoms/molecules are collision free as the distance to the substrate is less than the mean free path of the particles. At approximately 10^{-7} torr (background pressure), the mean free path of a molecule is approximately

500 metres. The pressure rises to $\approx 5.0 \times 10^{-5}$ torr during the growth of nitrides. The mean free path is now reduced to be approximately the same as the distance the beam travels to the substrate. So there are some collisions with atoms before the beam reaches the surface.

When the atoms/molecules arrive at the substrate they can adsorb on the surface, migrate across the surface, be incorporated into the growing crystal or desorb from the surface. If the right conditions are employed within the system, then the film will grow and build up monolayer by monolayer. This is known as Frank van der Merwe [100] growth which is a two-dimensional layer by layer growth mode. Volmer-Weber [101] and Stranski-Krastanov [102] growth modes can be employed for 3-dimensional layers. These will be discussed in more detail later in this chapter.

The substrate will act as a seed crystal for the deposited layer. Generally the layer takes on the crystal structure and orientation of the substrate. If the layer is the same composition as the substrate, and has the same crystal structure, then the growth is known as homoepitaxy, otherwise it is heteroepitaxy. Homoepitaxy is the preferred growth method as the crystal quality is often higher. Unfortunately, this is not always possible as for some materials, substrates are not commercially available or are very expensive.

When choosing a substrate, several factors need to be considered; the lattice parameters of the substrate and of the grown material, orientation, the cost of the substrate, preparation, and doping. Generally it is a compromise between achieving good crystal quality (a high lattice mismatch results in strain and eventually defects) and the cost of the material.

The substrate is mounted onto a holder which is heated to the growth temperature and usually rotated throughout the growth. Rotation helps the materials from the cells to be deposited more evenly across the surface. Ide-

ally at least one rotation per monolayer incident upon the surface is needed.

High purity films are often required, which is why the ultra high vacuum is needed. This requires everything within the system to be outgassed and for there to be no leaks. To illustrate this point, the partial pressures of an impurity such as oxygen can be considered. If an incorporation rate of 100% is assumed, the partial pressure is 10^{-10} torr for the impurity and 10^{-7} torr for Gallium:

$$\text{Impurity mole of fraction} = \frac{10^{-10}}{10^{-7}} = 0.1\% \quad (2.1)$$

In GaAs there are 2.2×10^{-22} Ga atoms in a cubic centimetre, 0.1% of this is 2.2×10^{-19} oxygen atoms per cubic centimetre. Typically, a highly doped GaAs layer will contain only 2.0×10^{-18} of the dopant atom in a cubic centimetre and an unintentionally doped crystal will have a doping level of $\approx 10^{-15} \text{ cm}^{-3}$.

Typically there are preliminary chambers where substrates are loaded and can be prepared in situ before being put in the main growth chamber. Preparation usually involves out-gassing of the substrate so that a minimal amount of impurities are introduced into the main chamber. This is important when high purity films are being grown as a clean vacuum chamber is paramount. It is now common for chambers to be added for post-growth analysis so there is no need for a substrate to be exposed to the atmosphere.

The liquid-nitrogen-filled cryopanel ensures UHV conditions before the growth, remove excess heat radiating from the cells, and isolate each one. As the panel is cold, any re-evaporation of material from the growth surface or heater will stick to the cryopanel during growth, keeping the background vacuum pressure low.

The UHV environment allows the use of equipment such as a quadrupole

mass spectrometer [103] which, monitors the vacuum chemical environment and a RHEED gun. These have become the standard on MBE machines.

2.1.2 Machine set-ups

Two different MBE machines were used to carry out the work described in this thesis. One is a small ‘mini’-MBE system that was built at the University of Nottingham and the other is a commercial Veeco Gen III system.

The main bulk of all of the research reported in this thesis was carried out on the ‘mini’-system. Once all the key parameters for the research were established, the technology was then transferred over to the Gen-III to produce higher quality samples.

‘Mini’-MBE System

This system has a base pressure of approximately 10^{-10} mbar. It has five ports, two of which permanently house a Ga cell and an Oxford Applied Research RF plasma source to provide active nitrogen. The other three are generally filled with indium, magnesium (for p-doping of GaN) and aluminium. One of the ports has the facility to house a high temperature cell to allow the use of very low vapour pressure elements eg. scandium for ScN.

Samples are mounted on a disc of tantalum with a cut-out just less than the wafer size and held in place by small wires as shown in Figure 2.2. This means that the back of the substrate faces the substrate heater.

The work described in chapters 4 and 5 was performed before any modifications had been made to the mini-system. This means that these growths were carried out without the sample being rotated continuously throughout. The sample, however, could be rotated manually during the growth to look at the different azimuths via RHEED.

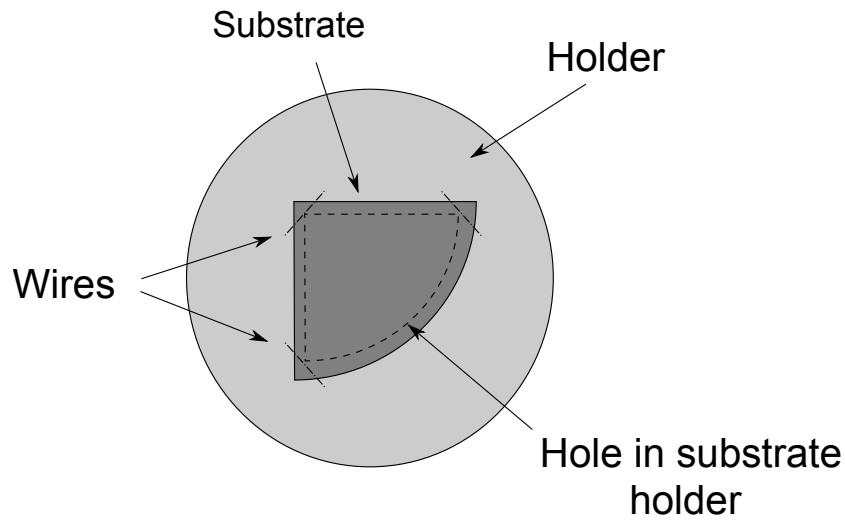


Figure 2.2: Schematic of the holder used within the ‘mini’-system.

Modifications

The ‘mini’-system underwent maintenance and upgrading during the course of this PhD to install a rotating stage. It was also decided to adapt the mounting plates to be compatible with both the Veeco Gen-II and Gen-III machines. First, the substrate holder within the machine was modified to allow the new plates to be used. Second, the mounting to the transfer arm was also redesigned. An extra arm has been added to the machine to act as a stabiliser for the transfer arm and the whole transfer method has been made electronic. This involved gearing up and down the handles originally used for transfer in order for the new electronics system to cope with the torque. This has resulted in a much more user friendly system.

Veeco Gen-III

Commercial systems tend to have a base pressure around 10^{-11} Torr. This system has 14 ports in all, two below the source flange that are used for dopants, with the remaining 12 ports around the source flange are used for

effusion cells, a Veeco plasma source and an arsenic cracker. There are two Ga cells permanently housed in these ports along with one each for aluminium, indium, magnesium and manganese. The other cells are changed depending on the selected growth objectives of a campaign.

In this Veeco system the sample can be mounted with the method used for the ‘mini’-system (hollow backing plate) but often a pyrolytic boron nitride (PBN) backing plate is used. At growth temperatures of approximately 200-300°C, the PBN plate appears to improve the radiative coupling mechanism so that more heat is coupled to the substrate than when it is not used. There appears to be little difference whilst growing at higher temperatures.

Both machines are equipped with a mass spectrometer, a RHEED gun and screen, and a k-space BandiT temperature monitoring system. RHEED and substrate temperature measurement will be discussed in detail later in this chapter.

Machine differences

Along with being a much smaller MBE system, the other key difference between the ‘mini’-system and the commercial systems is the lack of buffer chamber between the load lock and the main growth chamber.

One important thing to point out is that both systems are equipped with a plasma source. Ammonia gas can be used as a source of Nitrogen within MBE but at high temperatures it causes some metals, including aluminium to creep out of the K-cells. During all studies in this thesis, nitrogen gas has been used as a source. There is however one problem with using a plasma source; it is not known exactly what species are produced and which of these are active. Some experimental evidence suggests that the active species could be excited molecular nitrogen, but there are also strong arguments for it

being atomic nitrogen [104]. It seems that there is not yet any conclusive evidence that either theory is wrong and it is still a topic for debate. Indeed, the active nitrogen species may vary depending on the source design and operating parameters. The kinetics energy of the species impinging on the growing surface can also have an effect; if the energy is too high then damage will be caused to the surface [105] [106] [107], and if the energy is too low then there will not be a vigorous enough chemical reaction to allow the layer to grow [108] [109].

2.2 RHEED

The vacuum environment allows the RHEED technique to be used throughout growth to study the surface. This reveals information about the sample that cannot be seen just by looking through a view port.

The geometry of the system is shown in Figure 2.3 [110]. The electron gun and screen are placed on opposite ports of the chamber so that a grazing incidence of the electron beam on the sample surface can be achieved. The diffracted electrons from the substrate surface provide information about the top layer and produces a real-time picture of the growth of the crystal. The low angle of incidence (5° or less) results in a small penetration depth of only a few atomic layers before total external reflection occurs and the electron is diffracted out of the crystal. Thus, RHEED is an analysis method that is both real-time and non-destructive. In the ‘mini’-system, the electron beam is given 12 keV of energy.

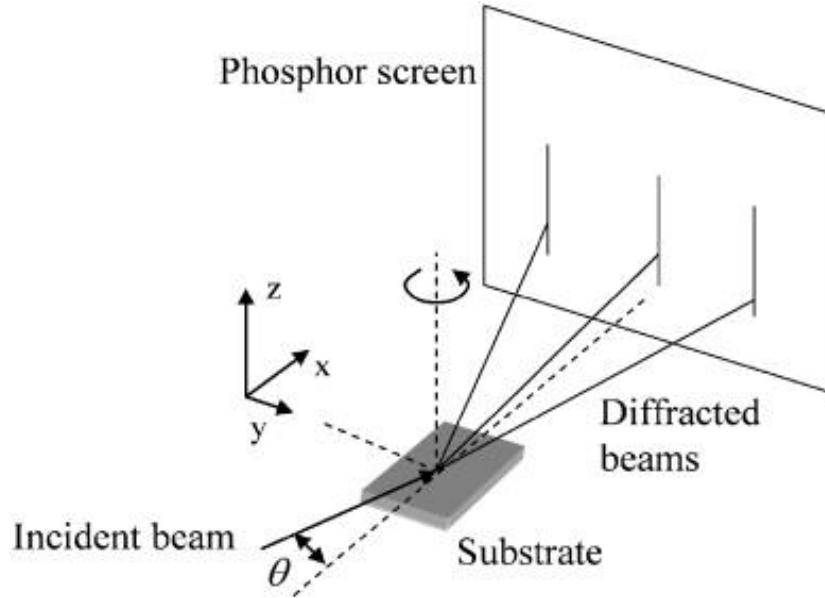


Figure 2.3: Schematic view of the RHEED geometry.

2.2.1 Theory of RHEED

The RHEED pattern that is used so often during MBE growth is essentially an image of the reciprocal lattice of the surface along an axis. If the RHEED beam is directed along the $[111]$ axis, the electrons are diffracted from the $\bar{1}11$ axis. The possible reflections that can be observed are determined by the condition that the reflected wavevector \mathbf{k}_f is equal to the sum of the incident wavevector \mathbf{k}_i and the reciprocal lattice vector \mathbf{G}_{hkl} .

The sample can be considered to be a two-dimensional layer, so the lattice can be reduced to a set of one-dimensional rods in reciprocal space aligned perpendicular to the sample surface. A reflection occurs in the diffraction pattern when these rods intersect with the Ewald sphere. It has a radius of length $2\pi/\lambda$ which is equivalent to the length of the incident plane wave's wave vector (\mathbf{k}_i). The diffraction process is assumed to be elastic so the scattering vector (\mathbf{k}_f) will also have a wave vector of $2\pi/\lambda$. The Ewald sphere

is superimposed onto the map of reciprocal lattice vectors to determine which conditions will lead to diffraction as shown in figure 2.4.

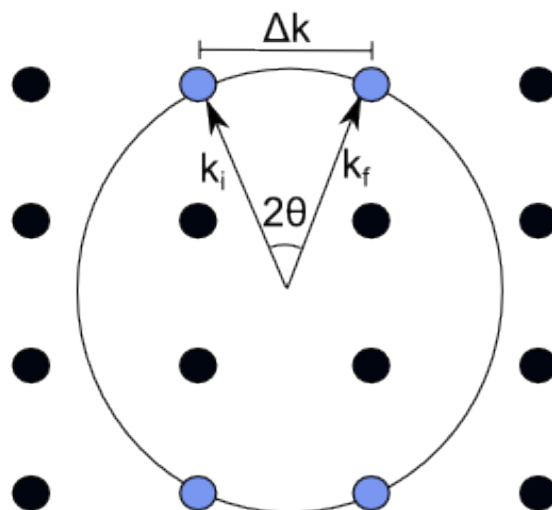


Figure 2.4: A 2D representation of the Ewald sphere.

At 10 keV, $\lambda=0.037$ nm and $k_i=170\text{nm}^{-1}$, which makes the radius of the Ewald sphere large in comparison to the wavelength of the electron. This requires changing the diffraction geometry in order to explore all of the reciprocal lattice rods. As the sample is rotated, the azimuth angle changes and simple diffraction patterns can be viewed when the incident beam is along a direction of high crystal symmetry.

If the electron beam only interacted with the top atomic layer of the surface, and this was perfectly flat and ordered, the three-dimensional reciprocal lattice points would transform into into parallel, infinitely thin rods. In reality, the reciprocal lattice rods have a finite thickness because of thermal vibrations and lattice imperfections. A near flat surface results in a RHEED image consisting of a series of streaks as illustrated in Figure 2.5

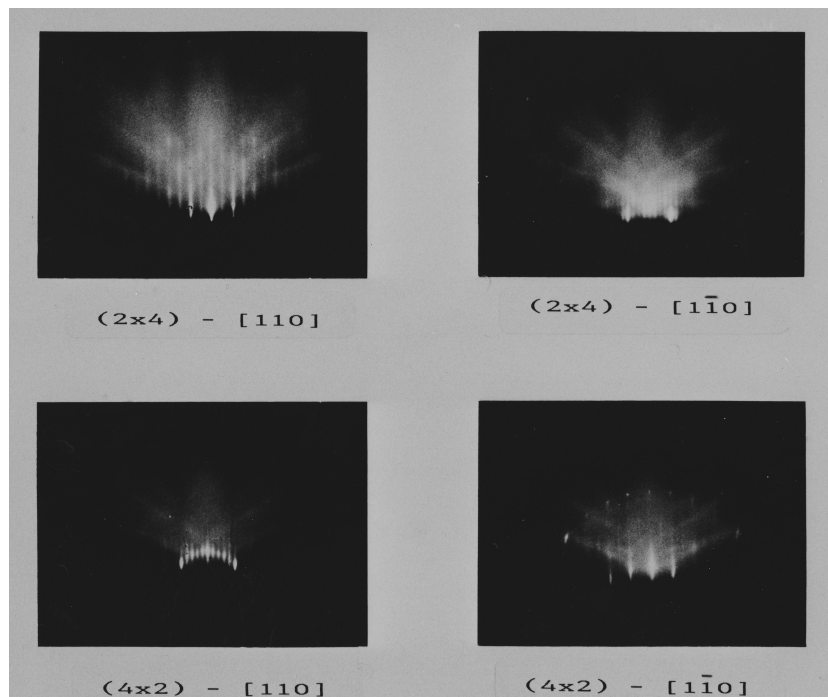


Figure 2.5: RHEED images taken during different surface reconstructions of GaAs.

If the surface is not flat, the electrons will be scattered in different directions. This leads to a RHEED pattern with many spotty features. Therefore, the first thing that is determined from a RHEED pattern is how smooth or flat the surface is.

Another point to note is that new substrates often have an amorphous oxide on the surface. This gives rise to no diffraction pattern, just a grey diffuse scatter. However, as the substrate is heated ready for growth, the oxide is removed and the underlying pattern from the crystal surface becomes visible. This allows us to know when the surface is clean and ready for growth.

2.2.2 Surface Crystallography

The RHEED image can also provide details of the surface structure as well as basic topographical information. When discussing the surface, the top

few atomic layers (monolayers) are what are being referred to. These surface atoms are able to move with respect to the bulk structure and tend to not be in the positions expected from a simple termination of the bulk. Atoms at or near the surface can either move normal to the surface or both perpendicular and parallel to the surface. A movement perpendicular to the surface is a relaxation of the lattice, whilst movement both perpendicular and parallel to the surface results in a reconstruction of the bulk structure. This is demonstrated in Figure 2.6.

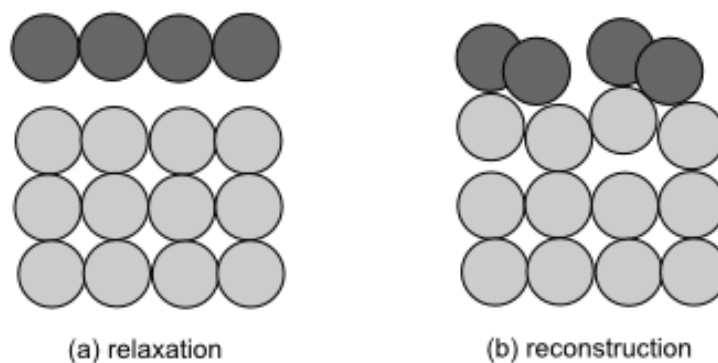


Figure 2.6: Schematic of how atoms at the surface can exhibit a different structure to the bulk, (a) showing a relaxed and (b) showing a reconstructed surface.

In relaxation, the top layer of atoms relax inwards or outwards from the surface. This means that the layer spacing on the surface will be different from the layer spacing within the bulk. This effect is not observed routinely on densely packed structures, but is found on more open channelled surfaces. Relaxation is common in metals because of the overflow of electrons into the vacuum.

Reconstructed surfaces are formed by the atoms moving both parallel and perpendicular to the bulk in order to gain the lowest energy configuration

possible. Bonds that would otherwise be used to join to atoms in the missing layers above are now used to bond atoms together along a row. This causes the atoms to move out of their bulk crystal positions. Reconstruction is more common in semiconductors where atoms are generally bonded together using covalent bonds. It also occurs in metals that have highly directional electrons such as gold which possess d and f electrons. The surface reconstruction observed depends on the material, the surface orientation and the surface termination, which can all depend on the temperature of the sample and whether there are any ambient gases within the chamber.

To describe the arrangement of atoms at the surface of the semiconductor sample, a , b and c nets are used, and all of these are Bravais lattices. The a net in this case describes the Bravais net that is associated with the surface and has a unit mesh that can be described by vectors \mathbf{a}_1 and \mathbf{a}_2 as shown in Figure 2.7. If atoms, molecules or adatoms are adsorbed onto a surface and are viewed on their own, they can sometimes form a regular structure that is called the b net. When the adsorbed adatoms and substrate atoms are considered together, this forms the c net.

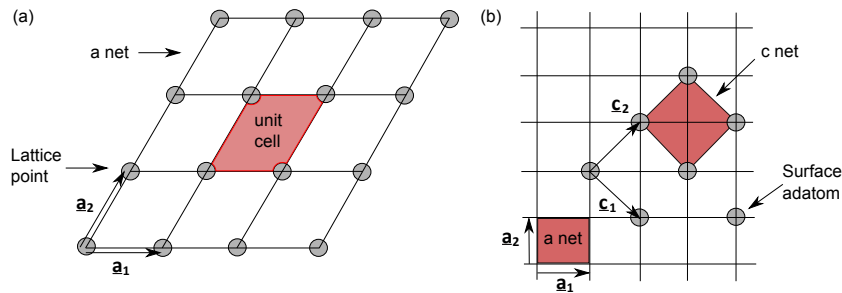


Figure 2.7: 2D structures are described using Bravais nets. (a) a nets are used in order to describe unreconstructed surfaces. (b) a and c nets are used in order to describe the overall surface structure, where atom arrangements on the surface differ to those in the bulk structure.

When trying to describe reconstructed surfaces, ‘out of position’ atoms at the surface are often described as foreign atoms that have been adsorbed to the surface. This then allows the bulk material to be described by the *a net* and the surface reconstruction by the *c net*. Wood notation is then used to describe the relationship between the *a net* and the *c net* and can be expressed as:

$$\text{Substrate}(\text{Millerindex}) - w[(b_1/a_1)x(b_2/a_2)]R\theta - N\text{adsorbate} \quad (2.2)$$

where *w* is the type of unit cell (*p* is used if primitive or *c* if a centred unit cell as shown in Figure 2.7). The angle of rotation between the *c net* and the *a net* is described by $R\theta$ and *N* describes the number of adsorbate molecules in the unit cell followed by the chemical symbol of the adsorbate. If describing a reconstructed surface, then the *N adsorbate* can be omitted, $R\theta$ will be omitted if there is zero rotation between the *c* and *a nets*, and *w* is often omitted if the unit cell is primitive. Examples of reconstructions and their Wood notation can be found in Figure 2.8.

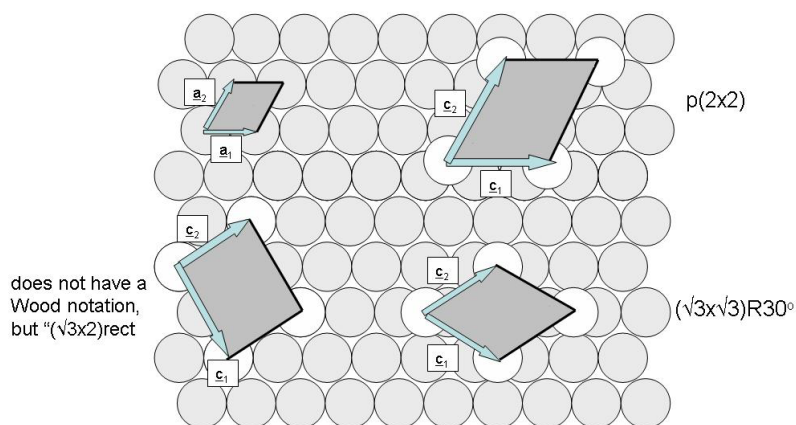


Figure 2.8: Surface reconstructions and their Wood notations [111].

As discussed earlier in section 2.2, RHEED gives the user a diffraction

pattern that is a picture of the surface in reciprocal space, so in order to relate the diffraction image to a real structure, the relationship between a Bravais net in reciprocal space and real space needs to be understood. Let us describe the a net as a^* in reciprocal space with translation vectors \mathbf{a}_1^* and \mathbf{a}_2^* . The translational vectors of the real and reciprocal space nets are related by:

$$\mathbf{a}_1^* \cdot \mathbf{a}_1 = 1 \quad \mathbf{a}_2^* \cdot \mathbf{a}_2 = 1 \quad \mathbf{a}_1^* \cdot \mathbf{a}_2 = 0 \quad \mathbf{a}_2^* \cdot \mathbf{a}_1 = 0 \quad (2.3)$$

This means that while \mathbf{a}_x^* is perpendicular to \mathbf{a}_y^* , \mathbf{a}_x^* and \mathbf{a}_x will have a reciprocal relationship as demonstrated in Figure 2.9. These equations are true of all Bravais nets and allows us to easily swap between reciprocal and real space. In reciprocal space, the larger repeating pattern relates to the a net and the smaller repeating pattern relates to the c net as shown in Figure 2.9.

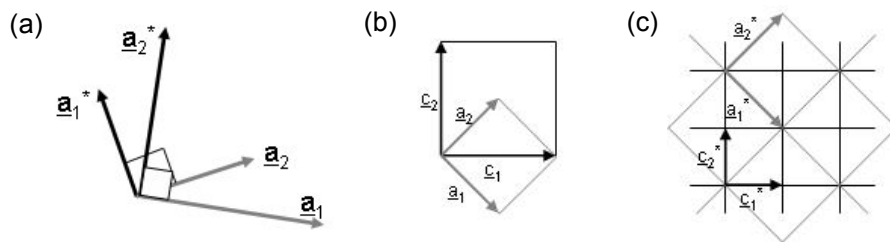


Figure 2.9: Translation between real and reciprocal space. (a) Schematic of the relationship between real vectors describing a unit mesh (\mathbf{a}_1 and \mathbf{a}_2) and their equivalents in reciprocal space, (b) a unit mesh in real space, and (c) the relation between a unit mesh in real space and reciprocal space [111].

2.2.3 Growth Rate Determination

The RHEED pattern can often be used to determine the growth rate of the sample. When a growth is initiated, the intensity of the features within the RHEED pattern begins to oscillate. As the the growth progresses the oscillations are damped and then once the growth has stopped, the intensity of the RHEED returns back to almost the same level of brightness as before growth. Harris et al. first reported these RHEED oscillations in 1981 [112] and they reported two important findings. First, that the period of the oscillations corresponds to the amount of time taken for a monolayer to be deposited, and second that the period does not depend on the growth temperature.

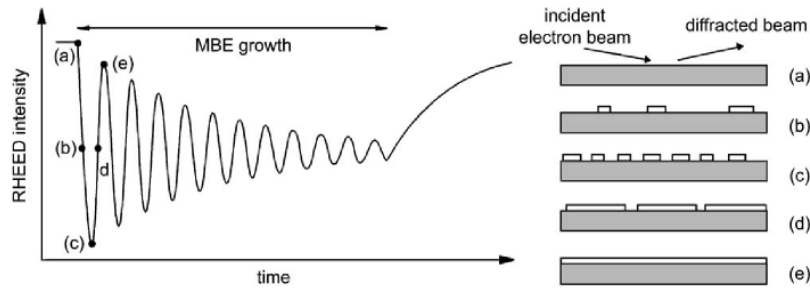


Figure 2.10: Different stages of the layer-by-layer growth by nucleation of 2D islands and the corresponding intensity of the diffracted RHEED beam [113].

With reference to figure 2.10, when the growth has commenced (a), the number of 2D islands on the surface and therefore the number of step edges increases (b) until it reaches a maximum (c) which is a minima in the intensity of the RHEED. As growth continues the islands start to coalesce which reduces the step density (d) and increases the spot intensity of the RHEED, until the surface is completely covered (e) and a maximum RHEED inten-

sity is reached. This results in the diffracted beam intensity increasing to its maximum value where the process is repeated over. RHEED oscillations are used to determine the growth rate on a daily basis in the Gen III.

2.3 Temperature Monitoring during Growth

The mini-MBE system as well as the Gen-III are fitted with a k-Space Associates (kSA) BandiT. This comprises of a lamp and a sensor that can be fitted to the machine on top of two window ports. It provides the user with a real-time measurement of the substrate temperature, without physical contact with the surface as is explained later in this section. Traditionally, a thermocouple in the substrate heater or a pyrometer was used to acquire the temperature, however the thermocouple only reports what is happening to the heater because of the placement of the thermocouple.

The heater configurations currently used in the machines for sample growth are shown in Figure 2.11 a) and b). The Gen-III has a thermocouple that is isolated from the heater by a heat shield. The heat shield extends beyond the heater towards the substrate with the aim that only radiated heat from the back of the substrate should reach it. In reality, the thermocouple undergoes significant heating directly from the heater. This has been tested by heating up the system without a substrate present. The thermocouple still measures a temperature rise even though there is no substrate for radiated heat to come from.

The ‘mini’-system has an entirely different set up. The thermocouple is placed the same distance behind the heater that the substrate is placed in front of the heater. This seems a more feasible arrangement as they should see equal heat fluxes on either side of the heater. However, the thermocouple is

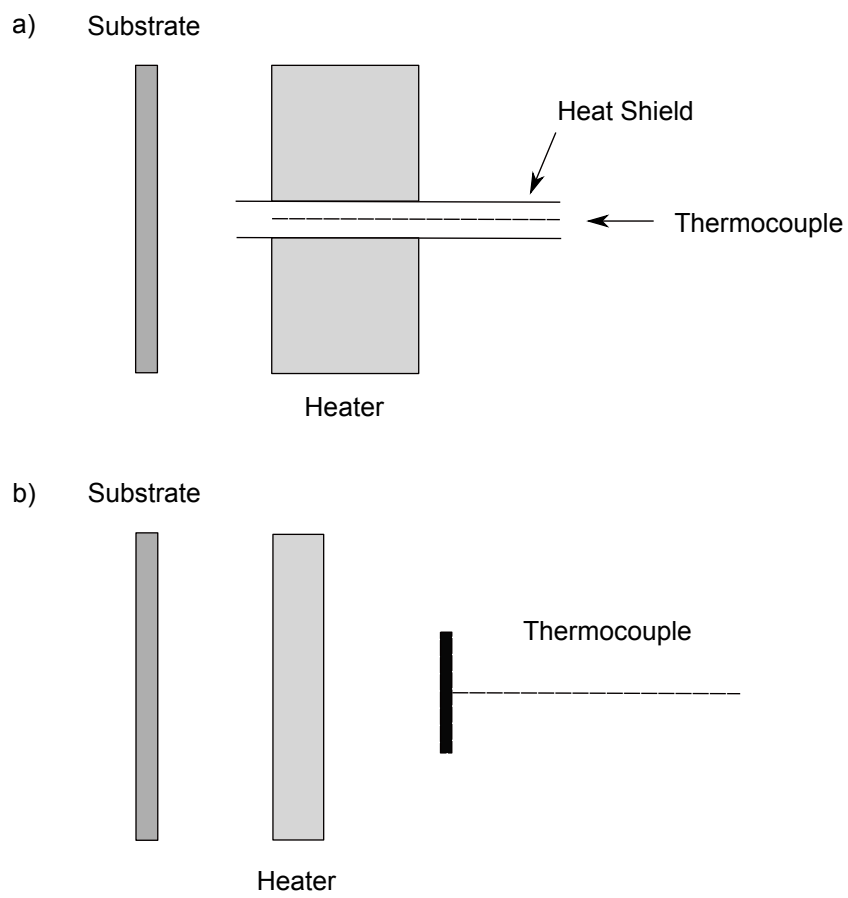


Figure 2.11: Schematic of the heater configurations in a) the gen III and b) the 'mini'-system.

only exposed to the loading mechanism in the machine, whereas the substrate is exposed to heated k-cells. Also, in both cases, the thermocouples will not have the same emissivity as the substrates. This will change how much the substrate is heated compared with the thermocouple even though the same amount of power is input to each.

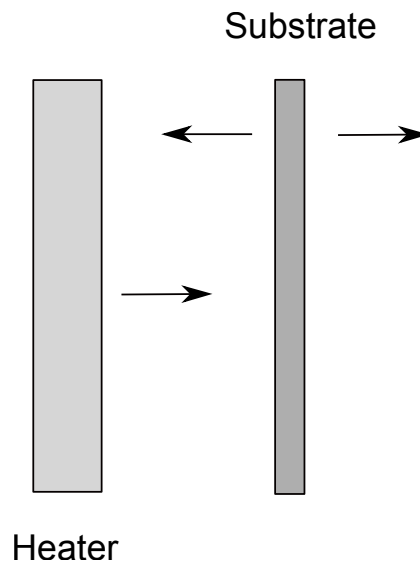


Figure 2.12: Schematic of the heat transfer within the system. Arrows indicate heat flow.

Figure 2.12 is a schematic of the heat flow within the system with the arrows indicating the direction of any heat flow. Heat is given out from the heater and absorbed by the substrate. The substrate then emits heat back towards the heater but also through the other side and into the system. A heat flow equation can be constructed and for simplicity, the emissivity of the heater and the substrate have not been considered.

$$\sigma T_H^4 - \sigma T_S^4 = \sigma T_S^4 \quad (2.4)$$

$$\frac{T_S}{T_H} = \sqrt[4]{\frac{1}{2}} \quad (2.5)$$

$$\approx 0.8 \quad (2.6)$$

where σ is the Stefan-Boltzmann constant, T_H is the temperature of the heater and T_S is the temperature of the substrate.

This equation has led to the conclusion that the highest temperature the substrate will reach is 80% of the heater temperature, but in reality it will be much lower when the emissivity of the materials have been considered.

Pyrometry is a reliable method when the growth temperature is greater than 500°C. However the emissivity of the material has to be known in order to derive the temperature and this can be problematic when growing new materials where many parameters are unknown. Indeed, emissivity will often change during growth for example due to doping.

2.3.1 BandiT

The BandiT determines the temperature of the substrate by monitoring the bandgap of the substrate material. This dependence can be described by Varshni's equation [114]:

$$E_g(T) = E_g(0) - \frac{\alpha T^2}{T + \beta} \quad (2.7)$$

where $E_g(0)$, α and β are parameters that are material dependent.

As the temperature of a material is increased, there is an increase in amplitude of the atomic vibrations. This leads to an increase in the interatomic spacing of the crystal, thus reducing the electric potential that is experienced

by the electrons. So as the temperature increases, the bandgap energy must decrease.

The BandiT measures the wavelength of the material's absorption edge from the fact that semiconductors are transparent when $h\nu < E_g$ and opaque when $h\nu > E_g$. From this the bandgap energy of the semiconductor can be determined and in turn the substrate temperature.

Measurement of the absorption edge is carried out using diffusely scattered light from the sample. This can either come from the substrate heater directly (transmission mode), or light can be shone onto the surface using a kSA light source mounted on a second port (reflection mode). The detector collects the spectrum of data which undergoes a fitting procedure in order to determine the cut-off wavelength or energy and so the temperature. A real-time temperature display is available which can be constantly monitored throughout growth. Generally, the materials grown by MBE are thin, so we assume that the temperature of the grown layer is the same as the substrate. Figure 2.13 is a schematic of the BandiT setup.

The BandiT system is only dependent on the bandgap of the substrate which is advantageous over other methods such as pyrometry. It also means it can be used during growth and etching of the material, as well as allowing for standardisation of measurements between MBE machines. Deposition of material on the viewport does not produce an inaccurate temperature reading as attenuation of the signal can be compensated for over a wide range of signal loss. Also, calibration data can be collected for a given type of substrate outside of the vacuum eg. in a black body oven configuration.

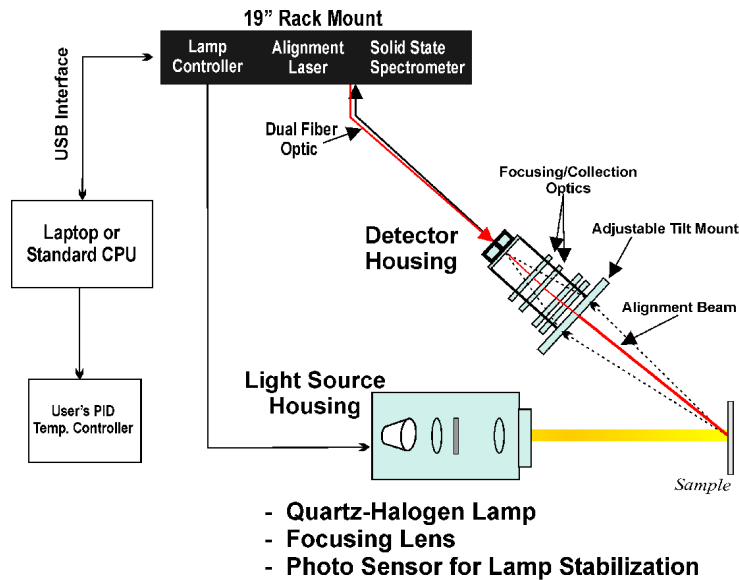


Figure 2.13: Schematic of the *kSA BandiT* product setup taken from www.k-space.com.

2.3.2 Pyrometry

A pyrometer is a non-contact way of acquiring the temperature just like the BandiT (explained in the next section). It measures the thermal radiation from the substrate and uses this to produce a temperature reading. The pyrometer uses an optical system to focus the thermal radiation onto a detector, the temperature T can then be determined using the Stefan-Boltzmann law:

$$I = \varepsilon\sigma T^4 \quad (2.8)$$

where I is the irradiance, ε is the emissivity and σ is the Stefan-Boltzmann constant.

Pyrometry is a reliable method but there is an error associated with each temperature measurement due to readings being taken through a window of the vacuum system. This window can become coated over long periods

of time which alters the effective emissivity and makes it difficult to put a numerical value on the uncertainty of the measurement.

2.4 Growth Mechanisms

The growth mechanisms for MBE samples are shown in Figure 2.14. These are described in more detail in the following sections (2.4.1 and 2.4.2).

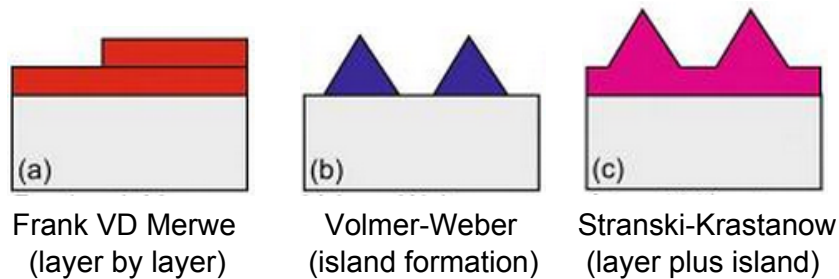


Figure 2.14: Schematic of (a) Frank van der Merwe (FVDM or layer by layer growth), (b) Volmer-Weber (VM or island formation growth), and (c) Stranski-Krastanow (SK or layer plus island growth) growth modes that can be utilised during MBE growth.

2.4.1 2D Growth

There are two types of 2D growth mode; layer-by-layer and step-flow. The former mode means that one layer of atoms is completed before any material is deposited in the next layer to be formed on top. This occurs when the surface migration length λ of the adsorbate is shorter than the mean distance between islands. During this type of growth, some incoming atoms will reach step edges and be incorporated within the island, whilst others will form islands on top of the already existing ones. This regime gives rise to RHEED oscillations that are readily used to determine the growth rate.

The latter mode occurs when λ is much larger than the mean distance between islands. This means that the metal atoms can easily reach a step edge and thus the existing islands expand. The number of step edges remains constant throughout this regime and so oscillations in intensity do not occur in the RHEED measurements. These layer-by-layer modes are also known as Frank van de Merwe growth [100].

2.4.2 3D Growth

This mode is known as island growth or Volmer-Weber (VW) growth and it occurs when islands of material are formed on the surface [101].

3D growth generally occurs under two different conditions:

1. There is a lattice mismatch between the substrate and the layer.
2. The temperature is low enough that migration on the surface is inhibited.

When there is a lattice mismatch, initially the layer will grow via a 2D mechanism, and will be under strain. Once a critical layer thickness has been reached, 3D islands will form, and this change in surface morphology manifests itself as spots in the RHEED pattern rather than the streaks seen for 2D growth. The RHEED pattern can also develop ‘arrow head’ shapes at the spot positions which appear when the islands develop facets. This intermediate layer-plus-island growth mode is known as Stranski-Krastanov (SK) 3D growth. The 2D-to-3D growth transition is a result of the relaxation of the elastic energy which builds up as the thickness of the mismatched layer is increased [99].

At very low temperatures, the surface will be flat and 3D growth does not occur. This is because the surface atoms have zero mobility so can not move

across the surface. The smoothness of the surface depends on the arrival rate which is constant across the sample.

An important difference to note between SK and VW growth is that in the VW regime the surface migration lengths of the adatoms are reduced. This leads to a high nucleation rate and low lateral spreading. In the SK regime, the nucleation rate is initially slow and lateral spreading of the monolayer islands diminishes, but the nucleation rate subsequently increases [115].

2.5 Conclusions

This chapter has described the set up of both MBE chambers used for the work in this thesis. The differences between the Gen-III and the ‘mini’-MBE system have been outlined, along with the improvements that have been implemented to the ‘mini’-system during this PhD.

There are various in-situ techniques that have been outlined in this chapter, that are utilised during the growth of semiconductors. These are all used to reveal details about the crystallographic structure (RHEED), and the substrate temperature (pyrometer and BandiT). Without these, semiconductor growth of devices would be almost impossible.

MBE can be used to grow materials via 2D (Frank van der Merwe and Stranski-Krastanow) or 3D (Volmer-Weber) growth modes and the differences have been outlined in this chapter.

Chapter 3

Characterisation Techniques

3.1 X-Ray Diffraction (XRD)

X-rays are part of the electromagnetic spectrum with a wavelength between 1 and 10 Å. This is comparable with the atomic separation within crystals and makes them ideal for probing crystallographic structure. X-rays are produced when an electrically charged particle with a high enough kinetic energy is rapidly decelerated, normally by a collision, causing an x'ray to be emitted. These charged particles are usually electrons, and are accelerated using a high potential difference, and decelerate when they hit a target.

All of the diffraction experiments have been carried out using a Philips X'pert high resolution X-ray diffractometer. The x-ray tube has a tungsten filament and a copper anode. The filament is heated, which generates free electrons. These are then accelerated towards the copper anode where they can eject electrons from the inner shells of the target atom. These vacancies are quickly filled by electrons dropping down from higher levels and emitting an x-ray in the process. In this machine, the copper K_α transition is used to examine the sample.

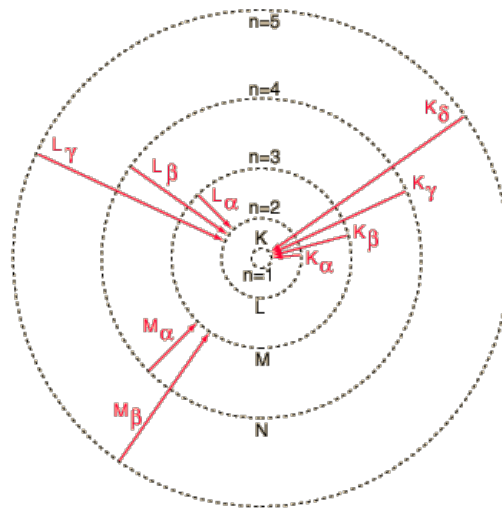


Figure 3.1: Schematic of the atomic transitions within the copper atom.

As shown in figure 3.1, the K_α transition is derived from an electron being excited to the $n=2$ shell and returning to the $n=1$ shell.

3.1.1 Theory

In a crystal, the atoms are arranged periodically in a lattice. When radiation strikes a material, it will be both scattered and absorbed. In most scattering directions, destructive interference occurs resulting in almost zero intensity. However, in a few directions, the scattered radiation wavefronts will be completely in phase resulting in constructive interference and a diffracted beam from the crystal.

When a diffracted beam is present, this will be along a direction such that Bragg's law is obeyed. Bragg's law considers each plane to be a scattering centre, rather than each atom individually. Strong diffraction occurs when the angle of incidence is equal to the angle of reflection. Bragg's law can be summarised by:

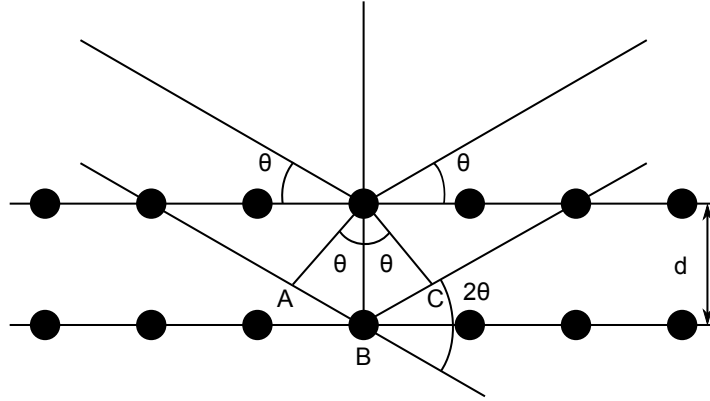


Figure 3.2: Schematic to show geometry of Bragg's law.

$$n\lambda = 2d_h k l \sin\theta \quad (3.1)$$

where n is an integer that represents the order of diffraction, λ is the wavelength, d is the crystals interplanar spacing and θ is the angle of incidence and the angle of diffraction relative to the reflecting plane. This is represented schematically in figure 3.2.

Bragg's law represents the conditions for diffraction from a set of parallel planes. The amount of radiation reflected when the Bragg condition is met depends on the structure factor ($F_h k l$) of the material. This is a mathematical representation of how the crystal scatters radiation. It essentially determines the scattering at any given angle by multiplying the scattering strength of:

1. an electron or nucleus
2. an atom
3. a unit cell

4. the total number of unit cells

all with regards to the direction of scattering and the relative phase of the scattered waves. These phases will then either add up or cancel out, thus explaining why some reflections are not seen.

The intensity in the diffracted beam from the planes (hkl) is proportional to the modulus squared of the structure factor:

$$I_{hkl} = |F_{hkl}|^2 \quad (3.2)$$

3.1.2 High Resolution XRD

High resolution X-ray diffractometry or (double-axis diffractometry) allows measurement of the rocking curve of the sample. The detector is fixed at the centre of the expected Bragg reflection while the sample is independently 'rocked'. This measurement is incredibly sensitive to strain and strain gradients within the sample. Thus it can provide a lot of information about the crystal structure of the material. It is also possible to model rocking curves for a given crystal structure to a high level of accuracy. This uses dynamical x-ray scattering theory to simulate a curve which is then refined and smoothed to compare with the real data taken.

The basic set-up is shown in Figure 3.3 and this is widely used for measurements of epilayer strain, composition, thickness and crystal structure.

In an ideal world, the incident radiation should be a perfectly parallel monochromatic beam. The reality, however, is that radiation will always have a small amount of spread in energy, direction, and divergence associated with it. This problem is usually solved by placing a beam conditioner between the x-ray source and the sample. This collimates and monochromates the beam

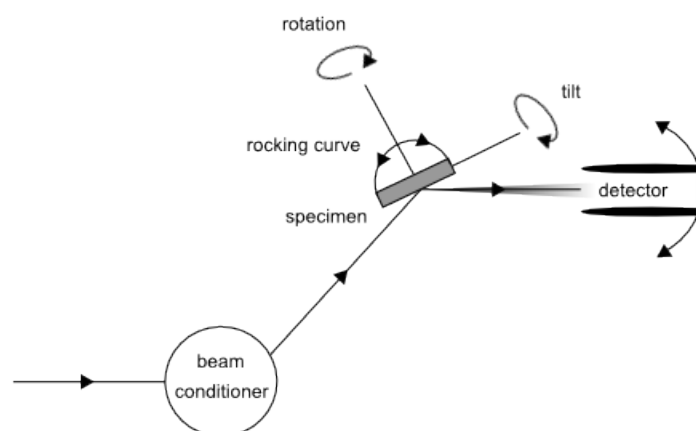


Figure 3.3: Schematic diagram of a high resolution double-axis X-ray diffractometer.

using a combination of diffraction and angular-limiting apertures. These apertures can also control the spatial width of the beam. The sample is then placed on a holder that can be tilted and rotated with a precision of around 1 arc second.

3.1.3 Triple Axis Diffractometry

Double-axis diffractometry is normally used because it is a relatively quick method of gaining crystallographic information. Unfortunately, it loses important data about mosaic spread or the extent to which the crystal is bent. Thickness fringes or narrow peaks are often blurred or even completely lost. Triple axis diffractometry places an analyser crystal between the sample and the detector and restricts the angular acceptance. This separates the effects of strain and tilt and allows a 2D Reciprocal Space Map (RSM) to be produced.

During the measurement of an RSM, both the specimen and the analyser

are rotated, and the scattering measured to produce a map. The map enables the diffraction from different sources to be distinguished, for example, scattering from the ‘perfect’ crystal occurs in a different direction in space to the scattering from defects. In addition, mismatch or strain can be distinguished from tilt or mosaic spread. RSMs have axes of Q_x and Q_y which are measured in reciprocal lattice units (rlu) and are proportional to $1/d$. Q_x and Q_y are related to ω and 2θ via the following equations:

$$Q_x = R[\cos\omega - \cos(2\theta/\omega)] \quad Q_y = R[\sin\omega + \sin(2\theta/\omega)] \quad (3.3)$$

where R is the radius of Ewald sphere.

3.1.4 PANalytic X’Pert Materials Research Diffractometer

The diffractometer used for the work discussed here is a PANalytical (Philips) X’Pert Materials Research Diffractometer (MRD). It is equipped with a copper tube X-ray source along with primary optics (beam conditioner) consisting of an X-ray mirror, 0.02 radian soller slits, in order to reduce divergence of the beam in the y -direction and finally a four bounce Ge(220) monochromator. This is used to create a parallel $K_{\alpha 1}$ beam of wavelength 0.154056 nm with an equatorial x divergence of $< 12''$.

The X’Pert system contains both a high resolution and a triple-axis detector, known as the upper and lower detectors respectively. The high resolution detector is an open detector with no slit whilst the triple-axis detector has a triple bounce Ge(220) analyser with a $12''$ acceptance. The high resolution detector can also be used with a slit placed in front of it to give a pseudo RSM. The system is capable of achieving the following resolutions: 0.01°

for ϕ (tilt - rotation about an axis lying in the plane of the sample) and ψ (twist - rotation about an axis perpendicular to the plane of the sample) and 0.0001° for ω (angle between the incident beam and the sample surface) and 2θ (angle between the incident and diffracted beam). In practice, these resolutions are limited by the step size used and the sample being measured. In reality, the highest resolution should be 0.0003° for ω and 2θ .

PANalytical X'Pert Epitaxy fitting software is also available to simulate rocking curves. A detailed explanation of the theory of fitting X-rays can be found in ref (25 jacs thesis).

3.2 Scanning Electron Microscopy (SEM)

The SEM system in Nottingham is a converted Jeol JSM-7000f SEM with an in-lens Schottky field emission source capable of acceleration voltages between 0.5 kV and 30 kV. This offers resolution of up to 3nm, maximum magnification of x500,000, and detectors for secondary, backscattered (composition, topography) and forward scattering electron imaging.

The SEM allows images of a sample to be taken by scanning the surface with a beam of high energy electrons. The electron beam is emitted thermionically from an electron gun fitted at the top of the column and is focussed by two sets of condenser lenses to a spot. The final condenser lens contains a set of scanning coils which deflects the beam in the x and y axes in order to raster scan the surface.

When the electron beam hits the surface, the electrons lose their energy as a result of repeated random scattering and absorption within the specimen. The incident electrons can either scatter elastically resulting in the reflection of high energy electrons (back scattered electrons); inelastically scatter,

causing emission of secondary electrons; or electromagnetic radiation can be emitted. Each of these can be collected and analysed with specialised detectors fitted to the SEM. Images discussed in this thesis are generally taken by studying the secondary electrons as these are more sensitive to topography. This is because the electrons only travel a short distance within the sample, so it is easy to gain an image from the number of secondary electrons detected.

3.3 Photoluminescence

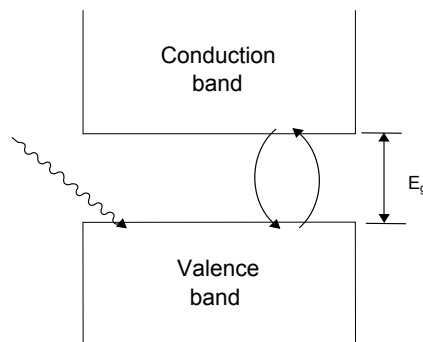


Figure 3.4: Schematic of photoluminescence.

Photoluminescence is a non-contact and non-destructive method of probing a material to reveal details about its electronic structure. When a semiconductor is illuminated by an external light source with an energy greater than the band gap energy, the light is absorbed in the semiconductor and electron-hole pairs are generated. These photo-induced electrons and holes recombine either radiatively or non-radiatively.

If light is shone upon the sample, it can absorb the photons and excite an electron in the valence band into the conduction band. The excited electron will then relax and fall back down to the original state, emitting a photon.

It takes only a few nanoseconds for an electron to be excited and then to re-emit a photon. This is known as radiative recombination. During non-radiative recombination, a phonon is released instead.

The energy of the emitted photon relates to the difference in energy levels between the state in the valence band and the conduction band. The intensity of the emitted photons also tells us about the contribution towards radiative and non-radiative processes from the initial incident photon.

In this report, photoluminescence measurements are used to reveal the bandgap of the sample. They can however be used to analyse the defect density within the sample and thus to a degree it can be a measure of material quality.

Measurements within this thesis was carried out using excitation from a Nd-Yag laser operating at 266 nm.

3.4 Optical Reflectance for Thickness Measurements

The optical reflectance apparatus consists of a white light source which is directed on to a sample, the reflected light is captured by a solid state spectrometer and analysed. The reflected data from the sample is normalised using reflected data from a mirror to produce a reflectance or absorption spectrum as shown in figure 3.5. Changes within the reflectance spectrum allow the material's bandgap to be estimated and, using the period of the Fabry-Pérot oscillations, the materials thickness to be determined.

Samples which consist of layers of different materials and therefore differing refractive indices normally exhibit Fabry-Pérot oscillations. Incident light waves reflect from each interface which can lead to beams that have

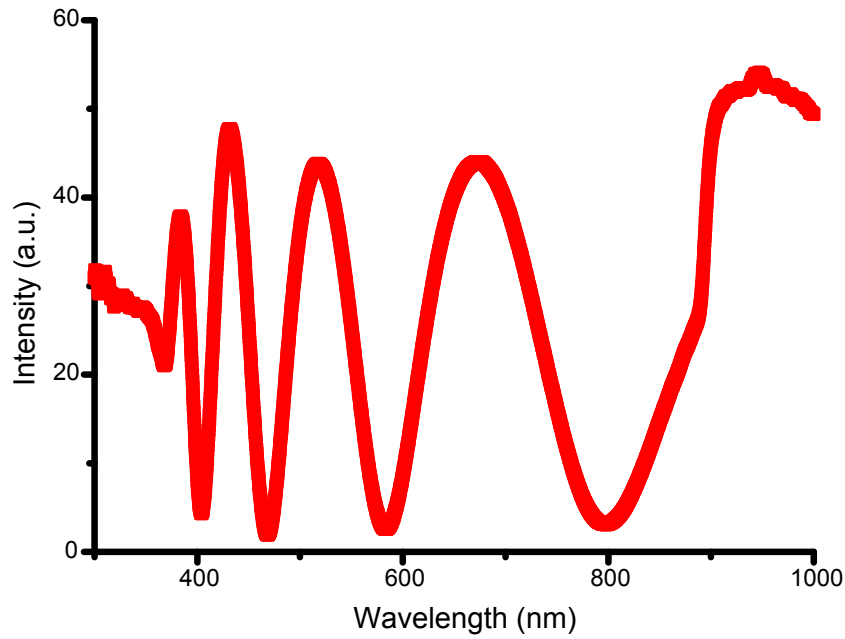


Figure 3.5: Optical reflectance spectrum from a 450nm layer grown on a substrate of GaAs.

undergone multiple reflections. This allows constructive and destructive interference to occur. If the transmitted beams are out of phase then destructive interference will occur. Constructive interference conditions are satisfied when $2n(\lambda)d = m + 0.5\lambda$ whilst the minima occurs when $2n(\lambda)d = m\lambda$ where $n(\lambda)$ is the refractive index of the first layer, d is the thickness of the layer, m is an integer and λ is the wavelength of the light.

3.5 Transmission Electron Microscopy (TEM)

Transmission electron microscopy operates using the same principles as a light microscope but utilises electrons rather than light. Electrons have a much shorter wavelength than light, which yields a resolution approximately a thousand times better than light.

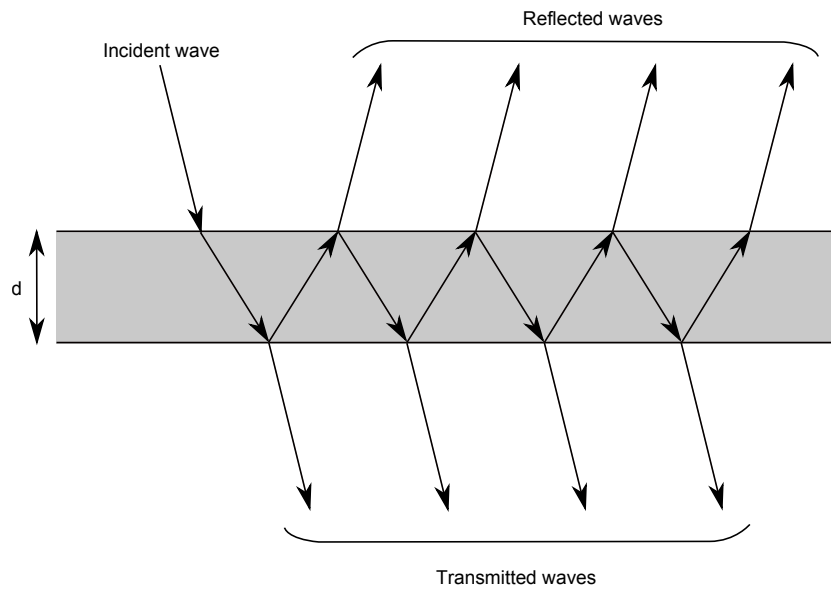


Figure 3.6: Schematic diagram of multiple Fabry-Pérot oscillations in a thin film of thickness d .

In TEM, an electron beam, generated by an electron gun, illuminates the specimen via a system of lenses. The electrons interact with the sample and are scattered. This scattered radiation is collected and focussed to form the image. Electrons interact strongly with matter, so the samples are thinned to a thickness of the order of tens of nanometres for high resolution TEM measurements. Ion beam milling is used to achieve this. A lot of effort goes in to the sample preparation ready for TEM analysis. Electrons need to be able to pass through the specimen that will be imaged, thus it needs to be thin (10-200 nm). The specimen also needs to be of a uniform thickness.

The TEM consists of a large column under vacuum. The electron gun is placed at the top and points downwards. The beam is then emitted down the column where it is focussed by a number of electromagnetic lenses and apertures.

Images formed by TEM can show features such as threading dislocations,

interface changes, domains of different crystal polytypes and surface morphology.

TEM samples in this thesis were prepared by firstly creating a thin wedge by ion thinning at an angle of 7° and -7° . Further ion thinning is carried out at 3 kV (rather than typically 10 or 20 kV) to reduce the ion damage to the sample.

All TEM analysis carried out in this thesis was undertaken at the University of Bristol.

3.5.1 Convergent Beam Electron Diffraction (CBED)

In contrast to conventional electron diffraction techniques where a parallel beam of incident radiation is used, CBED uses a convergent beam of electrons in order to limit the area of the specimen that contributes to the diffraction pattern. Each spot shows variations in intensity. These patterns can be used to interpret information about the thickness of the specimen, changes in lattice parameter due to composition or strain, and symmetry of the crystal. The convergent beam of electrons creates a Fresnel (near field) diffraction pattern which can be simulated to then obtain the polarity of the growth of the crystal being examined.

Simulations are carried out using JEMS diffraction software where the crystal information can be input along with the imaging conditions used for the TEM. This produces a simulated image of what the user should see which can then be compared with the CBED pattern and thus the polarity of the layer or nanorod determined.

CBED was carried out at the University of Bristol.

3.6 Seebeck effect

Samples that have been doped during growth were tested using the Seebeck effect. The positive probe of a multimeter was heated whilst the negative probe remained at room temperature. The probes were then pressed on to the surface of the sample. If the layer is p-type, then holes should move away from the positive hot probe and a negative voltage produced on the meter. If the layer is n-type then the opposite should occur. Holes should move away from the negative probe towards the hot positive probe and a positive voltage should be seen on the meter.

3.7 Conclusions

The characterisation techniques used for the semiconductor samples have been described in this chapter. The theory of x-ray diffraction has been outlined along with the specific diffractometer setup used for the samples in this thesis. SEM and TEM techniques have also been presented here as well as the CBED simulation procedure used to identify the polarity of the semiconductor material. OARS and the Seebeck effect have been introduced as the routine immediate checks carried out once samples have been unloaded from the system. Finally the theory of PL has been outlined.

Chapter 4

Growth of Indium Nitride Nanocolumns

4.1 Motivation

Indium Gallium Nitride has become a well researched material over the years because of its versatility. It has been utilised for Light Emitting Diodes (LED's) [2], laser diodes [116] and photovoltaic cells [117]. Over recent years, harvesting the sun's energy has become an increasingly intriguing prospect and research has grown worldwide in solar cell development. InGaN alloys have a direct band gap from 0.7 to 3.4 eV, which covers the visible spectrum and in principle presents us with the ability to be able to 'tune' the bandgap. Bulk InGaN contains a high density of defects due to the lack of lattice matched substrates. This can lead to non-radiative recombination centres so reducing the defect density would be desirable.

Nanorods promise a possible improvement in the quality of the InGaN material as they tend to grow defect free. Therefore, over recent years there has been increasing interest in InGaN nanorod research for LEDs and solar

energy conversion [118] [119] [120].

A substrate needs to be chosen carefully in order to reduce the lattice mismatch, and thus the potential strain induced within the layer. GaN, InN and InGaN have been successfully grown on different substrates including Si and Sapphire by Plasma-Assisted Molecular Beam Epitaxy (PA-MBE), and Metal Organic Chemical Vapour Deposition (MOCVD). It is already well established that GaN and InN nanorods can be grown by PA-MBE under strongly N-rich growth conditions [118] [119] [120].

A popular choice has been to grow GaN nanorods by PA-MBE on sapphire (0001) [118] [119] [120]. Nanorods grown in this way were found to be mostly free of threading dislocations. It has also been shown that by changing from N-rich to Ga-rich MBE conditions, the growth direction can be changed from vertical to lateral. This leads to growth of a continuous GaN overlayer [121]. Growing on top of the nanorods reduces the number of threading dislocations present in the layer. The coalesced GaN over-layers have been studied and possess an average threading dislocation density of up to two orders of magnitude lower than in continuous GaN epilayers [121].

InN nanorods have been achieved successfully using MBE and MOCVD on Si substrates by several research groups. However, it is evident that the band alignment is not suitable for the formation of p-n junctions between InN and Si [122] [123]. The conduction band minimum of InN is below the valence band maximum for Si. This makes this material combination unsuitable for any potential device application because of the potential for recombination. This problem of the band alignment can be overcome by growing InN on SiC substrates [124] as there is no overlap between the valence and conduction bands of the materials, so this material combination is the subject of the study described in this chapter.

4.2 Theory of Nanorod Growth by PA-MBE

Let us consider the growth of gallium nitride nanorods as this is the simplest nitride to produce nanorods using PA-MBE. In practice, growth of GaN nanorods needs very nitrogen-rich growth conditions which is believed to reduce the diffusion length for gallium [125] and carried out at approximately 700°C, typically on sapphire or silicon substrates. In all cases, there has been no evidence of liquid droplets present [118] on the surface which suggests that the growth mechanism for GaN by PA-MBE may differ from the vapor-liquid-solid (VLS) growth of other III-V semiconductors [126].

The vls model will be briefly discussed in section 4.2.1 and a new complementary geometric growth model [127] in section 4.2.2.

4.2.1 Vapor-Liquid-Solid mechanism of Crystal Growth

The vapor-liquid-solid method is thought to be the growth model that produces one-dimensional structures such as nanocolumns whilst using other growth methods such as Chemical Vapour Deposition (CVD) [128] or Chemical Beam Epitaxy (CBE) [129]. It was also thought to be the model for growth by MBE until recently [127].

The VLS model was proposed in 1964 by Wagner and Ellis in order to explain the anisotropic growth of Si wires that were catalysed by gold nanoparticles. A schematic of the VLS mechanism is shown in Figure 4.1 and was adapted from [130]. The silicon precursor species are supplied in the vapour phase, then at growth temperature, the pre-deposited gold particles on the surface form a liquid eutectic alloy with the silicon. Silicon is continuously supplied until the Au-Si alloy particle becomes supersaturated with silicon, which allows precipitation of the silicon at the interface between the sub-

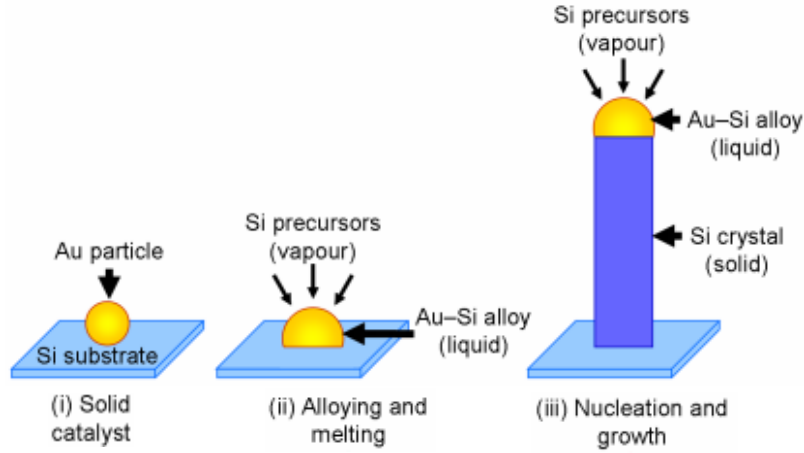


Figure 4.1: Schematic of the VLS growth of Si nanocolumns using a gold catalyst. (i) The initial stage of growth with a gold particle on the surface, (ii) Silicon vapour causes alloying and melting of the particle, and (iii) Nucleation via a silicon precipitate and growth.

strate and the particle alloy resulting in a solid crystalline silicon wire or column. Two possible explanations for nanocolumn growth were proposed by Wagner and Ellis; either the liquid particles are favourable collection sites for vapour phase reaction species and so nanocolumn growth propagates, or the metallic particle is a chemical catalyst which enhances the decomposition of the gas-phase precursors by lowering the activation energy barriers [131]. The VLS growth mode was then used for III-V nanowire growth utilising gold nanoparticles as a catalyst [132].

This vls growth model has been used for GaAs nanowire growth via MBE with and without the use of a catalyst [133, 134] respectively. However, a geometric growth model is thought to be more significant in the development of III-V nitride nanowires as explained in the next section.

4.2.2 Complementary Geometric Growth Model for GaN

Let us consider a horizontal PA-MBE system such as the Veeco gen-II or gen-III systems where the substrate is mounted vertically, the gallium cell is mounted in an upward pointing port and the nitrogen plasma source in a downward pointing port. This means that the gallium and nitrogen fluxes come from different directions in the system. In these systems, the cell ports are angled at approximately 30° to 40° to the normal of the substrate and samples are continuously rotated throughout the growth. This would suggest that atoms from both sources arrive on the top of the columns simultaneously but the arrival of the atoms at the sidewalls is different. As the sample rotates, the sidewall will be exposed to gallium for some of the time, then as it continues to rotate, the same part of the sidewall will be exposed to nitrogen which is similar to Migration-Enhanced Epitaxy (MEE) that was developed for low temperature growth [135, 136]. Given the geometry, it would be reasonable to assume that the arrival rate for the molecules at the top of the nanocolumn will be larger than the rate for the sidewalls, which would result in a difference in growth rate if we ignore any diffusion effects.

Let us consider the growth geometry of a cylindrical nanowire of length L , and diameter D , as shown in Figure 4.2, and is rotated continuously throughout sample growth. The arrival rate for Ga at the top of the nanocolumn can be expressed as $J\cos(\alpha)$ where J is the flux of the incoming gallium, and α is the angle between the surface normal and the flux. The vertical growth rate will therefore be equal to $J\cos(\alpha)/\rho$ where ρ is the density of gallium atoms in gallium nitride which is approximately $4 \times 10^{22} \text{cm}^{-3}$.

The growth rate on the side of the column however will be different. The gallium arrival rate is now given by $J\sin(\alpha) \times L \times D$, but this is spread over the column as it rotates, so over an area of $\pi \times L \times D$. Thus, the

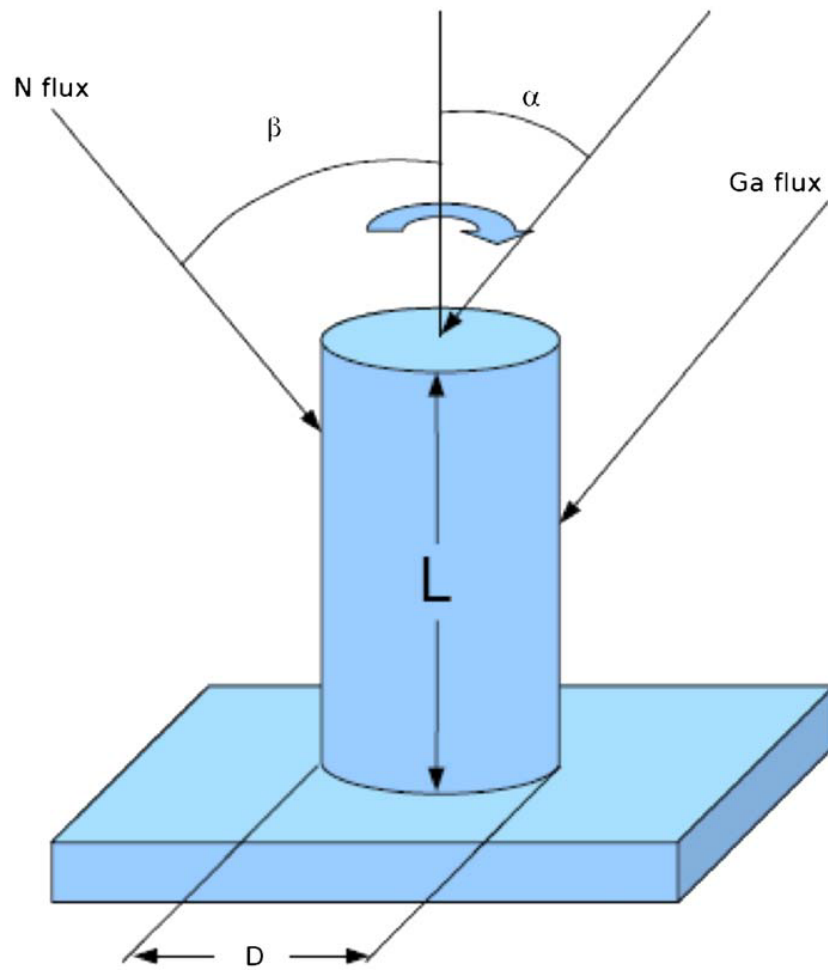


Figure 4.2: Schematic of the suggested growth model for a cylindrical nanocolumn in a PA-MBE system [127].

growth in diameter of the nanocolumn is given by $J \sin(\alpha)/(\rho \times \pi)$, which is a significantly lower rate.

The ratio of the vertical growth rate to the lateral growth rate is given by $\pi/\tan(\alpha)$ where α is 30° to 40° in the MBE machine considered, and will be approximately 5-6. This means that the growth rate of the nanocolumn is fixed by the geometry of the MBE machine being used. Once the nanocolumn has been formed and the rotation continues, the vertical growth rate of the nanocolumn will always be greater than the lateral growth rate, but both will increase linearly with time. Rotation is critical in order to form and maintain nanocolumn growth.

4.3 Experimental Method

All of the samples discussed in this chapter were grown in the ‘mini’-MBE system using the CARS25 RF plasma source and K-cells detailed in previous chapters. The In and N fluxes are measured using the ion gauge and growth was monitored with RHEED throughout. The nitrogen flux was kept constant at a growth chamber pressure of $\sim 4.0 \times 10^{-5}$ Torr, using a N_2 flow rate of 1.00 sccm. An applied RF power of 400W was used in all cases to ensure working in the high brightness mode of the plasma. InN decomposes at temperatures greater than 550°C [1] and the pyrometer does not operate below 550°C where growth was attempted. The BandiT cannot be used because the substrate is a wide bandgap material and the BandiT spectrometer attached to the system is only appropriate for GaAs. All growth temperatures presented in this chapter are substrate thermocouple readings. The InN films were grown on $10 \times 10 \text{ mm}^2$ 6H-SiC substrates from CREE.

Preparation for each growth begins with the same method to ensure the

same initiation conditions for each sample are created. Substrates were transferred to the growth chamber and heated to $\sim 700^\circ\text{C}$ for 20 minutes. This allows outgassing to occur and removes any residual surface contamination. Substrates were then cooled to the desired growth temperature (generally 400°C). Once the growth temperature had stabilised, the nitrogen flux was introduced into the chamber and the nitrogen plasma initiated. The MBE growth was started as soon as the plasma source was set to 400 W by simultaneously opening the In and N shutters. Strongly N-rich conditions (V:III ratio of $\sim 10 : 1$) were employed in order to enable the nanorods to grow. The growth time was typically 5 hours in each case.

After growth, samples were analysed *ex situ* using Scanning Electron Microscopy (SEM), Transmission Electron Microscopy (TEM), Convergent Beam Electron Diffraction (CBED) and Photoluminescence (PL). The InN nanorods on the surface and their densities were studied by SEM using a JEOL JSM 6330F, with a 12 kV operating voltage. TEM was used to examine the structure of the InN nanorods and InN layers using a Phillips EM430 with an accelerating voltage of 200 kV. CBED was utilised in order to look at the polarity of the nanorods by comparing the experimental image with a simulated image. Optical properties of the InN nanorods and layers were studied using PL at room temperature and at 4 K.

4.4 Results

4.4.1 Growth of Nanorods

There has been no previous published work carried out on the growth of InN nanorods on 6H-SiC substrates and so optimal growth conditions needed to be established. A fixed In:N ratio was chosen to give N-rich MBE conditions

that were known to give nanorods on other substrates. An In flux of 2.0×10^{-7} Torr was used, giving a V:III ratio of $\sim 10 : 1$.

First, the growth of InN was investigated as a function of growth temperature in the range 350 to 450°C. Figure 4.3 a) is an image of the surface of the InN layer grown at 350°C and shows that there are practically no nanorods present. Figure 4.3 b) shows the surface when grown at 400°C. At this temperature, a high density of nanorods can be seen on the surface. Increasing the growth temperature further to 450°C as shown in 4.3 c), leads to a reduction in the number of nanorods present on the surface. The latter two images show that there is an under layer that grows directly on the surface of the substrate and the taller nanorods emerge from this. This could be because of a difference in the growth rate between the flat surface and the rods resulting in a shorter under layer with tall nanorods growing through this. This difference in growth rate could be attributed to the layers growing with different polarities depending on the nucleation at the substrate surface. This is similar to the behaviour of GaN [137].

Figure 4.3 clearly shows that it is possible to grow nanorods on this substrate. The optimum temperature where the highest density of rods was achieved is at 400°C.

Once the best temperature for growth was found, the In flux was varied to determine the density of nanorods changes as a function of III:V ratio. Each 6H-SiC substrate has 2 faces - Si-face and C-face so growths were carried out on both to investigate if one face yields a more regular and uniform coverage of nanorods. Figure 4.4 shows the termination of both faces of the SiC substrate. SiC is a wurtzite structure, therefore the Si-face substrate has one dangling bond from each Si pointing out of the surface and the other three are bonded to carbon within the substrate. The C-face has one carbon

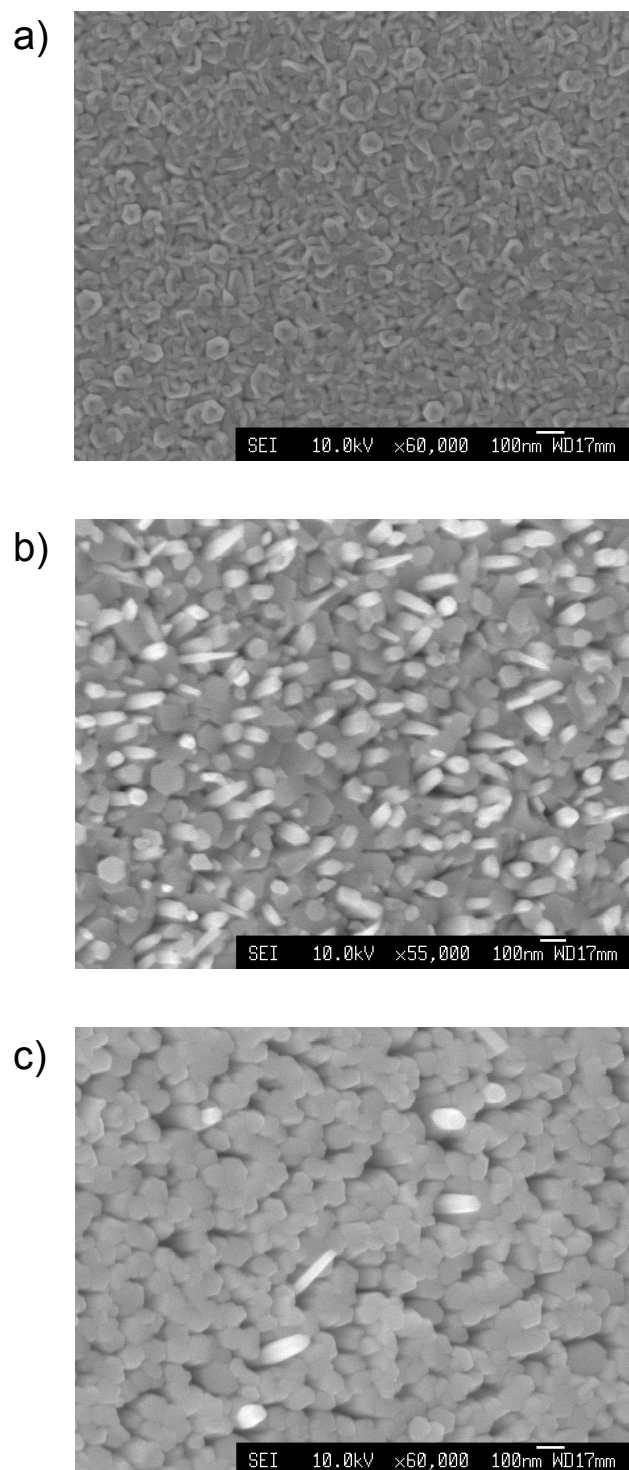


Figure 4.3: SEM images taken at $\times 60,000$ InN layers grown with In BEP of 2.0×10^{-7} Torr at a) 350°C , b) 400°C and c) 450°C .

bond pointing out of the surface whilst the remaining three are bonded to silicon within the substrate.

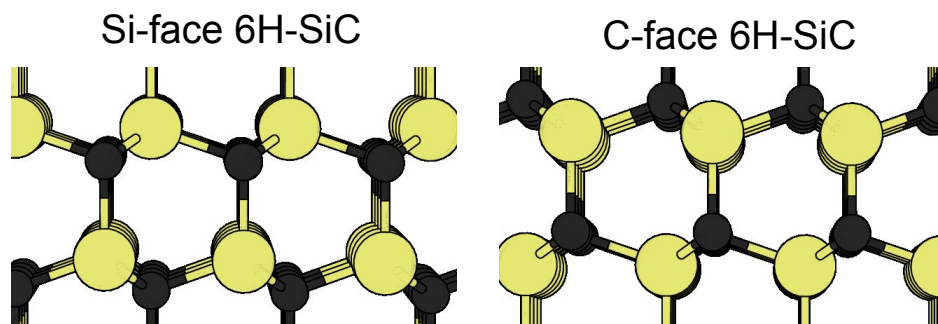


Figure 4.4: Schematic drawing of the dangling bonds left when the SiC substrate is terminated on the Si- or C-face. Yellow atoms represent Si while the black atoms represent carbon.

The In:N ratio was varied from an In BEP of 1.0×10^{-7} Torr to 3.0×10^{-7} Torr whilst keeping the growth temperature at 400°C and the N flux constant. Figure 4.5 shows a series of SEM and RHEED images from samples grown on Si-terminated SiC substrate. At low In:N ratios (figure 4.5a), the under layer is made up of discrete wide nanorods with taller and thinner InN nanorods protruding. At the higher In:N ratios (Figure 4.5c), there is more coalescence of the InN under layer making the islands much larger. There also appear to be fewer tall nanorods protruding. Figure 4.5b has the best coverage of nanorods. The most favourable growth conditions for InN nanorods on Si-face SiC are at an In flux BEP of 2.0×10^{-7} Torr and a growth temperature of $\sim 400^\circ\text{C}$.

The RHEED images taken for this set all show very polycrystalline material. It is unclear whether this signal is from the base layer, the nanorods, or both. The polycrystalline pattern is not present before growth is initiated, so it is a result of material being added to the surface. As the nitrogen flux is increased to 3.0×10^{-7} Torr, the complete arcs in the RHEED pattern

which are indicative of polycrystalline growth are replaced by defined spots. This change in pattern could be attributed to the crystal alignment being better with the higher flux, or the grain size could be bigger as the flux has increased. Polycrystalline RHEED patterns can be an indication that the rods are rotationally misaligned. Unfortunately, in this case, RHEED provides no information on the change in nanorod morphology. However the pattern develops from the diffuse scatter and faint streaks of SiC into the polycrystalline pattern. This indicates that growth has occurred on the surface.

As SiC substrates have two faces (Si-terminated and C-terminated), growth over the same flux range was also carried out on C-terminated SiC. Study of this set shows that at low In:N ratios (figure 4.6a), the under layer is made up of discrete wide nanorods with protruding thinner taller nanorods. At higher In:N ratios (figure 4.6c), there is improved coalescence of the under layer which makes the islands much larger. There are also fewer tall nanorods protruding. Figure 4.6b has the best coverage of nanorods and so we can conclude that the substrate orientation does not affect the choice of optimum growth parameters. Comparing the SEM images of the layer on both faces, fewer tall nanorods grow on C-face samples as the flux is increased compared with the Si-face samples.

RHEED does not reveal very much detail with regards to the surface during growth. One consistent observation between samples on the two surfaces is that the RHEED pattern becomes better defined as the nitrogen flux is increased to 3.0×10^{-7} Torr. RHEED also confirms that we are growing a layer on the surface as the evolution of the pattern can be seen from SiC to the polycrystalline rings.

There are obvious similarities between the two sample sets; as the nitrogen

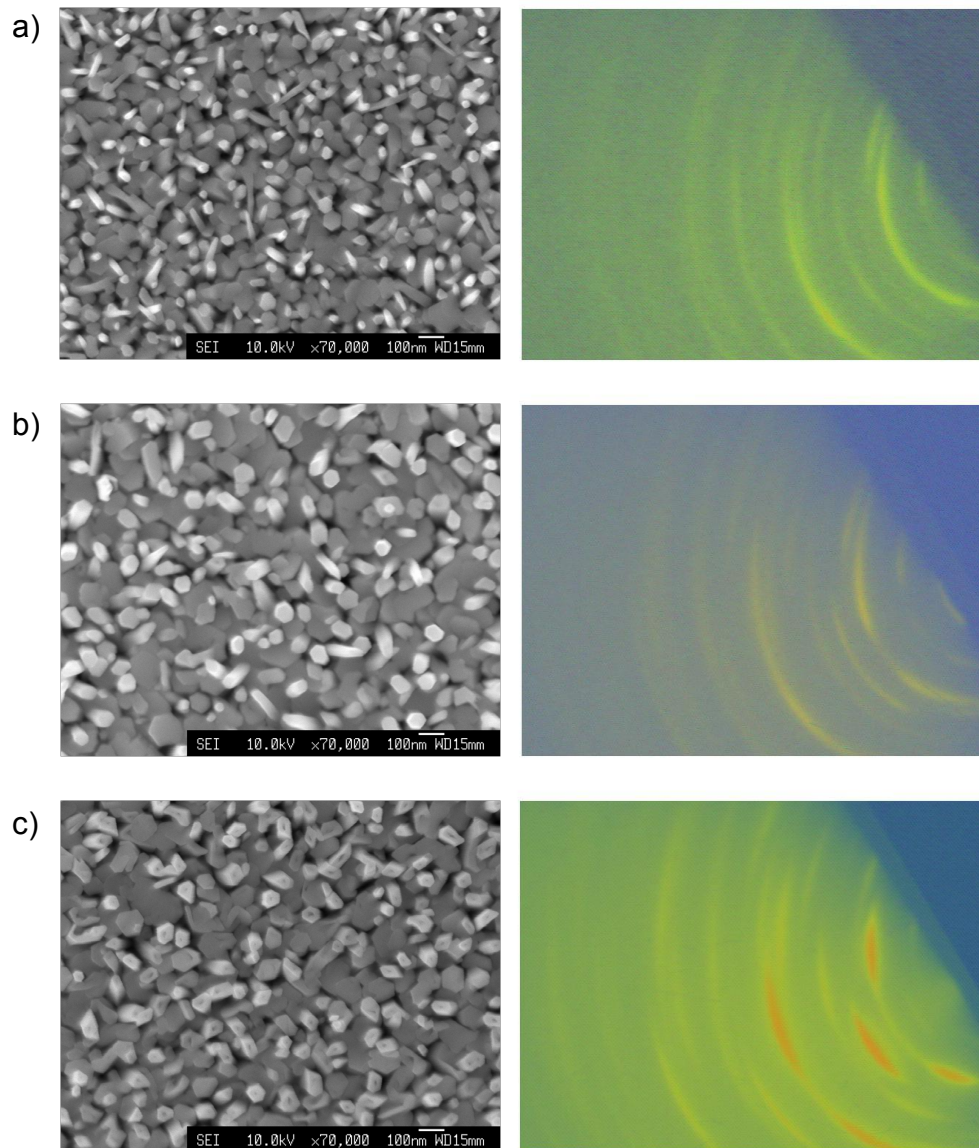


Figure 4.5: SEM (left) and RHEED (right) images of the InN nanorods grown on Si-face SiC at 400°C across an In flux range of BEP a) 1.0×10^{-7} Torr, b) 2.0×10^{-7} Torr, and c) 3.0×10^{-7} Torr.

flux is increased to 3.0×10^{-7} Torr, the total density of nanorods decreases and coalescence of the under-layer increases. Also, in all cases we observe two sets of rods, tall thin nanorods growing out of shorter wider nanorods (the under layer). One difference is that the density of taller nanorods present in the samples grown at 3.0×10^{-7} Torr appears to be a function of the crystal orientation. There are fewer tall nanorods present on the C-face sample compared with Si-face. Whether this is related to the polarity of growth is still under investigation.

4.4.2 Coalescence of Nanorods

In order to produce real devices, the rods need to coalesce in order to make contacting possible. This study began by establishing the In flux required for the growth of a continuous InN layer on SiC. An In flux of BEP $\sim 2.0 \times 10^{-6}$ Torr ($\sim 10 : 1$ V:III ratio) at $\sim 400^\circ\text{C}$ yields a continuous InN layer without any In droplets forming on the surface. This information was then used to coalesce an InN nanorod layer. First, the nanorods were grown with an In BEP of 2.0×10^{-7} Torr for 3 hours. The In flux was then increased to $\sim 2.0 \times 10^{-6}$ Torr for 2 hours to change the growth mode from N-rich to metal-rich conditions. It was hoped that this would achieve a coalesced top layer. Figure 4.7 is an SEM image of a successfully coalesced nanorod layer. The image shows the surface of the complete InN layer and confirms that coalescence of the rods can be achieved.

TEM and CBED analysis were performed on the coalesced InN layers grown on SiC. TEM (figure 4.8a) allows the structure of the rods to be analysed whilst CBED (figure 4.8b) reveals the polarity when compared with simulation from the JEMS software discussed in section 3.5.1.

It was found that InN layers grown on the Si-face of SiC substrates have

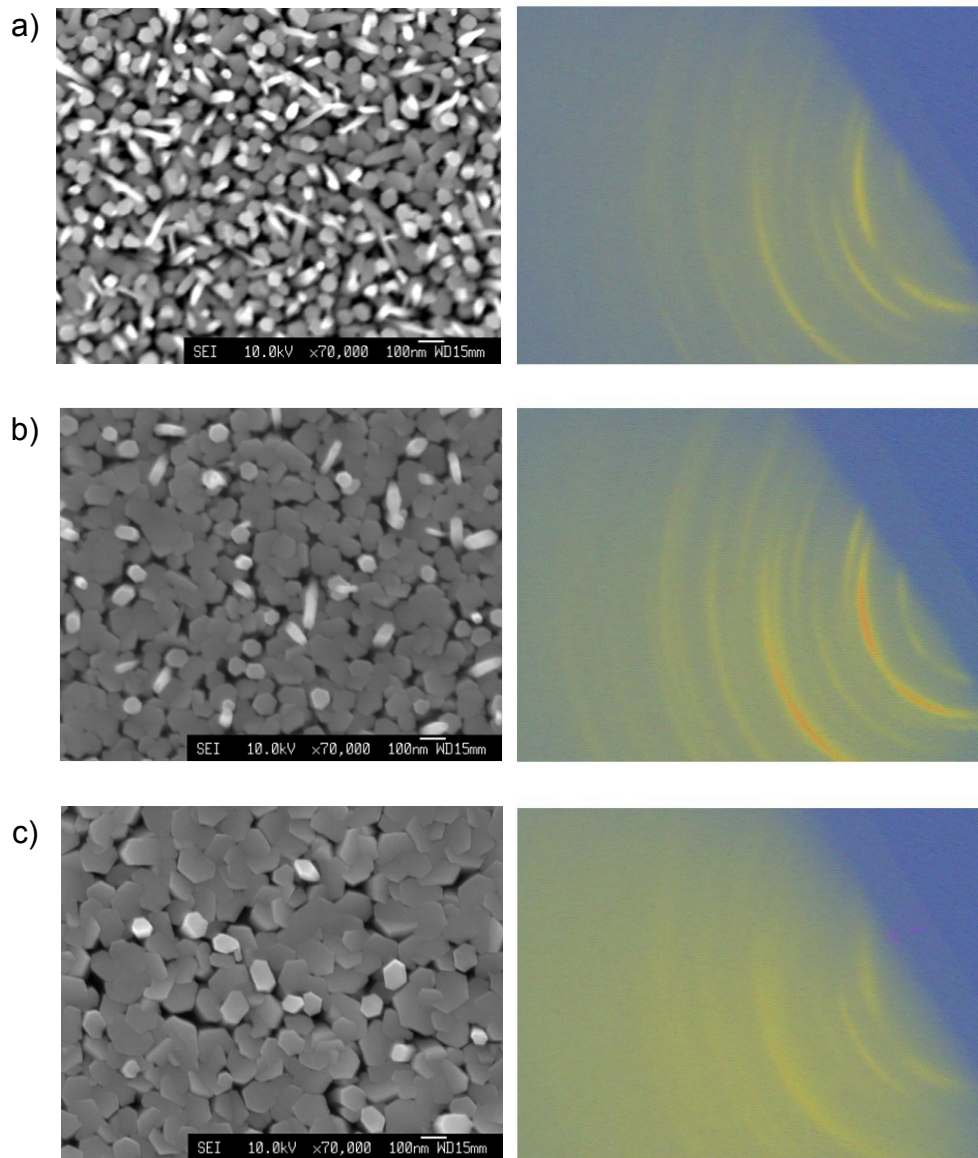


Figure 4.6: SEM and RHEED images taken during the growth of InN nanorods on C-face SiC at 400°C across an In flux range of BEP a) 1.0×10^{-7} Torr, b) 2.0×10^{-7} Torr, and c) 3.0×10^{-7} Torr.

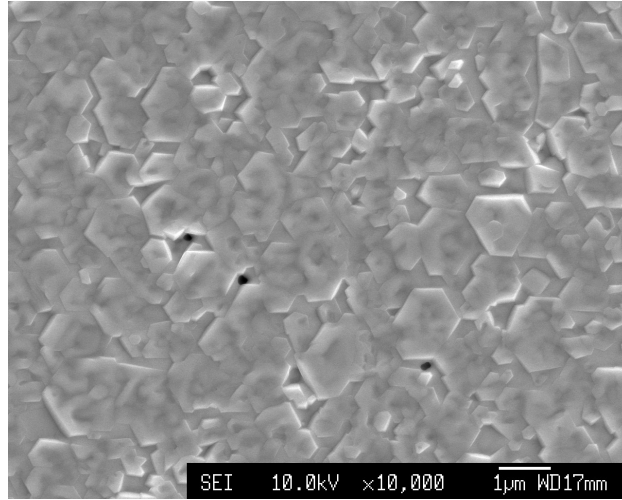


Figure 4.7: SEM image of coalesced InN layer grown on top of the InN nanorods.

In-polarity, as shown in Figure 4.8. The polarity of the InN nanorods and layers grown on the the C-face is still under investigation at the University of Bristol.

Growth of the nanorods is initiated from small nucleation sites on the surface of the substrate. The rods then continue to grow vertically, with a small degree of lateral growth. They then coalesce in the final stage of epitaxy. The bimodal growth can also be seen in the TEM image shown in figure 4.8b). The shorter nanorods tend to be wider and make up the under-layer whilst the tall ones appear to have a hollow core. This is a well studied defect that occurs whilst growing GaN [138, 139]. The hollow core is indicative of a screw dislocation being present. This means that the growth occurs in a spiral motion around a central hollow column. This growth mode is the principal relaxation method within GaN. The screw dislocation can be caused by a misfit within the lattice on the surface at nucleation. This can occur when there is a misalignment equivalent to half of the repeating unit that forces the rod to grow spirally.

CBED analysis was carried out (figure 4.8b) in order to analyse the polarity of the nanorods. The tall and thin nanorods were harvested from a sample grown on Si-face SiC by rubbing the sample with a mesh that breaks them off the substrate. These nanorods were then tested and found to grow In-polar. This is similar to previous work carried out to investigate GaN nanorods grown on sapphire [137]. In that study the taller rods grew Ga-polar and the shorter wider rods grew N-polar. It would be reasonable to think that InN would react in a similar manner.

Now that the polarity of the samples are known, it is worth discussing the differences between growth on Si- and C-terminated substrates. From the SEM images, (figures 4.5 and 4.6) growths on C-terminated have less tall In-polar rods on the surface as the flux is increased. It is not known why there is a difference in the number of nanorods but is something to be investigated.

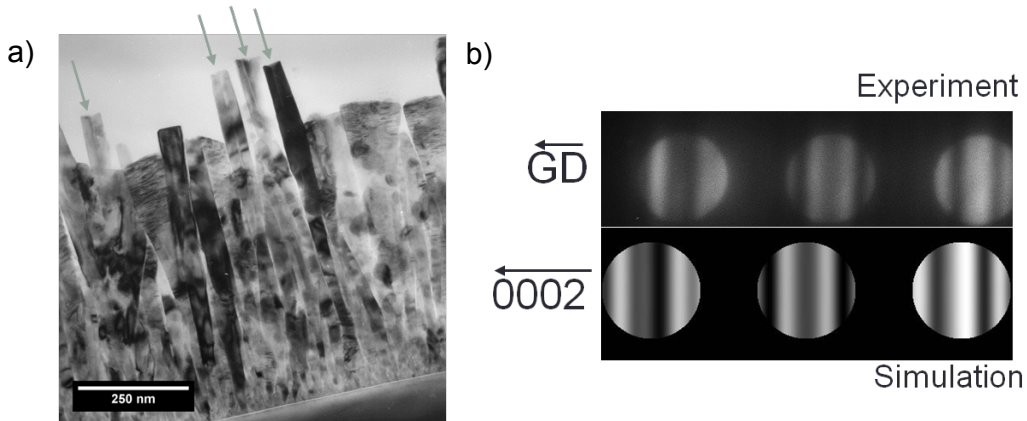


Figure 4.8: Data from nanorods grown on Si-polar 6H-SiC a) TEM image of nanorods, and b) CBED data for InN sample CBED simulations for In-polar InN.

Figure 4.9 shows the low temperature ($\sim 4\text{K}$) luminescence spectrum obtained from a nanorod sample that had been successfully coalesced (LG177). A peak is observed at $\sim 0.7\text{eV}$. This is a slightly higher energy than the best

reported PL data for InN nanorods [140, 1]. However, this could perhaps be attributed to several things, either a higher density of defects within the coalesced layer compared with a pure nanorod sample, or the Moss-Burstein effect [141]. This effect causes the apparent bandgap to be higher than the band gap as the absorption edge is increased in energy because states close to the conduction band edge are populated.

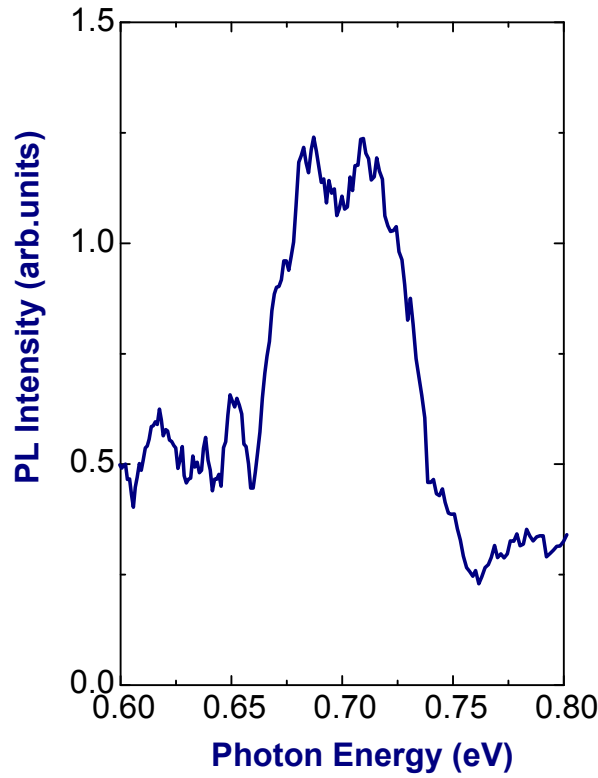


Figure 4.9: Low temperature ($\sim 4K$) PL spectrum from an InN coalesced layer on Si-face 6H-SiC.

The Moss-Burnstein effect is seen when the electron carrier concentration exceeds the conduction band edge density of states, and this corresponds to degenerate doping in semiconductors. Nominally doped semiconductors sees the Fermi level existing in between the conduction band and valence band.

As the doping concentration is increased, electrons then begin to populate states within the conduction band which increases the Fermi level energy and can push it in to the conduction band. An electron from the valence band can now only be excited into the conduction band above the Fermi level as all states below the Fermi level are occupied and Pauli's exclusion principle forbids excitation in to occupied states. This explains the apparent increase in the bandgap.

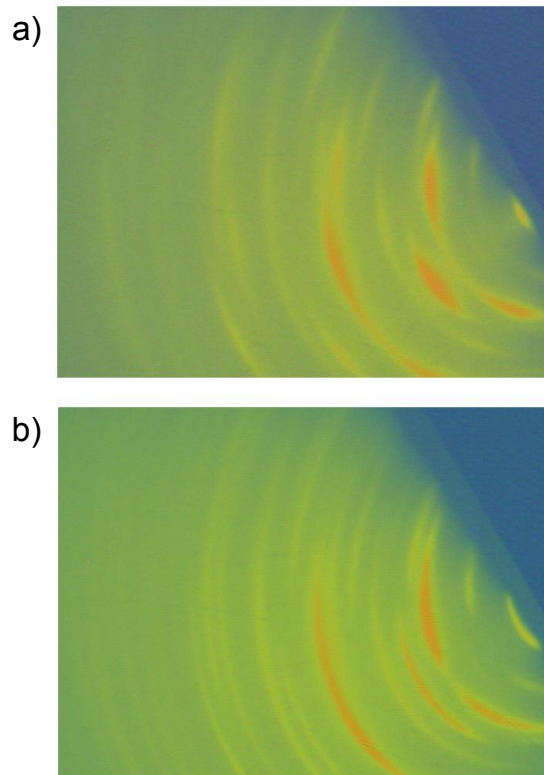


Figure 4.10: RHEED images taken during the growth of InN nanorods on p-type SiC on a) Si-face (LG169), and b) C-face (LG170) with a growth flux of 1.0×10^{-7} Torr.

Two p-n junction heterostructures were grown on both of the available

faces of SiC. These were fabricated using p-type SiC substrates. The InN layer is intrinsically n-type [142] so there is no need to add dopants to create the heterostructure. RHEED patterns were taken during the growth of these samples and are shown in Figure 4.10. As with the previous samples, RHEED does not reveal much information about the surface structure. It would be reasonable to suggest that these samples have fewer crystalline phases when compared with the previous RHEED images as this set has more defined spots. Possibly this equates to better ordered nanorods.

Table 4.4.2 is a list of all of the InN samples that have been grown along with the conditions used.

Sample	Temperature (°C)	Flux ($\times 10^{-7}$ Torr)	SiC Substrate (face, type)	Growth time (hours)	Layer type
LG155	300	2.1	unknown	5	rods
LG156	400	2.0	unknown	5	rods
LG157	450	2.0	unknown	5	rods
LG158	350	2.2	unknown	5	rods
LG159	400	2.0	unknown	5	rods
LG160	400	3.0	unknown	5	rods
LG161	400	2.1	unknown	5	rods
LG162	400	2.1	Si-face, n+	5	rods
LG163	400	3.0	Si-face, n+	5	rods
LG164	400	1.0	Si-face, n+	5	rods
LG165	400	2.0	Si-face, n+	5	rods
LG166	400	1.0	C-face, n+	5	rods
LG167	400	3.0	C-face, n+	5	rods
LG168	400	2.0	C-face, n+	5	rods
LG169	400	1.3	Si-face, p+	5	rods
LG170	400	1.0	C-face, p+	5	rods
LG171	400	10.0	C-face, n+	3	continuous
LG172	400	19.0	C-face, n+	3	continuous
LG173	400	9.8	C-face, n+	3	continuous
LG174	400	19.0	Si-face, n+	5	continuous
LG175	400	1.0	C-face, p+	3	rods
LG176	550	18.9	Si-face, n+	5	continuous
LG177	400, 550	18.5, 1.0	Si-face, n+	3, 2	rods, coalesce
LG178	400, 550	18.5, 1.1	Si-face, p+	3, 2	rods, coalesce

Table 4.1: Table of all InN growth carried out.

4.5 Conclusions

The growth of InN nanorods on 6H-SiC substrates has been investigated in this chapter. Nanorods were successfully grown on both the Si- and C-faces of the wafers, and the optimum PA-MBE growth conditions for InN nanorods were found to be a BEP flux of $\sim 2.0 \times 10^{-7}$ Torr and a growth temperature $\sim 400^\circ\text{C}$.

Coalescence of the nanorods was achieved by increasing the flux to $\sim 2.0 \times 10^{-6}$ Torr during the growth. CBED analysis has confirmed that the tall nanorods were growing In-polar, similar to the case of GaN nanorods. It seems likely that the thin under-layer will be growing N-polar as this is a slower growth mode. Photoluminescence data agrees with the literature and confirms that InN of a reasonable quality has been produced.

Chapter 5

Growth of GaN, InN, and InGaN

5.1 Motivation

Indium Gallium Nitride (InGaN) layers with low In content are now extensively used as the active region of light emitting diodes [2] and lasers operating in the blue/UV region of the spectrum. Other potential uses for this materials system include photovoltaic cells as the band gap range varies from 0.67 eV to 3.4 eV for indium nitride (InN) [1] and gallium nitride (GaN) [2] respectively. For this full range to be realised, InGaN with high In content needs to be grown. This has previously proved difficult in both Metal-Organic Vapour Phase Epitaxy (MOVPE) and Molecular Beam Epitaxy (MBE). In MOVPE, high In content InGaN is difficult to grow due to the high vapour pressure of nitrogen over the alloy at the growth temperatures needed, and the tendency for phase separation which increases with increasing In content [38]. In addition to the phase separation problem, there is evidence in Plasma-Assisted Molecular Beam Epitaxy (PA-MBE) for In segregation to

occur at the surface when growing under metal rich conditions. This effect is reduced under N-rich growth conditions. Another challenge whilst trying to grow this material is the lack of re-evaporation of any excess In from the surface. This is due to the evaporation temperature of In being higher than the thermal decomposition temperature of InGaN.

It has been demonstrated for PA-MBE that growth with a metal rich surface, although not one so metal rich to develop droplets, leads to optimum properties with respect to surface roughness and electrical measurements [143]. However for InGaN, this is unachievable due to the low growth temperature needed (approximately 550°C).

When growing any nitride-based material, the graph by Heying et al. [143] needs to be considered 5.1. There are three clear regimes in the diagram: metal-rich, nitrogen-rich, and an intermediate phase. Growth under N-rich conditions yields material that has a rough surface and can contain a high number of defects. Very nitrogen-rich growth yields columnar material [144] with less than ideal electrical and optical properties. However, if highly nitrogen-rich conditions are utilised, nanocolumns are produced which typically grow defect-free.

Metal-rich conditions produce much smoother layers with fewer defects. However, this growth regime can lead to metal droplets on the surface. The intermediate region allows growth to occur with some metal on the surface and any excess is evaporated by maintaining by utilising a higher growth temperature. All of the advantages of metal-rich growth are achieved without metal droplets being left on the surface.

GaN is generally grown at 650°C and above, Allowing growth in the advantageous intermediate regime. For high In content InGaN, the lower growth temperature (550°C and below) means growth is in the N-rich phase

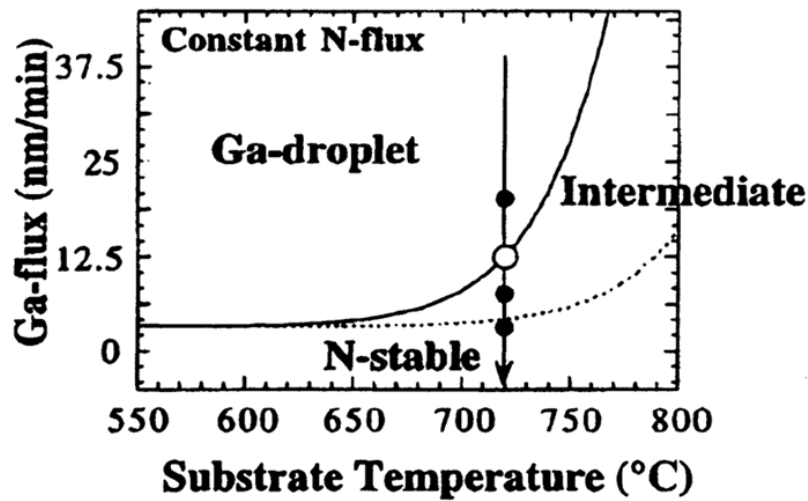


Figure 5.1: Graph illustrating the different growth regimes at different temperatures when growing gallium nitride [143].

of the diagram, which can lead to poor quality material. If possible, growth at these low temperatures would ideally be carried out using a stoichiometric III:V ratio. This is extremely challenging to maintain throughout an entire growth because of variations in the fluxes from the plasma source, the group III sources, and temperature gradients across the substrate wafer.

There are a selection of growth methods where one or more of the source fluxes are pulsed described in the literature [135, 145, 146], all of which have the aim of trying to keep metal on the surface, without it building up and forming droplets. This creates a pseudo-intermediate growth phase as metal is allowed to remain on the surface throughout most of the growth.

One possible method is Metal Modulation Epitaxy (MME) [135] as pioneered by Doolittle et al. at Georgia Tech. This method periodically closes the group III shutters to allow any excess metal on the surface to be consumed. The growth is monitored throughout using RHEED to study film

quality as the epitaxial layer develops. However, in this chapter a novel alternative method is proposed which is called Anion Modulation Epitaxy (AME).

5.2 Anion Modulation Epitaxy

Anion Modulation Epitaxy (AME) periodically interrupts the nitrogen flux to achieve similar aims as MME as discussed above. AME has one main advantage over MME in that it involves modulating only one beam within the growth system. It also ensures a metal rich surface for most of the growth time. RHEED monitoring throughout growth allows real-time feedback from the surface that can be used to adjust the AME cycle. This helps to ensure no build-up of excess metal on the surface during the growth. This will be discussed in detail later in this chapter.

Similar methods have previously been used for low temperature growth of As based III-Vs, known as Migration Enhanced Epitaxy (MEE) [145] and Nucleation Enhanced Epitaxy (NEE) [147] or Phase Locked Epitaxy (PLE) [148].

MEE alternately supplies metal and arsenic to the sample surface and is used in order to grow high quality material but at a lower substrate temperature than is normally used. MEE also encourages step-edge growth. NEE is used with the aim of encouraging the nucleation of islands. A controlled As pulse deposits an As monolayer on the surface, which is then turned into GaAs by the addition of the Ga beam, Ga droplets are stopped from forming by another pulse of As atoms to deposit. PLE utilises the oscillations visible in the RHEED pattern to allow easier growth of abrupt layers like a superlattice. Figure 5.2 shows the differences between these three techniques with

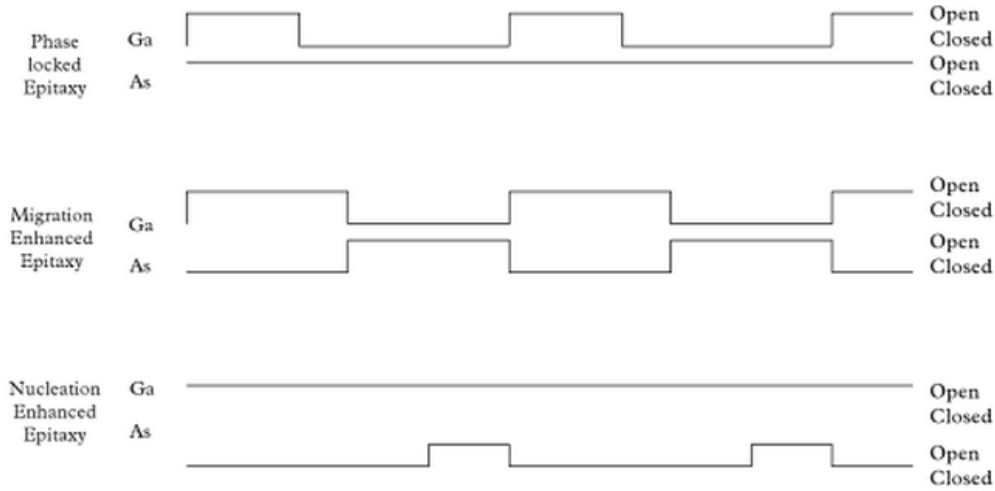


Figure 5.2: Summary of the shutter sequences used in the different types of modulated growth [149].

regard to the shutter sequences used.

In this chapter, AME is used to investigate the growth of GaN at lower temperatures than in conventional MBE.

5.3 Experimental Method

The samples used in this chapter were grown by PA-MBE and AME using the system constructed at the University of Nottingham as well as the Gen III system. During growth, films were monitored *in situ* using RHEED. As the temperature is an important parameter, the commercial BandiT system was also used [150]. For this reason, initial growths were carried out on GaAs (111)B substrates where accurate temperature measurements are possible using the BandiT, in preference to sapphire, SiC or GaN templates. However, the results presented should in fact be better with other substrates where the strains between the substrates and grown layers are minimised. The native

oxide was removed by heating to approximately 620°C whilst monitoring the surface using RHEED. The surface was then nitrated at 650°C and a GaN film grown under conventional PA-MBE growth conditions at 680°C to ensure a reproducible starting surface for each sample. Visual monitoring of the surface through grazing incidence windows allows the onset of gallium or indium droplets to be viewed for very low excess coverages. At this shallow angle, changes in the diffuse scattering of light can be observed for a build up of as little as two monolayers of excess group II on the growth surface. This was calculated by knowing the deposition rate of the group III metal, shutting the nitrogen shutter, and watching for a change on the substrate surface (cloudy/milky appearance). Re-opening the nitrogen shutter allows the metal on the surface to be used up and the surface can be seen to change from cloudy to shiny again. After growth, samples were examined *ex situ* using AFM and XRD. PL and optical reflectance data were also taken.

5.4 Results and Discussion

5.4.1 GaN Results by AME

The nitrogen shutter sequence for AME is shown schematically in Figure 5.3, which also shows the change in surface concentration of the group III element as a function of time. Group III material is allowed to build up on the surface whilst the nitrogen shutter is closed. Upon opening, the group III concentration decreases. The conditions were established for stoichiometric growth for GaN at high temperature and then, using a calibrated ion gauge, the equivalent beam pressure was calculated for In. The N-flux was adjusted to decrease the III:V ratio, resulting in a N-rich growth if carried out by PA-MBE, but a simulated stoichiometric growth using AME. This method is

therefore used to avoid droplet formation, but maintain a metal rich surface throughout a large portion of the growth cycle.

During the initial period of deposition, with the nitrogen shutter closed, only a small flux of active nitrogen reaches the substrate so the group III metal concentration on the surface increases until approximately 2 monolayers (MLs) is deposited. The nitrogen shutter is then opened and growth continues until all the excess metal is consumed. The nitrogen shutter is then closed and the cycle is repeated throughout the growth. This strategy enables growth to take place in a metal rich environment for the majority of the time. This growth method is known to smooth the surface and improve film properties. At the same time, this process avoids metal droplets from forming on the substrate surface by ensuring a short period of N-rich growth at the end of each cycle. RHEED and visual inspection of the sample surface through the window during growth also ensures this.

The growth is monitored by RHEED throughout whilst the sample is rotating (if in the Gen-III) or whilst stationary (in the ‘mini’-system). As shown in Figure 5.4 a clear sequence of patterns develop, which repeat for each AME cycle. At the beginning of the RHEED sequence, a streaky pattern is observed which is indicative of metal rich growth conditions. As the metal is consumed on the surface, the streaks shorten and change into a spotty pattern which is evidence that nitrogen rich growth is occurring. When all of the metal has been consumed, facets are immediately observed on the spots. This is particularly prevalent in Figure 5.4.

The relative times for metal-rich and N-rich growth can be adjusted precisely by determining the time in the cycle when these facets first occur. Any variation in fluxes can be easily compensated by adjusting the RF power to the plasma source. This is because it has previously been established to a

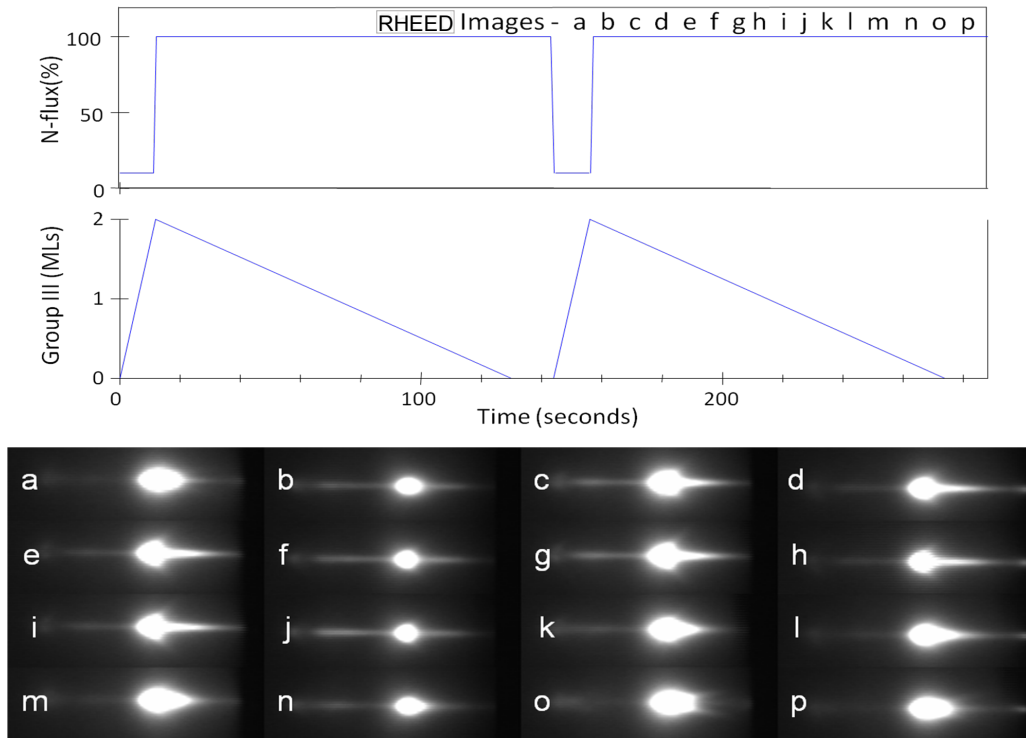


Figure 5.3: This shows the shutter sequence for the nitrogen flux together with the surface concentration of group III flux as a function of time. The growth sequence is as follows. During the time period when the nitrogen shutter is closed the group III surface concentration increases linearly with time; upon opening the nitrogen shutter the surface concentration decreases linearly with time, but growth takes place under metal-rich conditions until the free metal on the surface is "consumed". Finally, growth takes place for a very brief period under N-rich conditions. Letters a-p correspond in time to the RHEED images underneath the plot. Each column represents a different azimuth. A larger image of the RHEED spots is shown in Figure 5.4.

first approximation that the concentration of active nitrogen is proportional to the RF power for a fixed nitrogen flow rate [104]. If facets are no longer developing at the end of each cycle, a small amount of excess metal is left on the surface. Turning up the RF power should correct this. Alternatively, if facets develop early in the cycle, turning down the RF power will lengthen the time that the growth spends under metal-rich conditions.

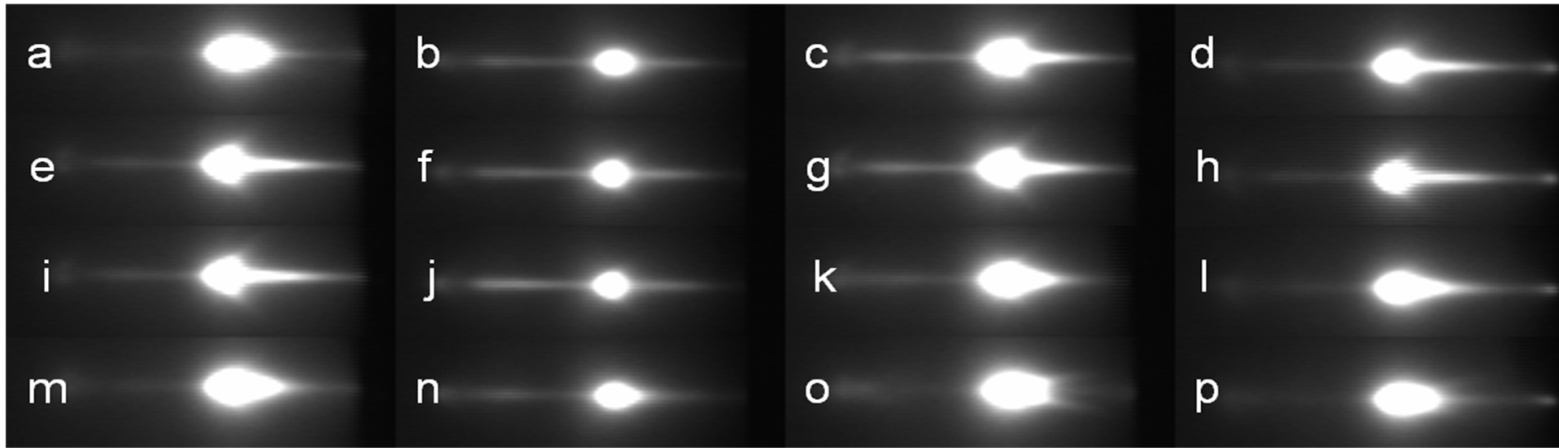


Figure 5.4: This is a series of RHEED images taken during the AME sequence on the Gen III, the images are taken with rotation and so various columns are for different azimuths. Letters a-p correspond in time to the RHEED image lettering in figure 5.3.

Having established that the growth conditions are stable, it is also possible to increase the mean concentration of metal on the surface. This is done by increasing for only one cycle the time during which the N plasma source is closed.

The aim of AME is that it will aid in the growth of InGaN samples. An ideal growth temperature for InGaN is in the range 500-550°C. At this point in the Heying diagram (Figure 5.1) there are only two growth regimes. Ideally, an entire growth run carried out under stoichiometric conditions would provide a sample with good film quality, but to do that for an entire growth is impossible. AME simulates growth within the intermediate regime which occurs only at higher temperatures. This should produce a film with all the positive attributes (low rms surface roughness, low defect concentration, improved electrical properties etc.) that are seen with samples of this kind.

Initial tests were carried out on GaN and then InN layers deposited at both 500 and 550°C. Films were grown by both PA-MBE and AME using identical growth conditions in order to determine any differences between the methods. For all of the samples in table 4.1, growth rates were determined from the Ga flux used, which remains constant with time. Therefore, for the same total time, the layer thicknesses should be equivalent. The times in brackets (t_1, t_2) indicate how long the nitrogen shutter is closed (t_1) and the period for which it is open (t_2). Three different t_2 times were tested; 30 seconds of applied nitrogen was predicted to consume all of the group III on the surface. Times above and below 30 seconds were picked in order to obtain a spread of results but also because there are fluctuations within the cell fluxes and plasma. Growth times for AME samples were adjusted to obtain the same layer thickness as the nitrogen shutter is closed for approximately 12.5% of the growth time. Hence, a growth duration of 2.25 hours for AME

compared with 2 hours for PA- MBE. Optical interference measurements after growth confirm that the films are of equal thickness of approximately $0.5 \mu\text{m}$ within experimental error from the thickness measurement.

For films grown using the AME technique we observe significantly improved properties compared with growth by PA-MBE at the same growth temperature. The surface morphology for GaN films grown by AME are greatly improved compared to the equivalent structures grown by PA-MBE. The rms roughness is decreased by an order of magnitude from 16nm for the PA-MBE GaN grown at 550°C to 1.5 nm for the equivalent AME sample. A similar improvement is seen for the samples grown at 500°C .

X-ray diffraction $2\theta/\omega$ line scans are shown in Figure 5.5 along with the photoluminescence data for the same samples in Figure 5.6. All of these samples are grown at 550°C and with the same gallium and active nitrogen fluxes. It can be seen from the X-ray data that the AME samples have narrower line widths when compared with the PA-MBE control layer. In addition, the intensity of the peak has decreased by almost a factor of 2 when using PA-MBE as compared with the highest AME sample. The FWHM measurements reveal that the layers are of similar quality with the exception of LG26 which is marginally worse. This suggests that the AME grown samples are of similar quality to PA-MBE samples at 550°C . However, photoluminescence was more prominent from the PA-MBE layer with a peak at approximately 700 counts.

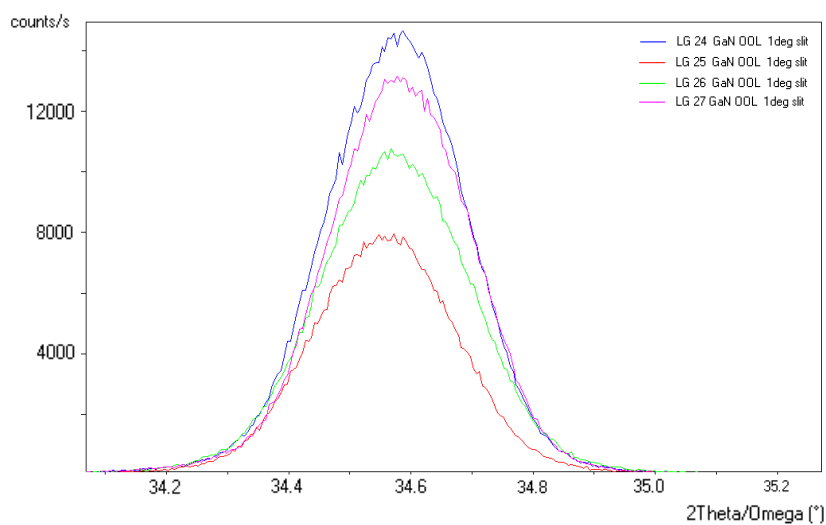


Figure 5.5: $2\theta/\omega$ line scans for GaN at 550°C

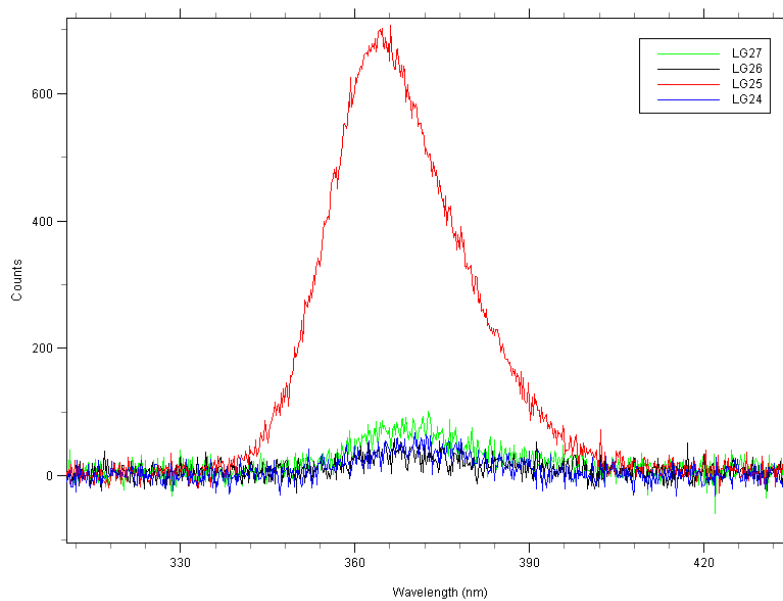


Figure 5.6: Photoluminescence from the 550°C GaN sample set. LG25 is the MBE grown sample that has given out a stronger photoluminescence when compared with the AME samples. The AME samples give off less than 100 counts compared with 700 counts for the MBE sample.

Sample	LG38	LG36	LG35	LG37
C/O times	(4,28)	(4,30)	(4,32)	PA-MBE
Temperature (°C)	500	500	500	500
FWHM (Omega) (deg)	1.1	1.5	1.6	1.8
Sample	LG24	LG26	LG27	LG25
C/O times	(4,28)	(4,30)	(4,32)	PA-MBE
Temperature (°C)	550	550	550	550
FWHM (Omega) (deg)	1.1	1.3	1.1	1.1

Table 5.1: Table of XRD data for the samples grown by AME compared to control samples grown by PA-MBE at both 500°C (LG35-38) and 550°C (LG24-27). The times in brackets (t_1 , t_2) are the times in seconds for which the nitrogen shutter was closed (t_1) and open (t_2). The Ga shutter is open continuously. Increasing t_2 , increases the time during which the growth is nitrogen rich. The MBE control sample is grown with the same Ga and N fluxes, within experimental error.

Figure 5.8 shows diffraction data from GaN grown at 500°C by both AME and PA-MBE. As with the samples at 550°C, the MBE grown sample (LG37) has the lowest intensity. Also, there has been a shift in the peaks between samples from around 34.5° for the same AME samples to 34.6° for the PA-MBE sample. With the 550°C sample set, the peaks have remained approximately the same at 34.6°. The layer grown by PA-MBE has a higher FWHM at 1.8° compared with AME samples, the lowest being 1.1° for LG38 grown by AME. As t_2 is increased the FWHM of the sample is increasing, suggesting that the film quality is decreasing. Thus, the best quality material is grown at $t_1, t_2 = (4, 28)$.

Figure 5.9 illustrates an photoluminescence observed from the samples. All samples produced by AME have shown PL in this set at 500°C, the highest producing 280 counts. PL for sample growth at 550°C has shown

the opposite trend. This is an indication that material quality increases as growth temperature decreases when using AME.

Figure 5.7 shows reciprocal space maps centred around the GaN peak for two separate samples both grown at 500°C, one by AME and the other by PA-MBE. The FWHM is much narrower in the omega direction for the AME sample when compared with the control using PA-MBE. This implies that there is a lower mosaic spread normal to the growth direction. For the films grown at higher temperature the differences are much smaller.

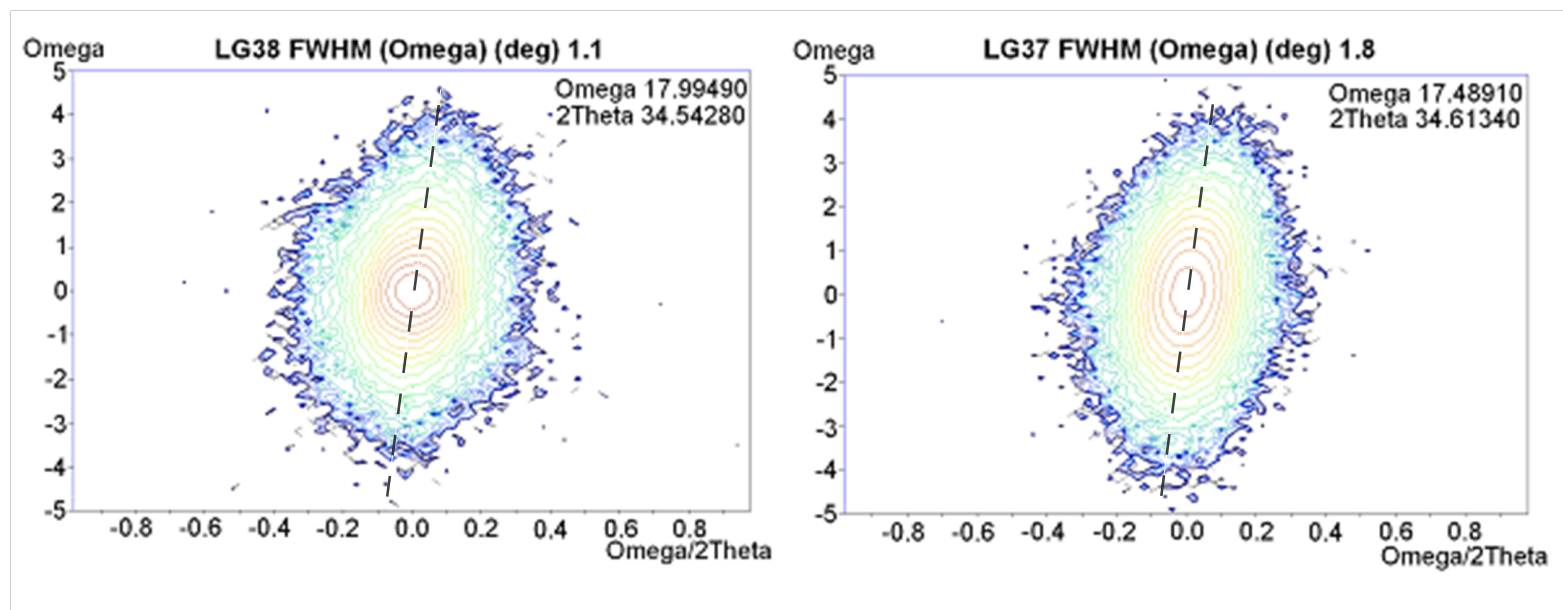


Figure 5.7: Reciprocal space maps for samples grown at 500°C by AME and PA-MBE, grown at the same temperature and with the same Ga and active nitrogen flux. The FWHM (Omega) is much narrower for the AME sample (LG38) compared to the equivalent control sample grown by MBE (LG37) indicating better structural properties.

Whilst producing GaN via both growth methods at 500°C and 550°C, opposite trends occur.

At 550°C, the layers have an improved quality when grown by traditional PA-MBE, whereas AME shows better quality layers when a substrate temperature of 500°C is used. Therefore, it can be concluded that as the substrate temperature decreases, AME produces improved layer quality. AME is simulating high temperature growth by having 1-2 MLs of gallium on the surface and the properties observed in the intermediate phase are also being exhibited here. High temperature growth is always carried out under slightly metal rich conditions so that the sample lies in the intermediate regime (Figure 5.1) as any excess will evaporate from the surface. This is encouraging for the eventual growth of InGaN as properties observed when growing at higher temperatures are being maintained at lower temperatures than normally expected.

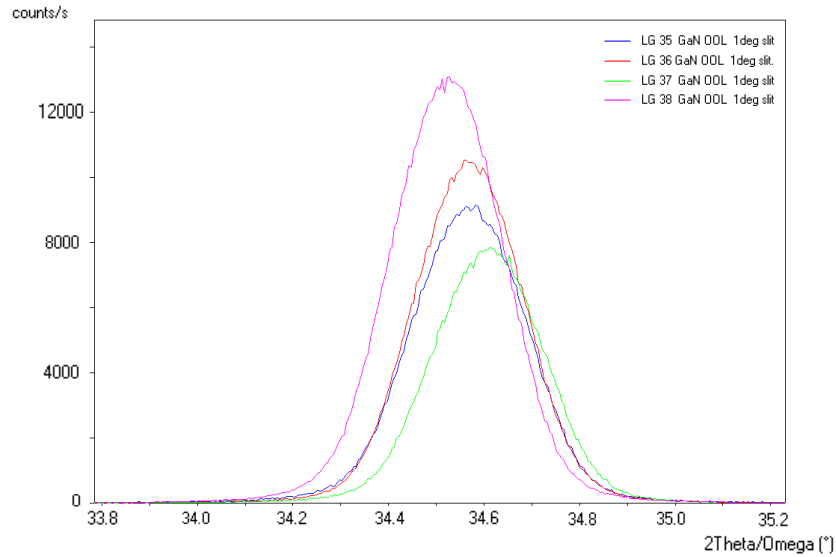


Figure 5.8: $2\theta/\omega$ scans for the GaN sample set at 500°C

The ability of AME to produce p-type doping of GaN using magnesium

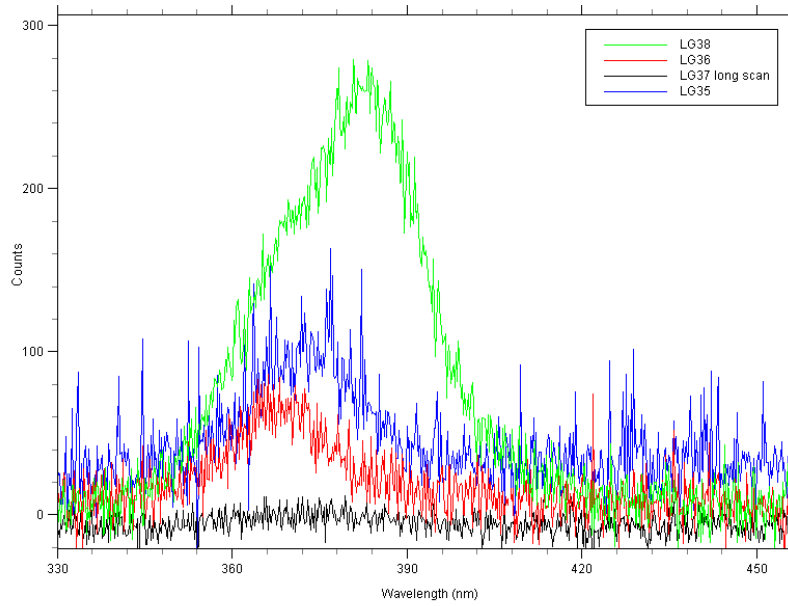


Figure 5.9: Photoluminescence data carried out on GaN grown at 500° C

at lower temperatures has also been tested. Samples were tested using the Seebeck effect as discussed in section 3.6. The positive probe was heated whilst the negative probe remained at room temperature, then pressed on to the surface of the sample. A negative voltage was produced on the multimeter indicating that the layer was p-type doped. Doping has been achieved [151] at temperatures as low as 550°C. Previous attempts at p-type doping of GaN have shown that it is only possible at high growth temperatures for thick films grown under carefully controlled V:III ratios [152]. By comparison, AME has made p-doping more reliable and reproducible.

5.4.2 InN Results by AME

InN was also grown at 500°C in a similar study to above to determine if there are any differences between the quality of the two layers grown by the growth

methods within this materials system. $2\theta/\omega$ scans were carried out on each sample. As can be seen from Figure 5.10, there is no clear trend for InN as to which method leads to improved properties. The lowest and highest intensity peaks are both from AME grown samples.

As a calibrated ion gauge was used, equivalent gallium fluxes are known. Using an equivalent gallium flux of 7×10^{-8} mbar, this would produce a layer under stoichiometric growth conditions and 8×10^{-8} mbar should be metal rich with droplets visible on the surface.

Figure 5.11 is a plot of sample thickness against equivalent gallium flux. For gallium nitride growth at 680°C , the thickness of the layer increases until the III:V ratio moves into the metal-rich regime, with the excess metal evaporating and the growth rate tending to a constant. Metal is not seen on the surface as any excess re-evaporates at this temperature. The same shape graph was expected for the growth of indium nitride, but instead the layer carried on increasing in thickness. Re-evaporation of metal on the surface is zero at 500°C so the metal must be existing within the growth layer, possibly between grain boundaries.

To test this theory, a high temperature gallium nitride buffer layer was grown before the indium nitride growth. The properties of such a layer are well determined and should give a reproducible starting surface for each sample.

Figure 5.12 shows two samples grown using the same fluxes for indium and nitrogen. The left hand wafer has a high temperature gallium nitride buffer layer and the right hand wafer does not. With the buffer layer, there is suddenly a large amount of metal on the surface that is not visible without the buffer layer. As re-evaporation of indium from the surface does not occur at these low growth temperatures, the excess metal in the right hand sample

must have been absorbed within the layer either between grain boundaries, or because the sample is columnar. This accounts for the growth rate continuing to increase into the indium rich regime and why there is no metal present on the surface.

A further observations that supports the idea that metal is trapped within the layer was made during the growth of PIN structures (detailed in chapter 6). When a layer of p-GaN was initiated on top of an InN layer, liquid metal was drawn to the surface that was not previously visible.

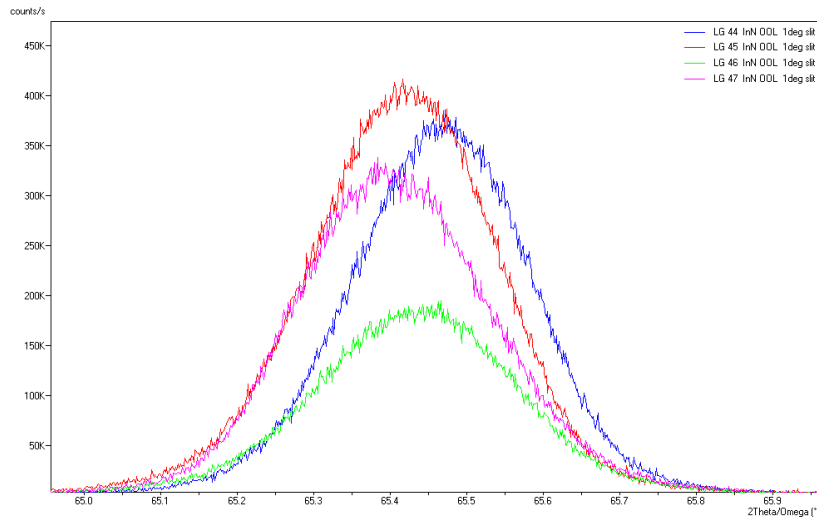


Figure 5.10: X-ray data for InN with a growth temperature of 500°C

5.5 Cyclic temperature changes during AME

As previously mentioned, growths on GaAs were monitored in situ using the BandiT system for samples grown by both PA-MBE and AME. During PA-MBE, once the shutters have been opened and the growth initiated, the recorded temperature stabilises and generally remains constant. However, when using AME as the growth method, the temperature changes during

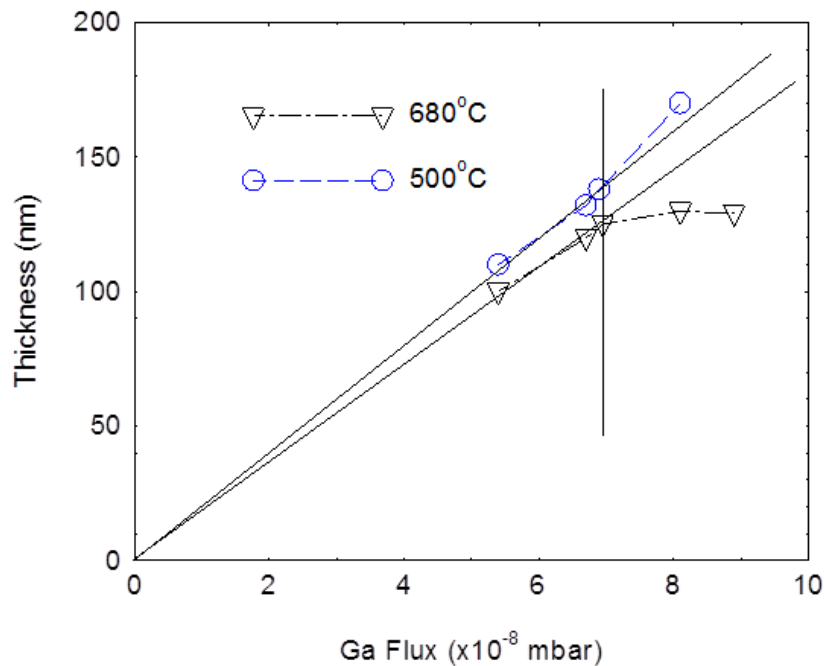


Figure 5.11: Growth rate data for gallium nitride at 680°C (in black) and indium nitride at 500°C (in blue). It is expected that the growth reaches a saturation point and the sample can not become any thicker as the amount of group V is remaining the same. In this case, the indium nitride layers seem to keep increasing in thickness.

each shutter cycle as shown in figure 5.13. When the nitrogen shutter is closed at the beginning of each cycle the temperature at the surface starts to increase until it is approximately 15°C hotter. This can be attributed to enhanced absorption of radiation from the heater because of the presence of metal on the surface [153]. If more metal were deposited at the start of each cycle, then the increase in temperature would be significantly greater. Once the nitrogen shutter is opened, and excess metal starts to be consumed, the temperature slowly decreases to its original starting value. The amount of nitrogen rich growth at the end of each cycle can also be determined by



Figure 5.12: Images of samples resulting from different growth conditions. The left hand wafer is with a buffer layer whilst the right hand uses the same indium and nitrogen fluxes but with no buffer layer present.

examining the BandiT temperature profile as a function of time. As can be seen in Figure 5.13, for longer periods of Nitrogen rich growth, at the end of each cycle, the gradient of the line tends towards zero.

There is also a delicate balance to be maintained throughout; the correct amount of metal has to be deposited so that it can be consumed within the cycle, whilst being sufficient to maintain metal rich growth for the majority of the cycle. If the metal is not being used up within each cycle, then there will be an overall increase in temperature. Thus, the base temperature (measured at the minimum) of the substrate during each cycle will slowly creep up. Similarly, if the amount of nitrogen-rich growth at the end of each cycle increases, the overall base temperature will slowly decrease. It is possible to strike a balance between the two growth regimes by optimising the nitrogen plasma power and the power being supplied to the substrate by the heater. This results in the same maximum and minimum temperatures as demonstrated in the latter part of the graph of Figure 5.14.

Figure 5.15 shows a BandiT spectrum taken throughout an entire growth. This demonstrates how dramatically the temperature can fall if there is a

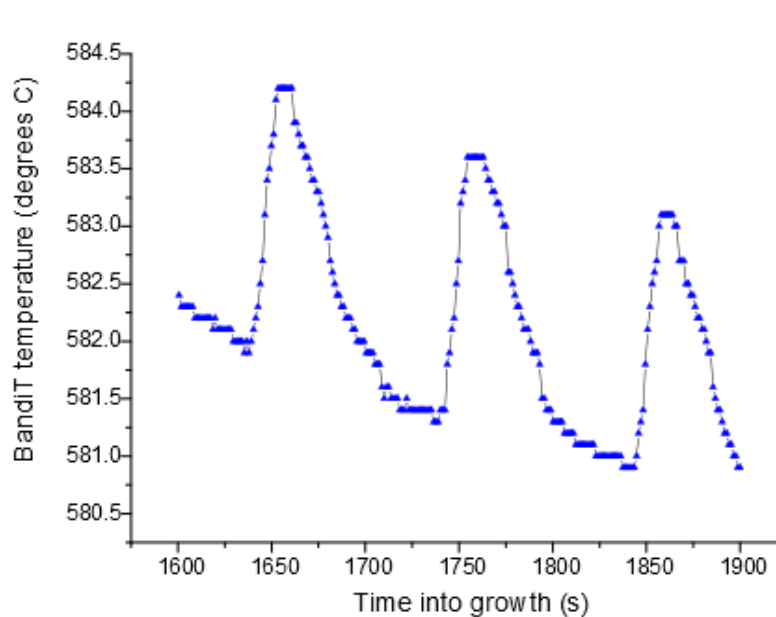


Figure 5.13: This shows the cyclic temperature changes in more detail for each sequence, whilst growing using the AME technique. The increase in temperature is rather fast whereas the decrease is slower.

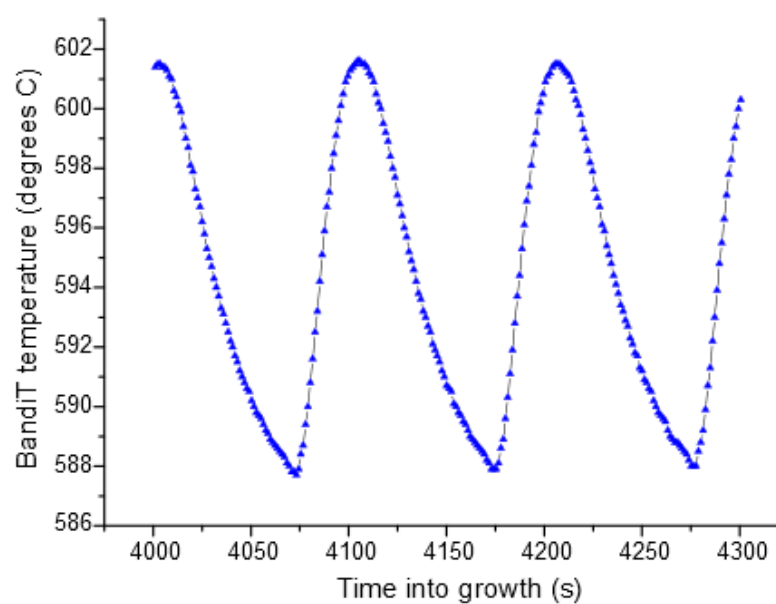


Figure 5.14: This is a close up from figure 5.15 that shows how reproducible the cyclic temperature changes become once the conditions have been optimised.

large amount of nitrogen-rich growth at the end of each cycle. It also shows how stable the growth temperature can become once small adjustments have been made.

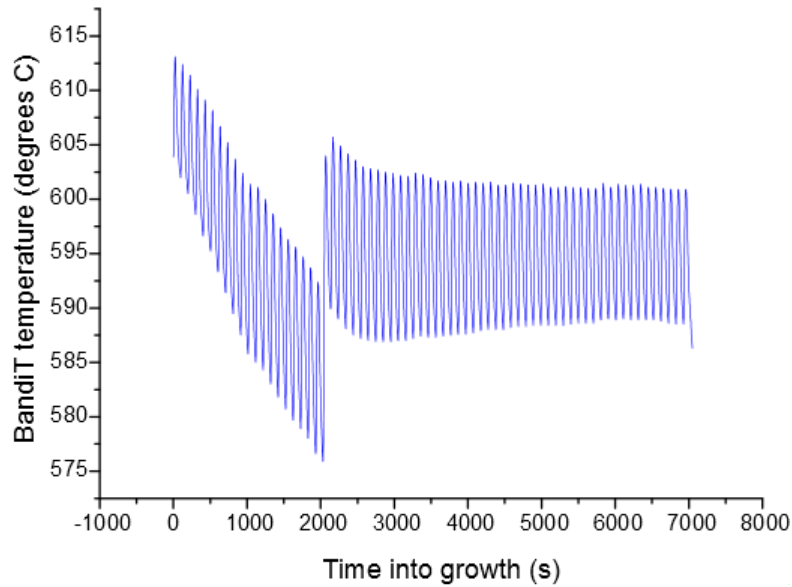


Figure 5.15: This graph shows the change in temperature throughout an entire growth. It can be seen that the growth can be stabilised so that only the cyclic temperature change occurs with no temperature trend for the extrema.

It is reasonable to suggest that other pulsed methods show a larger change in the temperature during each cycle. This is due to the change in heat load at the substrate while shuttering a metal flux. A metal cell is likely to produce much greater changes at the substrate surface than from interrupting the nitrogen from the plasma source. Thus similar effects or even larger are to be expected during growth by MME [146].

5.6 Conclusions

A new method for the growth of group III-Nitrides has been developed from Plasma-Assisted Molecular Beam Epitaxy (PA-MBE) known as Anion Modulation Epitaxy (AME). This technique gives rise to improved growth compared to equivalent samples grown by conventional PA-MBE methods. During AME, the nitrogen flux is interrupted periodically to build up a group III surface concentration of approximately two monolayers, which is then reduced to zero at the end of each growth cycle. This leads to enhanced mobility and significantly improved morphology compared to growth using conventional PA-MBE. It also enables doping at lower temperatures compared to PA-MBE. Direct comparison of GaN samples grown at equivalent temperatures by PA-MBE and AME show improved structural, electrical and optical properties for the samples grown using AME.

AME has allowed investigation in to the origin of temperature changes at the substrate surface when using any pulsed growth technique. The substrate temperature was found to vary by up to 15°C each time the flow was interrupted, producing a cyclic effect. It seems reasonable to infer that this would be the minimum temperature change experienced by other pulsed methods, such as metal modulated epitaxy (MME), where one or more metal fluxes is modulated periodically to achieve the same overall objective. In addition, slower long-term trends are observed depending on the average nitrogen to metal ratio. Increased metal-rich growth leads to an increase in overall temperature, whereas increased nitrogen-rich growth leads to the opposite effect.

Chapter 6

Application of AME for Solar Cells

6.1 Motivation

Efficiently harnessing the sun's energy has been a tantalising prospect for years as it is a 'free' resource waiting to be used. It is thought that the next generation of photovoltaics will be based on InGaN devices specifically because the band gap covers the entire visible light range from 0.64eV for InN [1] to 3.4eV for GaN [2]. Being able to utilise the whole spectral range in a single materials system would mean significant cost savings in production.

Conventional single-bandgap solar cells have been investigated for many years and the best of them are now achieving their maximum theoretical efficiencies. This efficiency is predicted by the Shockley-Queisser limit [154]. This limit refers to the maximum theoretical efficiency of a solar cell under concentrated sunlight, as a function of semiconductor bandgap and is $\sim 30\%$. If the bandgap is too high, most daylight photons cannot be absorbed; if too low, most photons have much more energy than necessary to excite electrons

across the bandgap, and the rest is wasted. These semiconductor solar cells have been constructed using a p-n junction, and is $\sim 30\%$.

The Shockley-Queisser limit has been exceeded experimentally by combining materials with different bandgaps to make tandem solar cells. Single-gap cells waste a considerable amount of incident energy due to a large amount of photons not being absorbed as they don't possess either enough energy to cross the bandgap or too much energy that is then converted into wasted heat.

There are three approaches that could be used to harness the energy that is otherwise lost [155]:

1. Increase the number of energy levels available by using tandem (multijunction) cells.
2. Multiple carrier pair generation per high energy photon, or single carrier pair generation with multiple low energy photons. In other words, relying on high energy photons to form multiple carriers close to the bandgap energy.
3. Capturing carriers before thermalisation as in hot carrier cells.

Of all of these solar cells, only the tandem cell has produced efficiencies that exceed the predicted Shockley-Queisser limit. More information is available in reference [155].

Unfortunately, there is a considerable mismatch in lattice parameter between InN and GaN. This would make conventional multijunction solar cells difficult to produce without introducing high defect densities which in turn reduces the efficiency.

An alternative approach would be to use the Intermediate Band Solar Cell (IBSC) approach pioneered by Luque and Martí [117] in 1997 where one or

more energy levels are added in the bandgap creating an intermediate band. The addition of these extra levels means that lower energy photons with energies less than the band gap can be absorbed in addition to photons with enough energy to make it cross the bandgap ($h\nu > E_g$). Two photons with energies less than the bandgap can be absorbed to promote an electron and create an electron-hole pair. The intermediate band concept is illustrated in Figure 6.1 for different absorption pathways. Photon (3) has enough energy to excite an electron from the valence band to the conduction band whereas (1) and (2) are photons with enough energy to excite an electron in to the intermediate band and then in to the conduction band. By using these photons the efficiency of the cell is increased. This can theoretically give up to approximately 67% efficiency [155, 156] because of the thermodynamic limit.

To produce intermediate band solar cells, indium gallium nitride PIN structures were grown with up to 30% In and 1% manganese as a dopant. Up to 30% In was chosen as all previous documented working solar cells have had less than 40% In. They have also all been deposited on high temperature GaN buffer layers to eliminate concerns about metal existing in the grain boundaries. The following samples were all grown using AME on n-GaAs. GaAs was chosen as the k-space BandiT system can be used to monitor the substrate temperature accurately.

This InGaN solar cell work was carried out as part of the IBPOWER EU program as a collaboration with Instituto di Energía Solar, Universidad Politécnica de Madrid.

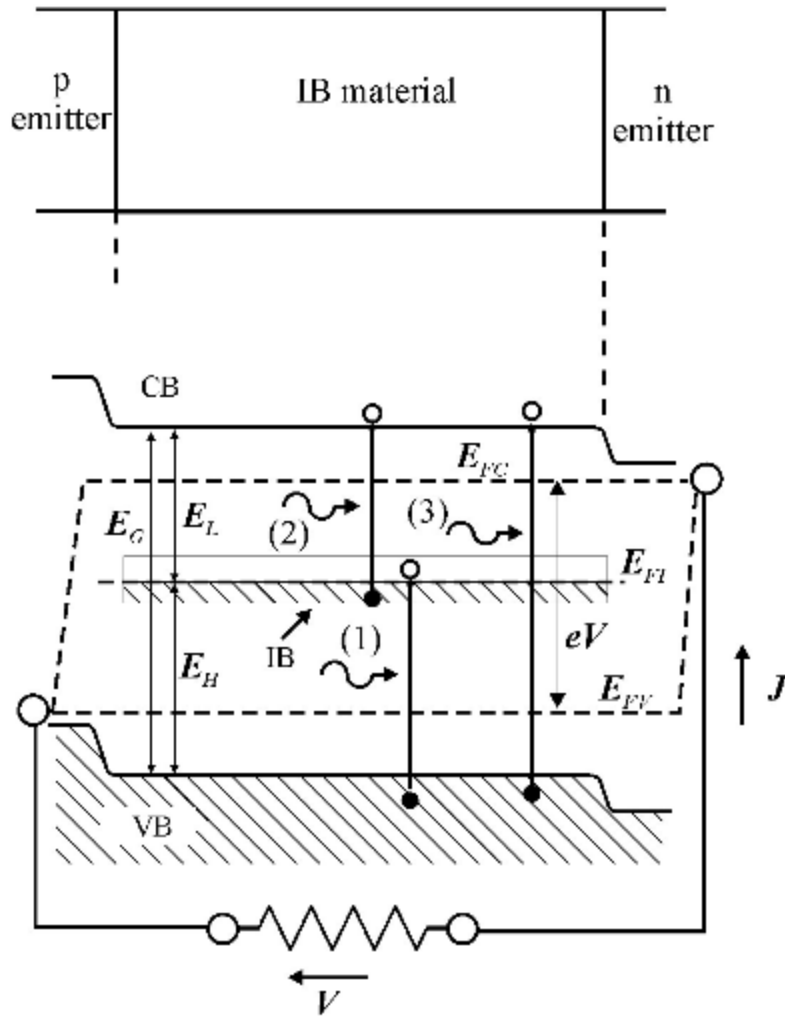


Figure 6.1: This diagram shows electron transitions in the intermediate band [117]. (1) illustrates a lower energy photon exciting an electron into the intermediate band, (2) demonstrates a lower energy photon exciting an electron from the intermediate band up to the conduction band, and (3) shows an photon with enough energy to excite an electron from the valence band all the way to the conduction band in a simple step.

6.2 Results

6.2.1 Growth on GaAs

Table 5.1 contains the samples that were processed to create solar cells and their photovoltaic response was measured by a simple 4-point probe method. A standard desk lamp was used to illuminate the samples in order to see if any responded to light. X-ray diffraction and reflectivity measurements were also taken.

Sample Number	Sample	Composition	Response to light (mV)
IB91	GaN PIN cell	0%In 0%Mn	22
IB92	GaN PIN cell	0%In 1%Mn	100
IB96	InGaN PIN cell	10%In 0%Mn	6
IB97	InGaN PIN cell	10%In 1%Mn	35
IB102	InGaN PIN cell	20%In 0%Mn	8
IB105	InGaN PIN cell	20%In 1%Mn	200

Table 6.1: Table of processed samples to create solar cells all on n-GaAs substrates.

IB91 and IB92 are both GaN PIN structures, 1% manganese has been added to IB92. Figure 6.3 shows $2\theta/\omega$ scans of the gallium nitride 002 peak. The FWHM of the samples are 0.241° and 0.237° respectively. This is an indication that the presence of manganese is not affecting the quality of the layer, or adding any strain. Optical reflectance measurements are included in the figure. The band edge can be seen at an energy corresponding to a wavelength of approximately 375nm which is the value expected for gallium nitride. The similarity of both X-ray and optical reflectivity spectra suggests that the structure of both the samples is almost identical, indicating that 1% manganese does not affect the material.

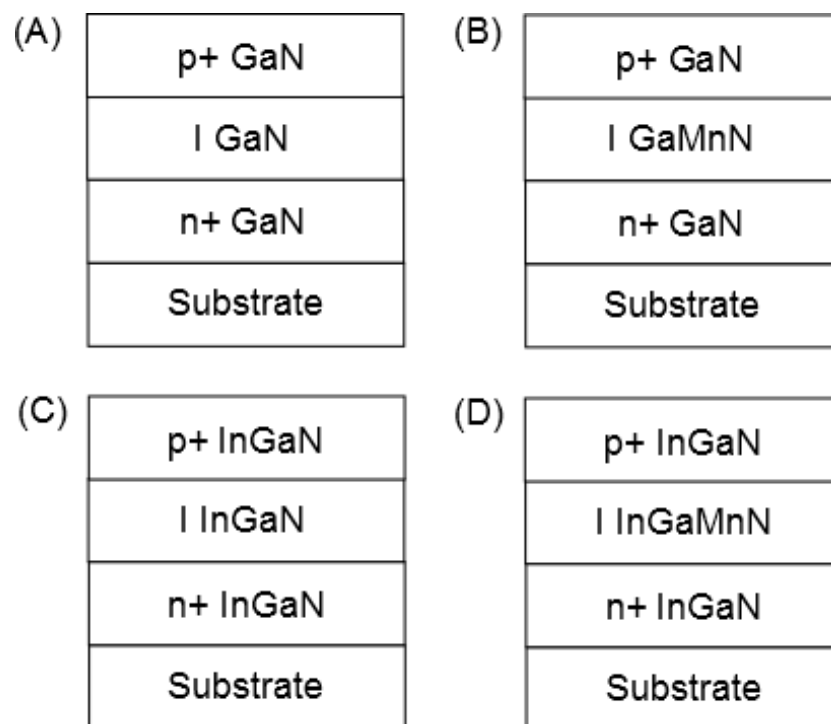


Figure 6.2: This diagram shows the the different types of samples grown using AME for solar cell testing. (A) is the reference PIN structure grown using GaN, (B) includes manganese in the intermediate region. (C) is the reference sample for InGaN PIN structures, (D) includes manganese in the intermediate region.

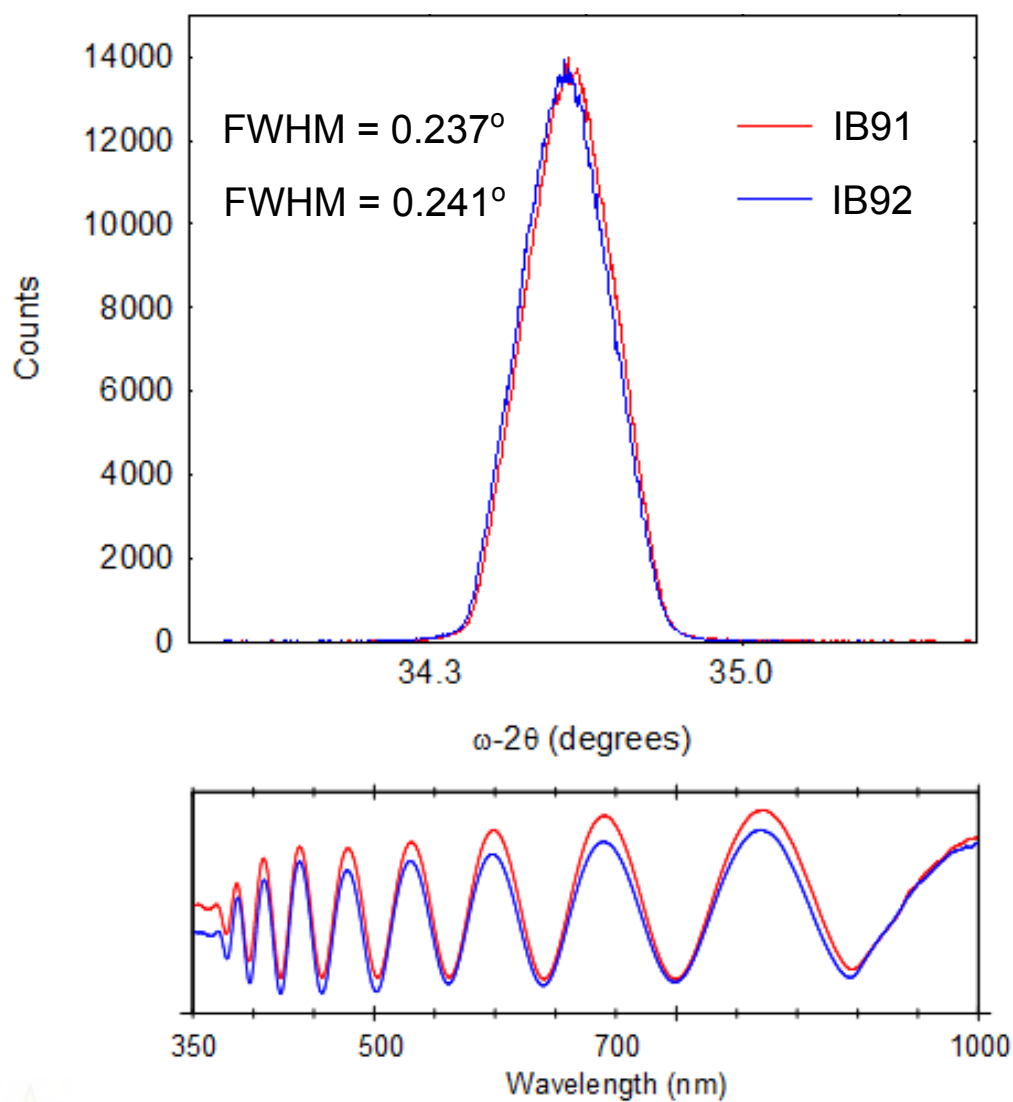


Figure 6.3: This image shows an x-ray diffraction line scan through the GaN peak for IB91 and IB92. It also includes the optical reflectance measurements for each sample.

X-ray diffraction spectra for IB96 and IB97 show a shoulder on the GaN peak which is visible in Figure 6.4. A non gaussian peak, eventually separating out into two separate peaks is expected in InGaN where phase separation occurs at high In mole fraction. Again, the FWHM measurements are similar for each sample (0.289° and 0.274° respectively) demonstrating that the manganese does not cause any significant dislocations produced by strain energy within the layer. However manganese does modify slightly the shape of the shoulder, which is better resolved without the manganese. The reflectance spectrum shows that the band edge has shifted towards longer wavelength (lower energies) slightly due to the added indium compared with the samples shown in Figure 6.3. Also, the reflectance spectra are in phase with each other but at energies below 500nm is reached, they start to become out of phase.

For the 20% In samples (IB102 and IB105), it can be seen in Figure 6.5 that the diffraction peaks have resolved and there is no longer a shoulder on the side of the gallium nitride peak. The FWHM values are almost unchanged (0.253° for IB102 and 0.252° for IB105) but there is some reduction in layer quality by adding manganese as the position of the peak has shifted. During the growth of these samples, the RHEED diffraction pattern started changing into one that was thought to indicate phase separation. The X-ray diffraction data however does not confirm this and so now is believed that stacking faults are to blame for the changes observed in the RHEED pattern. A reciprocal space map should be taken to confirm this. The reflectance spectra for these samples have remained in phase but with a reduced amplitude. This indicates that the layers have similar refractive indices to each other, but the reduction in amplitude could be due to non-parallel layers, or roughness of the layers on a scale comparable to λ .

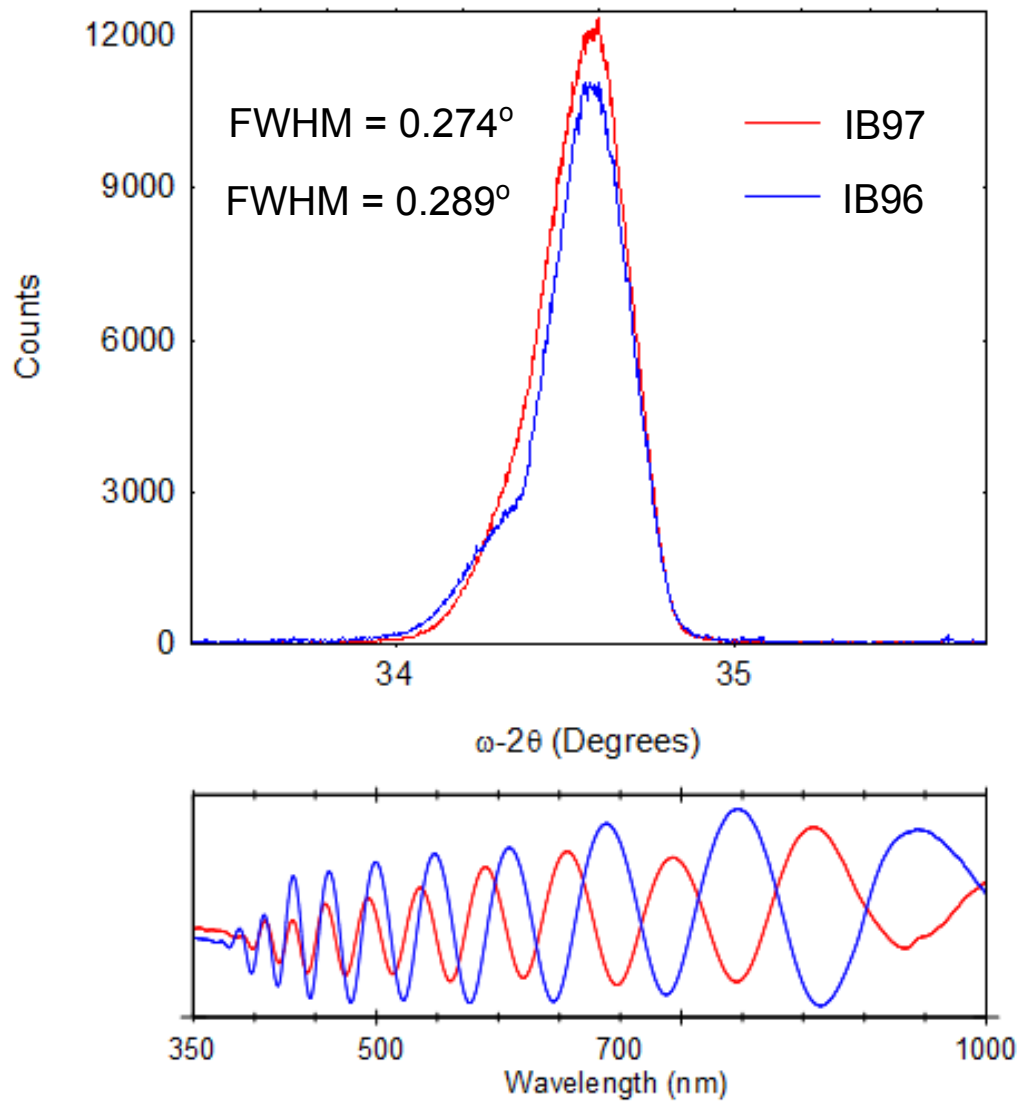


Figure 6.4: This image shows an x-ray diffraction line scan through the GaN peak for IB96 and IB97. Optical reflectance measurements are also present.

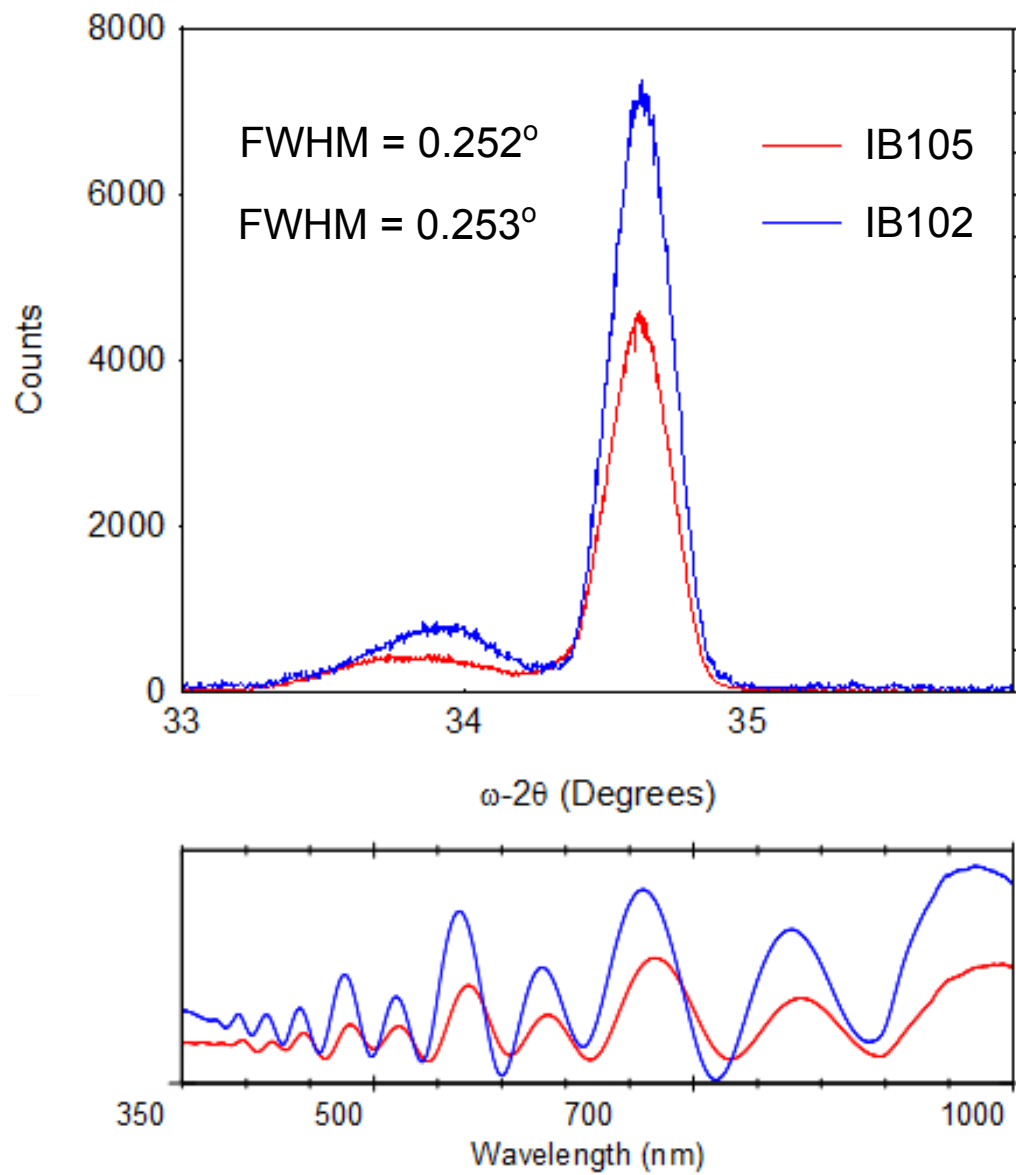


Figure 6.5: This image shows x-ray diffraction line scans through the gallium nitride peak for IB91 and IB92.

The External Quantum Efficiency (EQE) was measured for samples IB102 and IB105. These samples were patterned and fabricated into solar cells in order to perform quantum efficiency measurements which were carried out at Instituto di Energía Solar, Universidad Politécnica de Madrid. Quantum Efficiency (QE) is a measure of the current the cell will produce when irradiated by photons. EQE is the ratio of the number of charge carriers collected by the solar cell to the number of incident photons of a given energy. Once a photon has been absorbed and has generated an electron-hole pair, these charges must be separated and collected at the junction. Charge recombination causes a drop in QE to a lower EQE value and a ‘good’ material will avoid it. Incorporation of 1% manganese was hoped to increase the EQE. Figure 6.6 shows the EQE data for an InGaN reference sample (IB102) and the same growth parameters, but with 1% manganese added. The gallium arsenide band edge is 1.5eV and a solar cell should show activity below this. There is some absorption leading to a current below the band edge but no significant difference between the two samples.

6.2.2 Growth on Sapphire

The invaluable lessons learnt about the growth procedure on n-GaAs (111) were transferred to grow sample layers on sapphire. The lattice mismatch between the substrate and the layer is reduced from 20% to around 17% by changing from GaAs to sapphire. Mismatch is greater than 20% between gallium nitride and gallium arsenide. This reduces the strain within the layers which can limit the response to light.

The solubility of manganese within gallium nitride is very temperature sensitive with only a narrow temperature window existing in which doping can occur. Using gallium arsenide has meant the BandiT can be used for

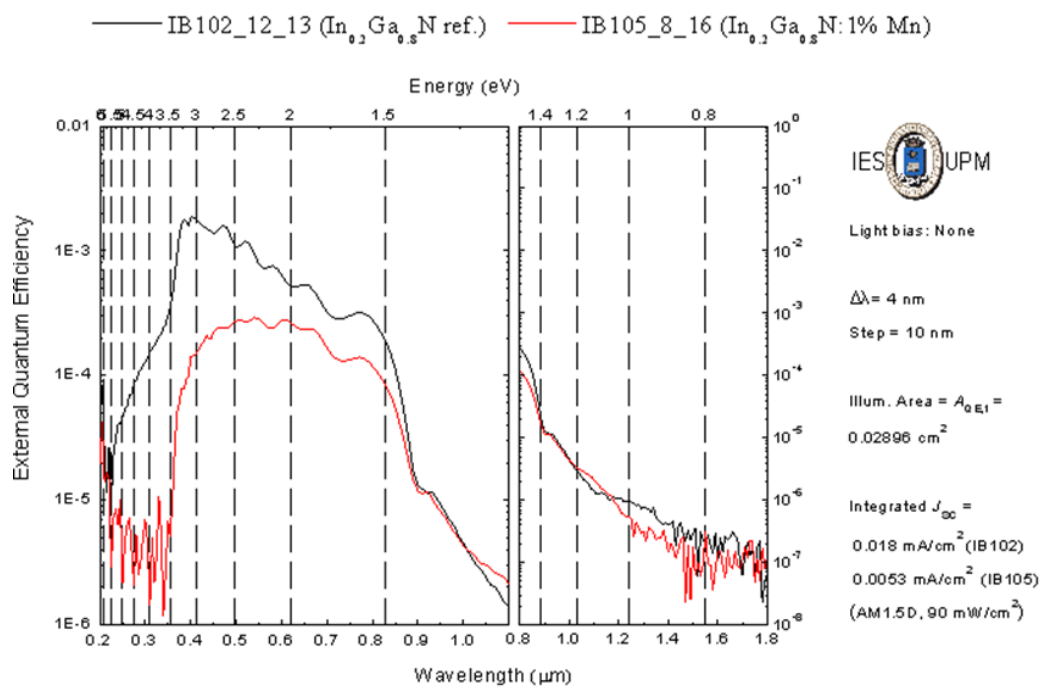


Figure 6.6: This image shows the external quantum efficiency for IB102 and IB105.

accurate temperature monitoring. There is also the large difference in interatomic spacing between indium nitride and gallium nitride which results in the miscibility gap as shown in Figure 6.7 (A). Indium gallium nitride decomposes into high and low In% fractions. The layer can undergo two different types of decomposition, binodal [157, 158] and spinodal [159, 160] depending on the indium percentage. Binodal decomposition means that the layer breaks down into two distinct phases which requires nucleation. Microscope images of a surface that has undergone binodal composition will show islands of each phase on the surface. Spinodal decomposition is the rapid ‘un-mixing’ of a layer. There is no thermodynamic barrier to a phase change inside the spinodal region, the decomposition is solely determined by diffusion.

At high growth temperatures, InGaN containing 50% In can be grown. However, as the layer is cooled, the thermodynamic equilibrium changes and the alloy breaks down into two compositional phases that are more energetically favourable and lie outside of the spinodal curve, but still inside the binodal. The material will then be metastable with respect to compositional fluctuations.

There is also the relatively high vapour pressure of indium and nitrogen in equilibrium with indium nitride compared to the vapour pressure above gallium nitride. This can lead to low indium incorporation in the alloy.

Figure 6.7 (B) is a three dimensional representation of the InGaMnN phase space and is an empirical diagram based on the observations made over the whole of the IBPOWER project that funded this work. At low indium percentages, up to 5% manganese is easily incorporated in to the layer. As the indium percentage is increased, the maximum manganese incorporation decreases over the whole temperature range.

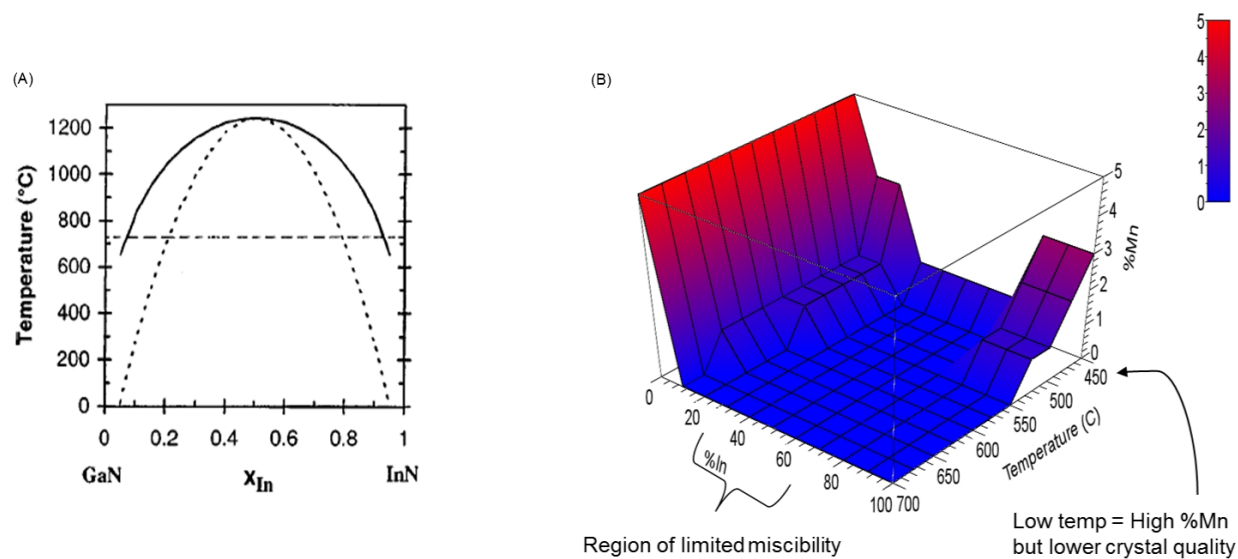


Figure 6.7: (A) Thermodynamic model showing the tendency for InGaN to decompose into high and low In% fractions. The horizontal dashed line shows the stable compositions at a given temperature [38]. Binodal decomposition is represented by the solid curve and spinodal by the dashed curve. (B) A three dimensional representation of the InGaN plus Mn phase space.

The sapphire substrates used were undoped, which requires an extra layer of n-GaN to be grown in order to create PIN structures.

After testing the resistivities of the samples grown on gallium arsenide, it was found that most of them were not conducting. This could be a sign that the material is growing in a columnar manner and a possible explanation for the previous indium nitride samples not producing metal on the surface (see sections 5.5).

Growth on sapphire had not been attempted previously as the bandiT system can not be used to monitor the temperature of the surface throughout growth. Initial growths of Gallium nitride on undoped sapphire were carried out to see if the same high quality n-GaN could be produced as with GaAs.

Figure 6.8 shows SEM images of some InGaN on GaAs (A) as well as n-GaN on sapphire (B and C). The InGaN morphology appears to show that numerous islands were nucleated and have grown laterally but not necessarily coalesced together. The gaps between the uncoalesced islands are where the excess metal is being stored within the layer. The n-GaN layers are generally well formed but dotted all over the surface are these ‘brain-like’ structures that could be attributed to spinodal decomposition [159, 160]. One hypothesis for these are that they were originally metal droplets on the surface and gallium nitride has formed on top.

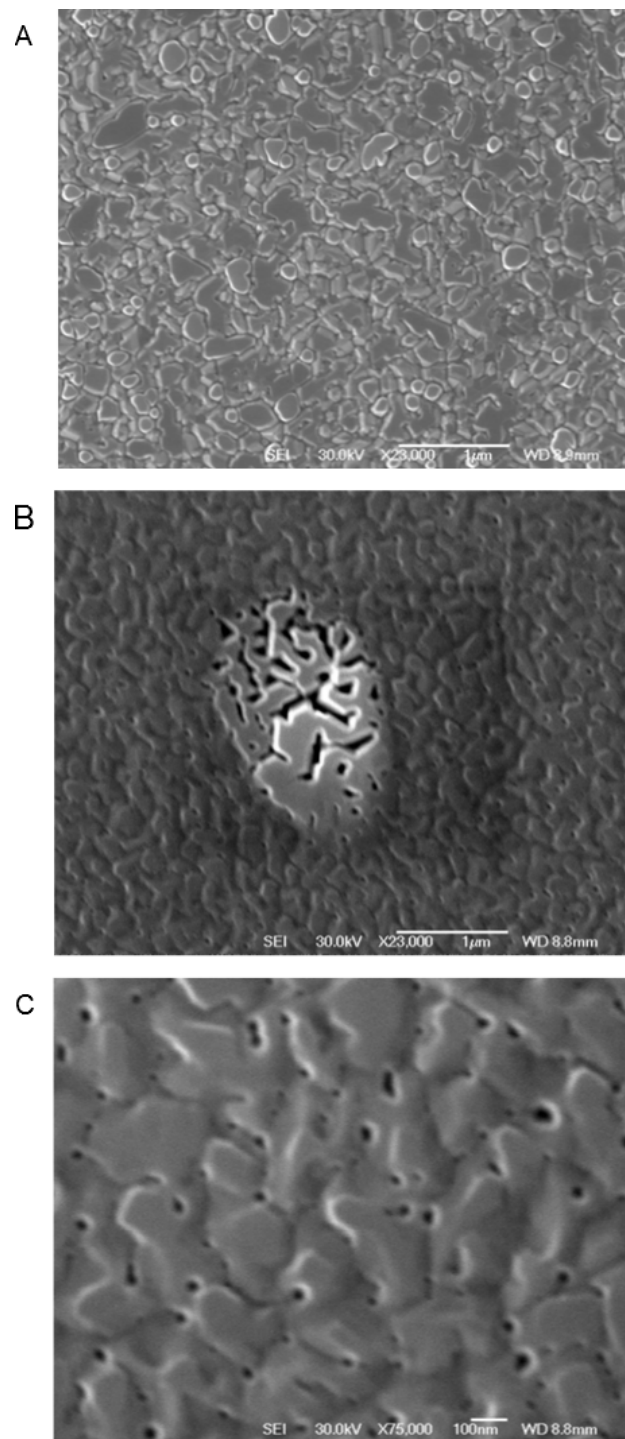


Figure 6.8: SEM images of (A) InGaN 10% In, 1 % Mn at $\times 23,000$, (B) n-GaN on sapphire at $\times 23,000$ and $\times 75,000$ magnification.

6.3 Conclusions

AME has been used to improve the growth of PIN structures for intermediate band solar cells. This new growth technique has allowed the entire growth to be carefully monitored and altered throughout with relative ease. It has also allowed the narrow growth window for p-doped gallium nitride to be broadened and become more reproducible.

AME also led to the discovery of excess metal filling up the grain boundaries. The typical growth rate graph with the thickness of the layer levelling off to stay the same even though more metal was being used each time was not produced because of the grain boundaries being filled up with liquid metal. The excess metal was only 'found' after the intermediate layer in the PIN structures were grown. All of the metal appeared at the surface once the p-GaN growth was initiated. AME allowed this sudden appearance of metal to be easily controlled by shutting off the group III fluxes for longer periods in order for it to be used up without ruining the sample.

Chapter 7

Summary of Results and Future Work

The main focus of this thesis was to investigate growth methods and properties principally of GaN and InN with the eventual aim of combining the methods to grow InGaN. A dominant part of this work has centred on a new growth technique known as Anion Modulation Epitaxy (AME). This technique has shown improved quality of growth compared with Plasma Assisted MBE. AME is a method that periodically interrupts the nitrogen flux incident upon the sample surface to allow a build up in concentration of group III material (normally around 2 monolayers). At the end of each growth cycle the amount of excess group III has returned to zero and the cycle of interrupting the nitrogen repeats. This technique can be easily monitored during growth using RHEED as well as utilising visible light reflected from the surface at low angles of incidence on the system to visually monitor build up of metal on the surface.

When comparing the sets of samples grown by PA-AME and AME, AME samples show improved structural, electrical and optical properties. AME

samples were also shown to improve doping efficiencies at lower temperatures.

Temperature changes at the surface were also investigated whilst using the AME growth technique. With any pulsed method, temperature variations within a growth cycle should be expected. The substrate temperature was found to vary in a cyclic manner by up to 15°C each time the nitrogen flow was interrupted. As well as this, the overall temperature drift up or down throughout the entire growth gives an indication as to whether there is some metal left on the surface or not as each cycle ends. Small amounts of metal left on the surface lead to an overall increase of the temperature throughout growth whereas a drift downwards can be attributed to nitrogen rich periods of growth at the end of each cycle. It can be assumed that this would be the minimum temperature change experienced by other modulated beam methods such as Metal Modulation Epitaxy (MME) as one or metal sources are periodically shut to create the same overall effect.

In Chapter 6, AME was also used in the growth of intermediate band solar cells. This technique provided more control over the entire growth and improved the success rate of p-doping of GaN. Using conventional MBE, the growth window for p-GaN is narrow and provides varied results.

In Chapter 4, InN nanorod growth was investigated on 6H-SiC substrates. Nanorods were grown on both Si- and C-face substrates successfully. Optimum growth conditions were found to be a BEP flux of $\sim 2.0 \times 10^{-7}$ Torr and a growth temperature of 400° measured on the substrate thermocouple. Nanorod coalescence was also investigated and readily achieved by increasing the nitrogen flux to $\sim 2.0 \times 10^{-6}$ Torr. CBED analysis was carried out on the rods and the tall columns were found to grow In-polar. This suggests that the shorter rods in the underlayer will be growing N-polar and form in a slower growth mode. Photoluminescence was carried out on the samples

and the spectra obtained are in good agreement with those obtained from samples grown by other techniques. This is an indication that reasonable quality InN has been grown. Both faces of the SiC have been used to grow p-n junctions and have shown a reaction to light during preliminary tests. This is encouraging for the final aim of creating a solar energy conversion device.

Future work should include further investigation of p-doping capabilities of GaN using AME. Consistent p-doping is still an ongoing problem in the growth of GaN and if it can be done within a larger temperature window then this would increase the chance of consistency through sample sets.

It would also be interesting to carry out transport measurements on the heterostructures mentioned in chapter 4. Transport data has not been taken during this thesis but it would be advantageous to carry this out for comparisons with literature.

With regards to the nanorods, grading the growth throughout to produce InGaN rods is a plausible next step. Tuning the rods by grading the growth ensures that all of the suns energy can be made use of by the device to produce electricity. More TEM and CBED analysis should be carried out on the samples to confirm the polarity of the under-layer in the InN nanocolumn samples as it is only assumed to be growing N-polar. Photoluminescence data is also important for characterisation of the samples, however the appropriate detector for InN was not available. This would potentially reveal more about the alignment of the nanocolumns and the structural properties of the columns.

Bibliography

- [1] V.Yu. Davydov, A.A. Klochikhin, V.V. Emtsev, S.V. Ivanov, V.V. Vekshin, F. Bechstedt, J. Furthmüller, H. Harima, A.V. Mudryi, A. Hashimoto, A. Yamamoto, J. Aderhold, J. Graul, and E.E. Haller. Band gap of inn and in-rich $\text{In}_{x}\text{Ga}_{1-x}\text{N}$ alloys ($0.36 \leq x \leq 1$). *physica status solidi (b)*, 230(2):R4–R6, 2002.
- [2] J W Orton and C T Foxon. Group iii nitride semiconductors for short wavelength light-emitting devices. *Reports on Progress in Physics*, 61(1):1, 1998.
- [3] S. Misawa H. Yamashita, K. Fukui and S. Yoshida. Optical properties of AlN epitaxial thin films in the vacuum ultraviolet region. *Journal of Applied Physics*, 50:896, 1979.
- [4] S. Strite and H. Morkoc. GaN, AlN, and InN: A review. *Journal of Vacuum Science and Technology B*, 10:1237, 1992.
- [5] T. Tanabe Y. Yoshizumi, S. Hashimoto and M. Kiyama. High-breakdown-voltage pn-junction diodes on GaN substrates. *Journal of crystal growth*, 298:875, 2007.
- [6] Ki C.g Jeong J. Ha T. Jeong, J. Baek and H. Ryu. Investigation of light extraction efficiency and internal quantum efficiency in high-power

- vertical blue light-emitting diode with 3.3 W output power. *Japanese Journal of Applied Physics*, 52:10MA09, 2013.
- [7] N. Iwasa S. Nakamura, M. Senoh and S. Nagahama. High-Brightness InGaN Blue, Green and Yellow Light-Emitting Diodes with Quantum Well Structures. *Japanese Journal of Applied Physics*, 34:L797, 1995.
- [8] M. P. DEvelyn S. D. Arthur J. Kretchmer C. H. Yan X. A. Cao, S. F. LeBoeuf and Z. H. Yang. Blue and near-ultraviolet light-emitting diodes on free-standing GaN substrates. *Applied Physics Letters*, 84:4313, 2004.
- [9] Y. Yamashita Y. Takagi K. Uchiyama H. Yoshida, M. Kuwabara and H. Kan. AlGaIn-based laser diodes for the short-wavelength ultraviolet region. *New Journal of Physics*, 11:125013, 2009.
- [10] C. Wu W. Chen J. Chen H.-Y. Chen, H. Lin and S. Gwo. Gallium nitride nanorod arrays as low-refractive-index transparent media in the entire visible spectral region. *Optics Express*, 16:8106, 2008.
- [11] H. Luo E. F. Schubert, J. K. Kim and J.-Q. Xi. Solid-state lighting-a benevolent. *Reports on Progress in Physics*, 69:3069, 2006.
- [12] S. Gwo and H.-Y. Chen. Gallium-nitride nanorods serve as subwavelength optical media. *SPIE Newsroom*, page 10.1117/2.1200902.1524, 2009.
- [13] H.-W. Lin S.-C. Chang H.-Y. Chen, Y.-C. Yang and S. Gwo. Polarized photoluminescence from single GaN nanorods: Effects of optical confinement. *Optics Express*, 16:13465, 2008.

- [14] R. Sharma E. L. Hu S. P. DenBaars T. Fujii, Y. Gao and S. Nakamura. Increase in the extraction efficiency of gan-based light-emitting diodes via surface roughening. *Applied Physics Letters*, 84:855, 2004.
- [15] J. Y. Lin T. N. Oder, K. H. Kim and H. X. Jiang. Iii-nitride blue and ultraviolet photonic crystal light emitting diodes. *Applied Physics Letters*, 84:466, 2004.
- [16] J. E. Epler N. F. Gardner M. G. Craford J. R. Wendt J. A. Simmons J. J. Wierer, M. R. Krames and M. M. Sigalas. Ingan/gan quantum-well heterostructure light-emitting diodes employing photonic crystal structures. *Applied Physics Letters*, 84:3885, 2004.
- [17] R. Sharma K. McGroddy S. Nakamura S. P. DenBaars E. L. Hu C. Weisbuch A. David, T. Fujii and H. Benisty. Photonic-crystal gan light-emitting diodes with tailored guided modes distribution. *Applied Physics Letters*, 88:061124, 2006.
- [18] C.J. Humphreys. Solid-state Lighting. *MRS Bulletin*, 33:459, 2008.
- [19] Energy Efficiency and U.S. Department of Energy Renewable Energy. Building energy databook 2011. <http://buildingsdatabook.eren.doe.gov/>, 2011.
- [20] International Energy Agency Paris. Key world energy statistics 2014. <https://www.iea.org/publications/freepublications/publication/KeyWorld2014.pdf>, 2014.
- [21] International Energy Agency Paris. Light's labour's lost: Policies for energy-efficient lighting. <https://www.iea.org/publications/freepublications/publication/light2006.pdf>, 2006.

- [22] S. F. Bevacqua N.Holonyak. Coherent (visible) Light Emission from Ga(As_{1-x}P_x) junctions. *Applied Physics Letters*, 1:82, 1962.
- [23] M. Elimelech J. G. Georgiadis B. J. Marias M. A. Shannon, P. W. Bohn and A. M. Mayes. Science and technology for water purification in the coming decades. *Nature*, 452:301, 2007.
- [24] R. M. Matthews. Purification of water with near - u.v. illuminated suspensions of titanium dioxide. *Water Research*, 24:653, 1990.
- [25] J. R. Moelle J. Calkins, J. D. Buckles. The role of solar ultraviolet radiation in natural water purification. *Photochemistry and Photobiology*, 24:49, 1976.
- [26] S. Hager and R. Bauer. Heterogeneous photocatalytic oxidation of organics for air purification by near UV irradiated titanium dioxide. *Chemosphere*, 28:1549, 1999.
- [27] J. Zhao and X. Yang. Photocatalytic oxidation for indoor air purification: a literature review. *Building and Environment*, 38:645, 2003.
- [28] J.-N. Chen C.-P. Chang and M.-C. Lu. Heterogeneous photocatalytic oxidation of acetone for air purification by near UV-irradiated titanium dioxide. *Journal of Environmental Science and Health, Part A: Toxic/Hazardous Substances and Environmental Engineering*, 38:1131, 2003.
- [29] Q. Xua J. J. Lamsona J. Moa, Y. Zhanga and R. Zhaoa. Photocatalytic purification of volatile organic compounds in indoor air: A literature review. *Atmospheric Environment*, 43:2229, 2009.

- [30] C. Scotto V. Sivaprakasam, A. L. Huston and J. D. Eversole. Multiple uv wavelength excitation and fluorescence of bioaerosols. *Optics Express*, 12:4457, 2004.
- [31] P. E. Sheehan M. M. Miller D. R. Baselt L. J. Whitman R. L. Edelsteina, C. R. Tamanaha and R. J. Colton. The barc biosensor applied to the detection of biological warfare agents. *Biosensors and Bioelectronics*, 14:805, 2000.
- [32] G. Hempel. Strategies to improve the sensitivity in capillary electrophoresis for the analysis of drugs in biological fluids. *Electrophoresis*, 21:691, 2000.
- [33] E. J. Lynch T. J. Jeys, L. Desmarais and J. R. Ochoa. Development of a uv-led-based biosensor. *SPIE Proceedings*, 5071, 2003.
- [34] R. Blomhoffa A. Karlsema and T. E. Gundersen. High-throughput analysis of Vitamin C in human plasma with the use of HPLC with monolithic column and UV-detection. *Journal of Chromatography B*, 824:132, 2005.
- [35] C. A. Boulet C. A. Lucy J. E. Melanson, B. L.-Y. Wong. High-sensitivity determination of the degradation products of chemical warfare agents by capillary electrophoresis indirect UV absorbance detection. *Journal of Chromatography A*, 920:359, 2001.
- [36] B. Mohammadi G. Bahrami and A. Kiani. Determination of oseltamivir carboxylic acid in human serum by solid phase extraction and high performance liquid chromatography with UV detection. *Journal of Chromatography B*, 864:38, 2008.

- [37] S. Mirzaeei G. Bahramia, B. Mohammadi and A. Kiani. Determination of atorvastatin in human serum by reversed-phase high-performance liquid chromatography with UV detection. *Journal of Chromatography B*, 826:41, 2005.
- [38] I.-C. Ho and G. B. Stringfellow. Solid phase immiscibility in GaInN. *Applied Physics Letters*, 69(18):2701–2703, 1996.
- [39] M. Funato S. Fujita Y. Narukawa, Y. Kawakami and S. Nakamura. Role of self-formed ingan quantum dots for exciton localization in the purple laser diode emitting at 420 nm. *Applied Physics Letters*, 70:981, 1997.
- [40] N. Sharma C.J. Humphreys G.M. Yang C.S. Kim H.K. Cho, J.Y. Lee and J.H. Song. Effect of growth interruptions on the light emission and indium clustering of InGaN/GaN multiple quantum wells. *Applied Physics Letters*, 79:2594, 2001.
- [41] J.S. Barnard M.E. Vickers T.M. Smeeton, M.J. Kappers and C.J. Humphreys. Electron-beam-induced strain within InGaN quantum wells: False indium cluster detection in the transmission electron microscope. *Applied Physics Letters*, 83:5419, 2003.
- [42] S. Yu. Karpov. Suppression of phase separation in InGaN due to elastic strain. *MRS Internet Journal of Nitride Semiconductor Research*, 3:16, 1998.
- [43] C. J. Humphreys. Does In form In-rich clusters in InGaN quantum wells? *Philosophical Magazine*, 87:1971, 2007.
- [44] M.J. Kappers C.J. Humphreys D.J. Stokes P.H. Clifton M.J. Galtrey, R.A. Oliver and A. Cerezo. Three-dimensional atom probe studies of

- an In_xGa_{1-x}N/GaN multiple quantum well structure: Assessment of possible indium clustering. *Applied Physics Letters*, 90:061903, 2007.
- [45] P. Dawson M. J. Godfrey T. M. Smeeton J. S. Barnard M. J. Kappers C. J. Humphreys D. M. Graham, A. Soltani-Vala and E. J. Thrush. Optical and microstructural studies of InGaN/GaN single-quantum-well structures. *Journal of Applied Physics*, 97:103508, 2005.
- [46] C. J. Humphreys. Does in form in-rich clusters in ingan quantum wells? *Philosophical Magazine*, 87:1971, 2007.
- [47] H. M. Manasevit and W. I. Simpson. The use of Metal-Organics in the Preparation of Semiconductor Materials: I. Epitaxial Gallium-V Compounds. *Journal of Tthe Electrochemical Society*, 116:1725, 1969.
- [48] M. Cooke. First ammonia MBE nitride HEMTs on silicon. *Semiconductor Tday Compounds & Advanced Silicon*, 7:86, 2012.
- [49] B. Damilano N. Grandjean and J. Massies. Group-III nitride quantum heterostructures grown by molecular beam epitaxy. *Journal of Physics: Condensed Matter*, 13:6945, 2001.
- [50] H. Tang J.B. Webb S.J. Rolfe J. Lapointe Electron. Lett. 39 564 (2003). J.A. Bardwell, Y. Liu. AlGa_N/Ga_N HFET devices on SiC grown by ammonia-MBE with high f_T and f_{MAX}. *Electronics Letters*, 39:564, 2003.
- [51] T. J. Kempa Y. Dong, B. Tian and C. M. Lieber. Coaxial group III nitride nanowire photovoltaics. *Nano Letters*, 9:2183, 2009.
- [52] E. C. Garnett and P. Yang. Silicon nanowire radial pn junction solar cells. *Journal of the American Chemical Society*, 130:9224, 2008.

- [53] D. A. Thompson J. A. Czaban and R. R. LaPierre. Gaas core-shell nanowires for photovoltaic applications. *Nano Letters*, 9:148, 2009.
- [54] J. C. Johnson R. Saykally M. Law, L. E. Greene and P. Yang. Nanowire dyesensitized solar cells. *Nature Materials*, 4:455, 2005.
- [55] A. I. Persson L. Landin D. Hessman H. Pettersson, J. Tragardh and L. Samuelson. Infrared photodetectors in heterostructure nanowires. *Nano Letters*, 6:229, 2006.
- [56] X. Duan Y. Cui J. Wang, M. S. Gudixsen and C. M. Lieber. Highly polarized photoluminescence and photodetection from single indium phosphide nanowires. *Science*, 293:1455, 2001.
- [57] J. L. Lensch J. E. Allen T.W. Odom Y. Gu, E.-S. Kwak and L. J. Lauhon. Nearfield scanning photocurrent microscopy of a nanowire photodetector, *appl. phys. lett.*, vol. 87, no. 4, p. 043111, 2005. *Applied Physics Letters*, 87:043111, 2005.
- [58] A. V. Maslov C. Z. Ning M. K. Sunkara A. H. Chin, S. Vaddiraju and M. Meyyappan. Near-infrared semiconductor subwavelength-wire lasers. *Applied Physics Letters*, 88:163115, 2006.
- [59] R. Agarwal X. F. Duan, Y. Huang and C. M. Lieber. Single-nanowire electrically driven lasers. *Nature*, 421:241, 2003.
- [60] C. J. Barrelet R. Agarwal and C. M. Lieber. Lasing in single cadmium sulfide nanowire optical cavities. *Nano Letters*, 5:917, 2005.
- [61] H. Feick H. Yan Y. Wu H. Kind E. Weber R. Russo M. H. Huang, S. Mao and P. Yang. Room-temperature ultraviolet nanowire nanolasers. *Science*, 292:1897, 2001.

- [62] S. Gradecak H.-G. Park Y. Dong Y. Ding Z. L. Wang F. Qian, Y. Li and C. M. Lieber. Multi-quantum-well nanowire heterostructures for wavelength-controlled lasers. *Nature Materials*, 7:701, 2008.
- [63] Y. Kobayashi S. Hara B. Hua, J. Motohisa and T. Fukui. Single GaAs/GaAsP coaxial core-shell nanowire lasers. *Nano Letters*, 9:112, 2009.
- [64] Y. Li C.-Y. Wen F. Qian, S. Gradecak and C. Lieber. Core/multishell nanowire heterostructures as multicolor, high-efficiency light-emitting diodes. *Nano Letters*, 5:2287, 2005.
- [65] M. van Kouwen J. A. van Dam L. P. Kouwenhoven V. Zwiller M. T. Borgstrom O. Wunnicke M. A Verheijen E. D. Minot, F. Kelkensberg and E. P. A. M. Bakkers. Single quantum dot nanowire leds. *Nano Letters*, 7:367, 2007.
- [66] C. Thelander A. I. Persson K. Deppert L. R. Wallenberg M. T. Bjork, B. J. Ohlsson and L. Samuelson. Nanowire resonant tunneling diodes. *Applied Physics Letters*, 81:4458, 2002.
- [67] A. B. Greytak C. J. Barrelet and C. M. Lieber. Nanowire photonic circuit elements. *Nano Letters*, 4:1981, 2004.
- [68] E. Muller M. T. Borgstrom, V. Zwiller and A. Imamoglu. Optically bright quantum dots in single nanowires. *Nano Letters*, 5:1439, 2005.
- [69] S. Abay C. Wilson J. B. Wagner C. Thelander P. Delsing H. A. Nilsson, T. Duty and L. Samuelson. A radio frequency single-electron transistor based on an InAs/InP heterostructure nanowire. *Nano Letters*, 8:872, 2008.

- [70] L. E. Froberg J. B. Wagner H. A. Nilsson, C. Thelander and L. Samuelson. Nanowire-based multiple quantum dot memory. *Applied Physics Letters*, 89:163101, 2006.
- [71] L. E. Jensen C. Thelander, H. A. Nilsson and L. Samuelson. Nanowire single electron memory. *Nano Letters*, 5:635, 2005.
- [72] A. E. Hansen L. E. Jensen M. W. Larsson L. R. Wallenberg M. T. Bjork, C. Thelander and L. Samuelson. Few-electron quantum dots in nanowires. *Nano Letters*, 4:1621, 2004.
- [73] M. T. Bjork B. J. Ohlsson M. W. Larsson L. R. Wallenberg C. Thelander, T. Martensson and L. Samuelson. Single-electron transistors in heterostructure nanowires. *Applied Physics Letters*, 83:2052, 2003.
- [74] A. L. Roest M. Kaiser T. H. Oosterkamp E. C. Heeres, E. P. A. M. Bakkers and N. de Jonge. Electron emission from individual indium arsenide semiconductor nanowires. *Nano Letters*, 7:536, 2007.
- [75] T. Lowgren T. Bryllert, L.-E. Wernersson and L. Samuelson. Vertical wrap-gated nanowire transistors. *Nanotechnology*, 17:S227, 2006.
- [76] T. Yamada P. Nguyen Y. P. Chen H. T. Ng, J. Han and M. Meyyappan. Single crystal nanowire vertical surround-gate field-effect transistor. *Nano Letters*, 4:1247, 2004.
- [77] L. Samuelson E. Lind, A. I. Persson and L.-E. Wernersson. Improved subthreshold slope in an InAs nanowire heterostructure field-effect transistor. *Nano Letters*, 6:1842, 2006.

- [78] H. Schmid H. Riel M. T. Bjork, O. Hayden and W. Riess. Vertical surroundgated silicon nanowire impact ionization field-effect transistors. *Applied Physics Letters*, 90:142110, 2007.
- [79] M. Loncar H.-G. Park F. Capasso C. J. Barrelet, J. Bao and C. M. Lieber. Hybrid single-nanowire photonic crystal and microresonator structures. *Nano Letters*, 6:11, 2006.
- [80] Y. Wu-B. Tian F. Qian H.-G. Park, C. J. Barrelet and C. M. Lieber. A wavelength-selective photonic-crystal waveguide coupled to a nanowire light source. *Nature Photonics*, 2:662, 2008.
- [81] H. Park Y. Cui, Q. Wei and C. M. Lieber. Nanowire nanosensors for highly sensitive and selective detection of biological and chemical species. *Science*, 293:1289, 2001.
- [82] J.-I. Hahm and C. M. Lieber. Direct ultrasensitive electrical detection of DNA and DNA sequence variations using nanowire nanosensors. *Nano Letters*, 4:51, 2004.
- [83] T. Sass-A. I. Persson C. Thelander M. H. Magnusson K. Deppert L. R. Wallenberg M. T. Bjork, B. J. Ohlsson and L. Samuelson. One-dimensional heterostructures in semiconductor nanowhiskers. *Applied Physics Letters*, 80:1058, 2002.
- [84] J.Wang D. C. Smith M. S. Gudiksen, L. J. Lauhon and C. M. Lieber. Growth of nanowire superlattice structures for nanoscale photonics and electronics, nature, vol. 415, no. 6872, pp. 617620, 2002. *Nature*, 415:617, 2002.
- [85] C. M. Lieber. Nanoscale science and technology: Building a big future from small things. *MRS Bulletin*, 28:486, 2003.

- [86] M. T. Bjork M. Borgstrom K. Deppert K. A. Dick A. E. Hansen T. Martensson N. Panev A. I. Persson W. Seifert N. Skold M. W. Larsson L. Samuelson, C. Thelander and L. R. Wallenberg. Semiconductor nanowires for 0d and 1d physics and applications. *Physica E*, 25:313, 2004.
- [87] M. Paladugu H. Wang Q. Gao H. H. Tan Y. N. Guo, J. Zou and C. Jagadish. Structural characteristics of gasb/gaas nanowire heterostructures grown by metal-organic chemical vapor deposition, appl. phys. lett., vol. 89, no. 23, p. 231917, 2006. *Applied Physics Letters*, 89:231917, 2006.
- [88] D. C. Chrzan E. Ertekin, P. A. Greaney and T. D. Sands. Equilibrium limits of coherency in strained nanowire heterostructures. *Journal of Applied Physics*, 97:114325, 2005.
- [89] M. Wallin P. Hakansson L. E. Froberg L. Samuelson M. W. Larsson, J. B. Wagner and L. R. Wallenberg. Strain mapping in free-standing heterostructured wurtzite inas/inp nanowires. *Nanotechnology*, 18:015504, 2007.
- [90] B. A. Wacaser M. W. Larsson W. Seifert K. Deppert A. Gustafsson L. R. Wallenberg T. Martensson, C. P. T. Svensson and L. Samuelson. Epitaxial IIIV nanowires on silicon, nano lett., vol. 4, no. 10, pp. 19871990, 2004. *Nano Letters*, 4:1987, 2004.
- [91] S. De Franceschi L. P. Kouwenhoven M. Kaiser M. Verheijen H. Wondergem E. P. A. M. Bakkers, J. A. van Dam and P. van der Sluis. Epitaxial growth of InP nanowires on germanium, nature mater., vol. 3, no. 11, pp. 769773, 2004. *Nature Materials*, 3:769, 2004.

- [92] C. Chase N. P. Kobayashi C. Chang-Hasnain L. C. Chuang, M. Moewe and S. Crankshaw. Critical diameter for iiiv nanowires grown on lattice-mismatched substrates, *appl. phys. lett.*, vol. 90, no. 4, p. 043115, 2007. *Applied Physics Letters*, 90:043115, 2007.
- [93] S. Crankshaw L. C. Chuang, M. Moewe and C. Chang-Hasnain. Optical properties of InP nanowires on Si substrates with varied synthesis parameters. *Applied Physics Letters*, 92:013121, 2008.
- [94] M. C. Reuter K. Deppert L. Samuelson-W. Seifert L. R. Wallenberg K. A. Dick, S. Kodambaka and F. M. Ross. The morphology of axial and branched nanowire heterostructures. *Nano Letters*, 7:1817, 2007.
- [95] V. G. Dubrovskii M. Moewe, L. C. Chuang and C. Chang-Hasnain. Growth mechanisms and crystallographic structure of InP nanowires on lattice-mismatched substrates. *Journal of Applied Physics*, 104:044313, 2008.
- [96] E. Hilner A. Mikkelsen C. Thelander J. Stangl-B. Ohlsson A. Gustafsson E. Lundgren L. Samuelson T. Martensson, J. Wagner and W. Seifert. Epitaxial growth of indium arsenide nanowires on silicon using nucleation templates formed by self-assembled organic coatings. *Advanced Materials*, 19:1801, 2007.
- [97] A.Y. Cho and J.R. Arthur. Molecular beam epitaxy. *Prog. Solid State Chem.*, 10:157–191, 1975.
- [98] J.R. Arthur. Molecular beam epitaxy. *Surface Science*, 500:189, 2002.
- [99] S. Franchi, G. Trevisi, L. Seravalli, and P. Frigeri. Quantum dot nanostructures and molecular beam epitaxy. *Progress in Crystal Growth and*

- Characterization of Materials*, 47(23):166 – 195, 2003. *Vapour Growth of Bulk Crystals and Epitaxy: Part I*.
- [100] F. C. Frank and J. H. van der Merwe. One-Dimensional Dislocations. II. Misfitting Monolayers and Oriented Overgrowth. *Proceedings of the Royal Society of London. Series A. Mathematical and Physical Sciences*, 198(1053):216–225, 1949.
- [101] M. Volmer and A. Weber. Novel growth mechanism in heteroepitaxial semiconductor growth. *Z. phys. Chem*, 119:277, 1926.
- [102] IN Stranski, Krastanov. Theory of orientation separation of ionic crystals. *Acad. Wiss. Math.-Naturw. Klasse Iib*, 146:797, 1938.
- [103] P. H. Dawson, editor. *Quadrupole Mass Spectrometry*. Elsevier, 1976.
- [104] A V Blant, O H Hughes, T S Cheng, S V Novikov, and C T Foxon. Nitrogen species from radio frequency plasma sources used for molecular beam epitaxy growth of GaN. *Plasma Sources Science and Technology*, 9(1):12, 2000.
- [105] E Jones J S Chan X Liu-M D Rubin N W Cheung T C Fu, N Newman and E R Weber. The influence of nitrogen ion energy on the quality of GaN films grown with molecular beam epitaxy. *Journal of Electronic Materials*, 24:249–255, 1994.
- [106] M Kinniburgh A Ohtani, K S Stevens and R Beresford. Analysis and optimisation of the electron cyclotron resonance plasma for nitride epitaxy. *Journal of Crystal Growth*, 150:902, 1995.

- [107] Y W Kim N E Lee, R C Powell and J E Greene. Molecular beam epitaxy of GaN (0001) utilizing NH₃ and/or NH₄⁺ ions: Growth kinetics and defect structure. *Journal of Vacuum Science & Technology A*, 13(1):2293–2302, 1995.
- [108] R H Hammond and R Bormann. Correlation between the in situ growth conditions of YBCO thin films and the thermodynamic stability criteria. *Physica C*, 703:162–164, 1993.
- [109] G Ehrlich. *Chemistry and Physics of Solid Surfaces VII*, ed R Vanselow and R F Howe(1):1, 1988.
- [110] Z. Zhu, X.J. Zheng, and W. Li. Kinetic Monte Carlo simulation of RHEED from BaTiO₃ thin films. *Physica B: Condensed Matter*, 403(2122):4074 – 4078, 2008.
- [111] J. L. Hall. *Growth and Structural Characterisation of III-V Semiconductor Materials*. PhD thesis, University of Nottingham, 2010.
- [112] J.J. Harris, B.A. Joyce, and P.J. Dobson. Oscillations in the surface structure of Sn-doped GaAs during growth by MBE. *Surface Science Letters*, 103(1):L90 – L96, 1981.
- [113] L. Seravalli S. Franchi, G. Trevisi and P. Frigeri. Quantum dot nanostructures and molecular beam epitaxy. *Progress in Crystal Growth and Characterization of Materials*, 47(23):166, 2003. *Vapour Growth of Bulk Crystals and Epitaxy: Part I*.
- [114] Y.P. Varshni. Temperature dependence of the energy gap in semiconductors. *Physica*, 34(1):149 – 154, 1967.

- [115] W.A. Tiller. *The science of crystallization: macroscopic phenomena and defect generation*. Cambridge University Press, 1992.
- [116] G. Fasol S. Nakamura and S. J. Pearton. *The blue Laser diode*. Springer, 2000.
- [117] Antonio Luque and Antonio Martí. Increasing the Efficiency of Ideal Solar Cells by Photon Induced Transitions at Intermediate Levels. *Phys. Rev. Lett.*, 78:5014–5017, Jun 1997.
- [118] E. Calleja, J. Risti, S. Fernández-Garrido, L. Cerutti, M. A. Sánchez-García, J. Grandal, A. Trampert, U. Jahn, G. Sánchez, A. Griol, and B. Sánchez. Growth, morphology, and structural properties of group-iii-nitride nanocolumns and nanodisks. *physica status solidi (b)*, 244(8):2816–2837, 2007.
- [119] L. Geelhaar, C. Cheze, B. Jenichen, Oliver Brandt, C. Pfüller, S. Munch, R. Rothmund, S. Reitzenstein, A. Forchel, T. Kehagias, P. Komninou, G.P. Dimitrakopoulos, T. Karakostas, L. Lari, P.R. Chalker, M.H. Gass, and H. Riechert. Properties of GaN Nanowires Grown by Molecular Beam Epitaxy. *Selected Topics in Quantum Electronics, IEEE Journal of*, 17(4):878–888, 2011.
- [120] Shunfeng Li and A. Waag. Gan based nanorods for solid state lighting. *Journal of Applied Physics*, 111(7):071101–071101–23, 2012.
- [121] D. Cherns, L. Meshi, I. Griffiths, S. Khongphetsak, S.V. Novikov, N. Farley, R. P. Champion, and C.T. Foxon. Defect reduction in gan/(0001)sapphire films grown by molecular beam epitaxy using nanocolumn intermediate layers. *Applied Physics Letters*, 92(12):121902–121902–3, 2008.

- [122] W Walukiewicz. Intrinsic limitations to the doping of wide-gap semiconductors. *Physica B: Condensed Matter*, 302(0):123 – 134, 2001. Proceedings of Yanada Conference LIV. The 9th International Conference on Shallow-Level Centers in Semiconductors.
- [123] Hieu Pham Trung Nguyen, Yi-Lu Chang, Ishiang Shih, and Z. Mi. InN p-i-n Nanowire Solar Cells on Si. *Selected Topics in Quantum Electronics, IEEE Journal of*, 17(4):1062–1069, 2011.
- [124] B. L. Zhang, G. S. Sun, Y. Guo, P. F. Zhang, R. Q. Zhang, H. B. Fan, X. L. Liu, S. Y. Yang, Q. S. Zhu, and Z. G. Wang. Valence band offset of InN/4H-SiC heterojunction measured by x-ray photoelectron spectroscopy. *Applied Physics Letters*, 93(24):242107, 2008.
- [125] J. Neugebauer T. Zywietz and M. Scheffler. Adatom diffusion at GaN (0001) and (0001) surfaces. *Appl. Phys. Lett.*, 73:487, 1998.
- [126] R. S. Wagner and W. C. Ellis. Vaporliquid-solid mechanism of single crystal growth. *Applied Physics Letters*, 4:89, 1964.
- [127] J. L. Hall R. P. Champion-D. Cherns I. Griffiths C. T. Foxon, S. V. Novikov and S. Khongphetsak. A complementary geometric model for the growth of GaN nanocolumns prepared by plasma-assisted molecular beam epitaxy. *Journal of Crystal Growth*, 311:3423, 2009.
- [128] S. Y. Jingc D. P. Zhanga P. Fana E. Q. Xi X. M. Caia, F. Yeb. CVD growth of InGaN nanowires. *Journal of alloys and compounds*, 467:472, 2009.
- [129] S. Jeppesen M. T. Bjrk A. I. Persson, L. E. Froberg and L. Samuelson. Surface diffusion effects on growth of nanowires in cbe. *Journal of Applied Physics*, 101:034313, 2007.

- [130] Hannah Jane Joyce. *Growth and Characterisation of IIIIV Semiconductor Nanowires for Optoelectronic Device Applications*. PhD thesis, The Australian National University, 2009.
- [131] T. de Smet M. T. Borgstrom M. A. Verheijen, G. Immink and E. P. A. M. Bakkers. Growth kinetics of heterostructured GaPGaAs nanowires. *J. Am. Chem. Soc*, 128:1353, 2006.
- [132] K. Haraguchi K. Ogawa T. Katsuyama M. Koguchi K. Hiruma, M. Yazawa and H. Kakibayashi. GaAs freestanding quantum-size wires. *Journal of Applied Physics*, 74:3162, 1993.
- [133] S. Lenk M. I. Lepsa T. Rieger, S. Heiderich and D. Grutzmacher. Ga-assisted MBE growth of GaAs nanowires using thin HSQ layer. *Journal of Crystal Growth*, 353:39, 2012.
- [134] M. Yamaguchi J. H. Paek, T. Nishiwaki and N. Sawaki. Catalyst free MBE-VLS growth of GaAs nanowires on (111) Si substrate. *Physica Status Solidi C*, 6:1436, 2009.
- [135] Y. Horikoshi. Migration-enhanced epitaxy and its applications. *Japanese Journal of Applied Physics*, 35:497, 1992.
- [136] Y. Horikoshi. Migration-enhanced epitaxy of GaAs and AlGaAs. *Semiconductor Science and Technology* 8, 6:1032–1051, 1993.
- [137] D. Cherns, L. Meshi, I. Griffiths, S. Khongphetsak, S. V. Novikov, N. R. S. Farley, R. P. Champion, and C. T. Foxon. Defect-controlled growth of gan nanorods on (0001)sapphire by molecular beam epitaxy. *Applied Physics Letters*, 93(11):111911, 2008.

- [138] M. Skowronski, K. Doverspike, L. B. Rowland, W. Qian, G. S. Rohrer and D. K. Gaskill. Opemodel screw dislocations in GaN epilayers observed by scanning force microscopy and high-resolution transmission electron microscopy. *Applied Physics Letters*, 67:2284, 1995.
- [139] J. E. Northrup. Screw dislocations in GaN: The Ga-filled core model. *Applied Physics Letters*, 78, 2001.
- [140] V.V. Emstev, D.A. Kurdyukov, S.V. Ivanov, V.A. Vekshin, F. Bechstedt, J. Furthmuller, J. Aderhold, J. Graul, A.V. Mufroi, H. Harima, A. Hashimoto, A. Yamamoto, V.Yu. Davydov, A.A. Klochikhin and E.E. Haller. Band gap of hexagonal inn and ingan alloys. *Phys. Stat. Sol. b*, 234:787–795, 2002.
- [141] W. Shan, K. M. Yu, J. W. Ager III, E. E. Haller, H. Lu and W. J. Schaff, J. Wu, W. Walukiewicz. Effects of the narrow band gap on the properties of InN. *Physical Review B*, 66:201403, 2002.
- [142] M. O. Manasreh. *Optoelectronic properties of semiconductors and superlattices*. Gordon and Breach Science Publishers, 200.
- [143] B. Heying, R. Averbeck, L. F. Chen, E. Haus, H. Riechert, and J. S. Speck. Control of gan surface morphologies using plasma-assisted molecular beam epitaxy. *Journal of Applied Physics*, 88(4):1855–1860, 2000.
- [144] M.A. Sanchez-Garcia, E. Calleja, E. Monroy, F.J. Sanchez, F. Calle, E. Muoz, and R. Beresford. The effect of the III/V ratio and substrate temperature on the morphology and properties of GaN- and AlN-layers grown by molecular beam epitaxy on Si(1 1 1). *Journal of Crystal Growth*, 183(12):23 – 30, 1998.

- [145] Yoshiji Horikoshi and Minoru Kawashima. Growth mechanism of GaAs during migration-enhanced epitaxy at low growth temperatures. *Japanese Journal of Applied Physics*, 28(Part 1, No. 2):200–209, 1989.
- [146] Michael Moseley, Jonathan Lowder, Daniel Billingsley, and W. Alan Doolittle. Control of surface adatom kinetics for the growth of high-indium content InGaAs throughout the miscibility gap. *Applied Physics Letters*, 97(19):191902, 2010.
- [147] F. Briones, D. Golmayo, L. Gonzalez, and A. Ruiz. Phase-locked RHEED oscillations during MBE growth of GaAs and Al_xGa_{1-x}As. *Journal of Crystal Growth*, 81(14):19 – 25, 1987.
- [148] K. Ohta, T. Nakagawa, N. J. Kawai, T. Sakamoto, H. Funabashi and T. Kojima. Phase-Locked Epitaxy Using RHEED Intensity Oscillation. *Japanese Journal of Applied Physics*, 23:L657, 1984.
- [149] C. T. C. T. Foxon. Orton. *Molecular Beam Epitaxy: A short History*. Oxford University Press, 2015.
- [150] C.T. Foxon, R.P. Champion, V.A. Grant, S.V. Novikov, J.J. Harris, R. Thomson, C. Taylor, and D. Barlett. Use of band-gap thermometry to investigate the growth of GaAs on sapphire and GaAs. *Journal of Crystal Growth*, 301(0):482 – 485, 2007. *14th International Conference on Molecular Beam Epitaxy*; *MBE XIV*.
- [151] D. C. Lock, B. Clavin, S. D. Burnham, G. Namkoong and W. A. Doolittle. Reproducible increased Mg incorporation and large hole concentration in GaAs using metal modulated epitaxy. *J Appl Phys*, 104:024902, 2008.

- [152] M. Senoh S. Nakamura and T. Mukai. Highly p-typed mg-doped gan films grown with gan buffer layers. *Japanese Journal of Applied Physics*, 30:L1708–L1711, 1991.
- [153] C.T. Foxon J.L. Hall, A.J. Kent and R.P. Campion. Temperature effects during the growth of ingan films through the whole compositional range by plasma-assisted molecular beam epitaxy. *Journal of Crystal Growth*, 312:2083–2088, 2010.
- [154] William Shockley and Hans J. Queisser. Detailed balance limit of efficiency of p-n junction solar cells. *Journal of Applied Physics*, 32(3):510–519, 1961.
- [155] Gavin Conibeer. Third-generation photovoltaics. *Materials Today*, 10(11):42 – 50, 2007.
- [156] M. A. Green. Third generation photovoltaics: Ultra-high conversion efficiency at low cost. *Progress in photovoltaics:research and applications*, 9:123, 2001.
- [157] T. Aschenbrenner S. Bley A. Rosenauer M. Seyfried J. Kalden K. Seibald J. Gutowski C. Tessarek, S. Figge and D. Hommel. Strong phase separation in strained InGaN layers due to spinodal and bimodal decomposition: formation of stable quantum dots. *Phys. Rev. B*, 83:115316, 2011.
- [158] Ch. Meissner M. Pristovsek M. Kneissl M. Leyer, J. Stellmach. The critical thickness of InGaN on (0 0 0 1) GaN. *Journal of Crystal Growth*, 23:4913–4615, 310.
- [159] J. W. Cahn. Phase separation by spinodal decomposition in isotropic systems. *The Journal of Chemical Physics*, 42 (1):93–99, 1965.

- [160] G. B. Stringfellow. Immiscibility and spinodal decomposition in III/V alloys. *Journal of Crystal Growth*, 65:454–462, 1983.